12-23-2016

Lipid-Based Self-Assembled NPs: The Effects of Morphology and Targeting Molecules on the Cellular Uptake Using In Vitro Tumor Model

Wafa Aresh
wafa.aresh@uconn.edu

Lipid-Based Self-Assembled NPs: The Effects of Morphology and Targeting Molecules on the Cellular Uptake Using *In Vitro* Tumor Mode

Wafa Aresh, Ph.D
University of Connecticut, 2017

While the usage of nanoscale materials for therapeutics and diagnostics is growing rapidly, there remain many challenges to understanding the expected controlling parameters (e.g., size, shape and chemical properties) that significantly affect the performance of the nanomaterials due to complicated *in vivo* environments. Therefore, a strong interest in the knowledge of the nano–bio-interactions and how they contribute to tissue accumulation has been developed. To date, researchers have relied on monolayer cell cultures and animal models to study such nano–bio-interactions. However, currently, there is a big gap between the result of the over-simplified *in vitro* cell response and the complex animal models, where many biological reactions and organs may interact with the nanomaterials. Novel non-expensive microfluidic systems have recently been designed to mimic the tumor environment (including extracellular (ECM) tissue and cancer cells). Moreover, well-defined and low-polydispersity lipid-based nanoparticles (NPs) have been synthesized into various morphologies such as nanodiscs, vesicles, ribbons, *etc*. in Prof. Mu-Ping Nieh's research group, and we will test their potential application in cancer drug delivery.

Lipid-Based Self-Assembled NPs: The Effects of Morphology and Targeting Molecules on the Cellular Uptake Using *In Vitro* Tumor Model

Wafa Aresh

B.S., King Abdulaziz University, Saudi Arabia, 2007

M.S., University of Bridgeport, USA, 2012

A Dissertation

Submitted in Partial Fulfillment of the

Requirements for the Degree of

Doctor of Philosophy

at the

University of Connecticut

2017

APPROVAL PAGE

Doctor of Philosophy Dissertation

"Lipid-Based Self-Assembled NPs: The Effects of Morphology and Targeting Molecules on the Cellular Uptake Using *In Vitro* Tumor Model"

Presented by

Wafa Aresh, B.Sc., M.Sc.

Major Advisor _____

Mu-Ping Nieh

Associate Advisor_____

Quing Zhu

Associate Advisor _____

Yu Lei

Associate Advisor _____

Yongku Cho

University of Connecticut

2017

Acknowledgements

I would like to express my sincere appreciation to my advisor Prof. Mu-Ping Nieh for his tremendous support and encouragement to pursue my research interests. Because of your excellent mentorship, I learned the importance of critical thinking and hard work and developed professional, leadership, and teambuilding skills. Thank you for your patience and the hard work that you dedicated to me, and I sincerely hope that our professional and personal relationship will last and grow.

A special thanks to Prof. Yu Lei and Prof. Quing Zhu, my associate advisors, for their support and advice. I am also very thankful to Prof. Pinar Zorlutuna, for her collaboration and the time she dedicated to my work. I am deeply thankful to Prof. Yongku Cho, Prof. Tai-His Fan, and Prof. Savas Tasoglu for allowing me to use instruments in their laboratories. I would like to thank all past and present project collaborators and lab members, especially Prof. Yong Wang, Dr. Anu Puri, Ms. Ying Liu, Ms. Yike Huang, Ms. Jessica Sine, Mr. Derek Thayer, Ms. Andreana Panzo, Ms. Yan Xia, Mr. Armin Tahmasbi Rad, Prof. Ping-Shan Lai, Chen ching-wen and everyone else who offered me their help and friendship. This work would not have been possible without the help and support from UConn Biotechnology-Bioservice Center. Special thanks to Dr. Carol Norris for the training and her assistance in the use of Flow Cytometry/Confocal Microscope. Also, I would like to acknowledge the financial support I received from the Saudi Arabian Ministry of High Education for my tuition. Lastly, I would never have reached this point without the love and support from my husband, Abdulrahman Alsaddah, my parents, my children, and my extended family and friends.

Table of Contents

List of Figures

List of Tables

List of Schemes

Chapter 1. Background and Literature Review

1.1 Background and Literature Review

Nanotechnology is an emerging research area in biomedical science and engineering, promising to overcome issues such as targeting delivery and efficacy of cellular uptake.[1] The term “nanotechnology” was invented by Professor Norio Taniguchi of Tokyo Science University in the year 1974 to describe precision manufacturing of small-scale materials (1 to 100 nm) that can be used in different applications.[2, 3] In recent years, various nanotechnology platforms have gained exceptional attention in the area of medical research, including diagnosis and therapy.[4, 5] During the past 40 years, research on the nanoparticles for pharmaceutical and medical applications have been conducted to investigate the potential of different nanoparticles (NPs) in related applications.[6] Because of the complexity of the human body, these systems of nanoparticles should be studied carefully before they can be available commercially. Abraxane™, human serum albumin nanoparticles containing paclitaxel, is the first commercial nanoparticle product containing a drug appeared on the market at the beginning of 2005.[7]

The consideration of nanoscale materials in the field of medicine is proven to have efficient and safe applications over the last decades.[5, 8-12] However, nanoparticles cannot be considered for a clinical application until some of their critical parameters have been carefully examined such as physical properties, drug loading efficiencies, drug release potential, and, most importantly, minimum toxicity. [13] Therefore, the requirement of more investigation to understand the role of nanoparticles’ characteristics in the interaction with the human tissue at the micro level is essential.

Nanoparticles are attractive for medical purposes because of their unique properties, such as high surface area which is larger than that of other particles, fast absorption of other compounds

and excellent encapsulation.[14] NPs have a relatively large surface which can bind and carry other compounds such as drugs, probes, and proteins.[15, 16] In many cases, surface modifications promote the functionality of these nanocarriers to achieve the maximum functionality of the carrying systems. Researchers have also found that the size, shape and surface chemistry of nanocarriers for biological and medical agents can dictate their efficacy.[17, 18]

Currently different materials are under investigation for drug delivery and more specifically for cancer therapy. Polymer-Based nanoparticles have been demonstrated high efficacy in cancer targeting.[19] These systems include polymeric drugs, polymer-protein conjugates, polymer-drug conjugates, and polymeric micelles.[20] These biocompatible polymers can be either synthesized or nature-derived indicating antiviral or antitumor properties.[21, 22] One of the most commonly used polymers to enhance the biocompatibility is polyethylene glycol (PEG) which allows nanoparticles to have a longer *in vivo* circulating time.[23, 24] PEG-drug conjugation is also applied to improve drug solubility and specificity of low molecular weight drugs. Lastly, polymeric micelles (PMs) composed of amphiphilic polymers are commonly used to entrap poorly water-soluble drug in the hydrophobic core of the micelles which protect the drug from the aqueous environment and stabilize the PMs against recognition *in vivo* by the reticuloendothelial system (RES).[25, 26]

Anticancer nanoparticles have made a tremendous impact in the treatment of various types of cancer, as proved by clinical use.[27] Recently, many review papers have presented different examples of numerous liposomal and polymer based drugs systems.[28, 29] PEGylated liposomal doxorubicin is one of drug formulations that is used for cancer treatment.[30, 31] The hydrophilic doxorubicin can be encapsulated in the water core of liposomes (vesicles). The general size of the vesicle is approximately 100 nm in diameter and shielded by a dense layer of polyethylene glycol

(PEG).[32] PEG attachment improves the reduction of the renal clearance of drugs and thus enhances uptake by cells. As a result, the lipid/drug complex has extended half-life and hence the frequency of drug administration is reduced.[31] Although nanoparticles have demonstrated enhanced efficacy to detect and treat cancer cells, the number of nanoparticle-based medicines approved for clinical use remains low[33] mainly because of the complexity of nanoparticles interacting with the human tissue. Hence, careful design of the nanoparticles and detailed analysis of the structure-function relationship are urgently needed. For that, researchers have been working to overcome any challenges developing smart therapeutics that are more effective and less toxic.

Lipid- based nanoparticles have the advantage of high biocompatibility and most of the lipids have been FDA approved and commercially used for *in vivo* anticancer drug carriers. Liposomes have been extensively reported as an example of lipid-based nanocarriers, which mainly consist of phospholipids (major components of biological membranes) and cholesterol.[34] They showed enhancement in biomedical applications in the aspects of stabilizing therapeutic compounds, enhancing cellular and tissue uptake, and improving *in vivo* biodistribution of drug compounds.[35-37]. The formation of liposomes is based on the physiochemical properties of the phospholipid molecules, which have hydrophobic and hydrophilic components, forming bilayers.[35-38] The size of liposomes can range from tens to thousands of nanometer.[20] Hydrophilic drug molecules can be encapsulated within the fluid enclosed by the vesicular lipid bilayers. Such encapsulation protects drugs from early inactivation, degradation, dilution in the circulation, while maintains minimal toxicity.[39] Since the 1980s, liposomes have been used in clinical applications, providing the efficacy of therapeutics, such as doxorubicin and amphotericin. [35, 36, 40]

Recently low-polydispersity lipid-based nanodiscs were found spontaneously forming in a mixture composed of long- and short- chain phospholipids.[41] These nanodiscs are capable of entrapping hydrophobic molecules in the bilayer core and have a robust formation mechanism,[42, 43] allowing large-quantity nano-manufacturing of the NPs. Most importantly, a transition of nanodisc-to-nanovesicle also takes place as the structure of long-chain lipid varies from the low-*T* gel (order) to high-*T* L_α (liquid disorder) phase. These nanovesicles are also uniform in size (low-polydispersity) and go through the irreversible formation at low lipid concentration even when the temperature reverts to the initial low *T*, where the long-chain lipid is in the gel phase.[43-45] Such properties allow us to produce different *low-polydispersity* morphologies from materials of *the same chemical composition* and enable our investigation on the morphological dependence of NPs as they interact with the cells while the other physicochemical characteristics remain constant. Note that these phospholipids are also biocompatible; thus, suitable for therapeutics or diagnostics applications of nanocarriers. However, the efficiency of these nanoparticles served as delivery vehicles remain unpredictable because of poor control over the way of interaction between carrier systems and the tumor tissue *in vivo*.[4] To overcome this problem, a better understanding of how nanoparticles (based on their size, morphology, and surface modification) interact and distribute at the cellular level in the tumor site is required.

Another important characteristic for effective drug delivery carriers is the local accumulation of NPs at the desired locations to enhance the cellular uptake.[5, 46-49] Based on several *in vitro* and *in vivo* studies, it has been reported that tumor accumulation of particle is affected by their size, shape, and surface chemistry.[18, 46] Recent studies indicated that the cellular uptake of nanoparticles depends not only on their chemical compositions but also the physical parameters such as shape and size [46, 49-53] as well as the cell lines used in the

study.[54] For example, under typical physiologically relevant conditions for several cell types, polymeric disc-shaped hydrophilic particles with diameters of 325 nm and 220 nm can be internalized more efficiently compared to nanorods or smaller-sized nanodiscs (80 nm in diameter).[54] However, the effect of the morphology of NPs on cellular uptake can only be unambiguously deduced based on the NPs made of the same chemical compounds and compositions.

Furthermore, targeting to molecular markers overexpressed on the surface of diseased cells can enhance the specificity and efficacy of delivery and decrease the potential damage to healthy tissues.[55] The vasculature in tumor tissues is usually leaky to macromolecules, and the tumor lymphatic system is deficient,[38] allowing nanoparticles with diameters < 100 nm to be preferentially delivered to the tumor through the enhanced permeation and retention (EPR) effect via blood vessels.[56] That is also known as "passive targeting," where the specificity is only based on size. Therefore, it is important to develop a more accurate and active system that could target the tumor and enhance intracellular uptake of NPs in the tumor sites. [57] This is called "active targeting." Another approach is to decorate the surface of NPs with molecules or ligands which target the overexpressed proteins on the surface of cancer cells. The targeting ligands can be small molecules or antibodies. This would presumably further improve the delivery of drugs to the targeted site in the human body.[33] The addition of targeting ligands allows the delivery of nanoparticles to target specific cells, thereby hoping to reduce the unwanted systemic exposure of cytotoxic drug.[57] The potential use of receptor-based actively targeting nanoparticles has drawn tremendous interest in their applications for diagnostic and therapeutic delivery.[58-60] Numerous targeting ligands have been investigated as biomarkers for targeted drug delivery including antibodies, antibody fragments, aptamers, peptides and different receptor ligands (e.g., folic

acid).[58-60]

The fact that folate receptor (FR) expression is high in many human cancers including kidney, brain, ovarian, lung, breast and colon cancers prompts the application of folic acid for a targeting ligand.[61, 62] FR has two glycosyl phosphatidylinositol-anchored isoforms: alpha and beta.[63] The expression of FR-alpha is frequently observed in epithelial cancer cells, whereas FR-beta expression is found in leukemia and inflammatory disease.[64] Therefore, FA is considered to be an attractive agent for tumor-specific drug delivery. Another important feature of FR is its location on the membrane of epithelial cancer cells, which is different from the membrane of normal cells.[65] It should be noted that folic acid has a very high binding affinity ($K_d \sim 10^{-9}$ M) with FR and can be conjugated to the surface of NPs, enhancing the delivery and cellular uptake.[66] Several studies verified that folic-acid-drug conjugates are efficient for folate targeting.[62, 67-69]

The efficacy of nanoscale-sized folate receptor-targeted conjugates called doxorubicin-polyethylene glycol-folate (DOX-PEG-FOL) aggregates was tested for the treatment of cancer in 2004 at the Korean Advanced Institute of Science and Technology.[70] The results of this study demonstrated a significant reduction in the size of the tumor using folate-targeted doxorubicin nano-aggregates compared to non-targeted doxorubicin aggregates or free doxorubicin.[70] In another study folate-PEG-chitosan-graft-low polyethyleneimine (FPCP) has been reported as a cancer cell-targeting gene carrier because of specific ligand-receptor interactions between folate molecules and the folate receptor.[71] More recently, folate receptor directed mercaptosuccinic acid-coated gold nanoparticles (GM) for detecting and imaging oral cancer were tested *in vitro* using KB cells and animal skin cells (NIH3T3).[72] The results showed that the folic acid linked GM could specifically target oral cancer cells and emit intense fluorescence for imaging, revealing more efficient intracellular uptake into KB cells compared to the other cell line used in

the study.[72] A novel lipid-polymer hybrid drug carrier comprised of folate (FA) modified lipid shell and polymer-core nanoparticles (FLPNPs) loaded with paclitaxel were developed for breast cancer treatment.[73] The outcomes of this study showed improvement of the cellular specific uptake and tumor size reduction with a minimum cytotoxicity.[73] These results suggested that folate-targeted paclitaxel nano-aggregates could be a useful delivery system for folate-receptor-positive cancer cells. Therefore, designing an applicable NPs, whose surface is coated with folate, as a delivery system is important to guide carriers to cancer cells. Afterward, the drug carriers are then internalized via receptor-mediated endocytosis.

The study of nanoparticles' efficiency is usually achieved through *in vitro* experiments of animal or human cell cultures or *in vivo* animal models. However, the data of the interaction between the nano-carriers and the cell gained from *in vitro* cell monolayer experiments is mostly limited to characterization of the binding affinity, uptake, cellular responses and toxicity of the nanoparticles.[46, 54, 74, 75] The absence of a three-diminution (3D) tissue structure makes these findings inaccurate to predict the *in vivo* results. Many pieces of evidence suggest that the 3D tumor models replicate more accurately the actual microenvironment of the tumor than the 2D cell model since they lose their phenotypes as are cultured in 2D environments; therefore, the behavior of 3D tumor model would reflect more closely the *in vivo* responses.[76-79] *In vivo* animal models have been applied to assessing general pharmacokinetics[80-82], and the effects of size, shape, surface modification and the composition of delivery carriers on their efficacy. However, it has been hard to visualize target tissues at the cellular level in animal models because of the low resolution of whole-animal imaging techniques.[83] Thus, it will be more efficient if a replication of the *in vitro* 3D animal model with accessible and well-controlled microenvironment is established to study the behavior of nanoparticles.

Hence, an easily prepared 3D cell culture model would be an alternative to mimic animal models. Multicellular spheroid (MCS) is one of the most well-known models used in this matter; it was first demonstrated by Holtfreter [84] and Moscona [85] using suspended cells to form the spheroid through a self-assembly process. Most MCS are similar to real human tissues in many aspects compared to monolayer cell cultures.[86] Many challenges prevented using spheroid tissue models for studying drug delivery in the past.[87] The formation of spheroids in uniform size and shape is one of the most common obstacles that prevented the use of spheroids in biomedical studies.[88] Another challenge is the difficulty of forming spheroids with an insufficient number of cells or using different types of cells to form tissue-like spheroids.[89] Nevertheless, the techniques allows the production of uniform, multi-cell-type spheroids to investigate drugs and drug delivery systems *in vitro.[86]* The comparable outcome of spheroids to that of the *in vivo* tissues validates the feasibility of using them to study the drug diffusion to organs.[86] Cancerous cells can also grow into multicellular spheroids, providing a model for testing drugs and their carriers.[90]

In the early 80s, the microfluidic technology started to emerge into biomedical studies, and more effort was required to improve the usage of this technique. Nowadays, microfluidic approaches are used in various research fields such as molecular and cell biology.[91] The advantages of the microfluidic device to grow in vitro tumor include better control of the cellular microenvironment and analyzing cellular interaction at the micro level.[92] Using microstructures to guide multicellular self-assembly is an emerging and powerful technique for generating MCS with well-controlled size and morphology.[93-97] Several chip-based MCS culture systems have been recently developed for comprehensive drug screening.[98] Microwells and microchannels were designed in these chips which trap thousands of MCS into arrays and then testing chemicals were delivered through the channels.[99] Cellular behavior

such as viability, chemical signaling, and responses can be extensively studied in real time on the microchip by a variety of methods.[100, 101] In 2005, a drug screening microchip was fabricated to examine the effect of antiallergic agents by detecting the released histamine from suspended cells.[102] The microchips have been proved to be capable of antiallergic drug screening by measuring the inhibition of histamine released from cells.[102] Recently, concave microwells with different diameters were used to form 3D tumor models and to test the effect of drug loaded nanoparticles. After 96 hours, scanning electron microscopy was used to monitor the tumor, and the results revealed a reduction in the size of the smallest tumor whereas the larger tumor did not show any changes.[103]

Another application of MCS-on chip is detecting the optimal conditions for stem cell differentiation to improve tissue engineering.[101] In 2006, a study by a group from WiCell Research Institute of a 3D microwell-based cell culture was used to keep human embryonic stem cells (hESC) from differentiating for weeks.[104] The growth of cells aggregates was controlled by different patterns of extracellular matrix (ECM) which revealed in maintaining the viability of hESCs for 2–3 weeks.[104] Moreover, microfluidic devices or microchips have been used extensively in the past few years to replicate human organs. Organ-on-a-chip is a merge tool to provide more valuable features than the animal models, which are expensive and require longer preparation time while sometimes fail to predict human responses.[105] A 3D microchip was fabricated to create a specific disease model of breast cancer that replicate the relations between metastatic breast cancer cells and their migration via vascular endothelium and bone tissue.[106] The model employed human umbilical vein endothelial cells in a 3D collagen gel microfluidic channel that contained bone cells. Cancer metastasis was then examined using high-resolution real-time microscopy to measure the migration of metastatic breast cancer cells in the vascular channel and their fate into the bone matrix.[106] The concept of the organ-on-a-chip can be used

as a critical measurement of therapeutic drugs to speed up the process of clinical trials. The potential of this approach was investigated in a recent study in which a 3D assay of epithelial-mesenchymal transition during cancer progression was developed. Lung cancer spheroids were cultured in a 3D matrix gel with endothelial coating microchannel to study the effect of 12 drugs on the behavior of cancer cells. The results were analyzed by direct visualization of the cancer spheroids. Interestingly, the results were not consistent with results from 2D culture.[107]

Another phenomenon observed among certain cancer patients is multidrug resistance where cancer cells develop resistance to chemotherapy drugs. This presents a major barrier to the treatment of different types of cancer.[108] For that, a better understanding of the interaction between the drugs or their carriers with the tumor is essential to develop high impact carriers that penetrate through the entire tumor cells. Several 3D *in vitro* studies have been performed to evaluate the diffusion of the chemotherapeutic drug in the human tissue;[109-112] however, the role of pharmaceutical carriers design in tumor accumulation is not well addressed. There have been only a few studies applying microfluidic devices to evaluate the relationship between nanoparticles physiochemical properties and their penetration into the tumor.[111, 113-115] A group from University of Washington developed a 3D microchamber to study the penetration of fluorescently labeled nanoparticles prepared in three different sizes (40, 100, 500 nm) and monitor their transportation in cell–gel soft tissue cultures. The results of this study demonstrated the impact of the size of the nanoparticles on their penetration inside tumor tissue.[116] More recently another study was conducted to evaluate the effect particle shape, size and density on their transportation within blood vessels in microchannel model. In this study, different types of nanoparticles were prepared in various sizes and densities were tested in a fibronectin-coated microfluidic channel. The results showed completely different migration rates based on the physiochemical properties of the nanostructures.[117] These researchers were mainly focus on the

effect of the size, instead of the morphology or surface modification (with targeting molecules), of the NPs on their distribution in the tumor.[115, 116] These studies suggested the microfluidics can serve as an approach for the rapid and profitable pre-screening of nano-carriers, providing sufficient data to model the transport process before full animal studies.[118] Therefore, our knowledge of the effect of both shape and surface targeting molecules of the NPs on penetration and tumor accumulation can be further advanced.

1.1 Dissertation Objectives:

This dissertation focuses on the fundamental knowledge of the effect of the NP shape on the cancer cellular uptake (adherent and suspension cells) and the endocytic pathways. Furthermore, this work investigates the efficacy of the NPs in the presence and absence of the folate group, which targets the receptor on the surface of cancer cells. Finally, a three-dimensional (3D) tumor model using a microfluidic device is constructed to allow real-time imaging and analysis of the penetration of the NPs under a physiological condition.

The outcome of the abovementioned research serves the functions to reveal the morphological dependence of cellular uptake (including the internalization mechanism). Moreover, the targeting effect of folate modification on the cellular uptake will be investigated using the 3-D tumor model to fill the gap between the over-simplified 2D cell model and complicated 3D *in vivo* tumor model to investigate the trafficking of the NPs in the tumor tissue.

Chapter 2. The Morphology of Self-Assembled Lipid-Based Nanoparticles Affects Their Uptake by Cancer Cells

Abstract

The morphology of nanoparticles (NPs) has been presumed to play a major role in cellular uptake and *in vivo* stability. This report experimentally demonstrates such dependence by using two types of uniform-sized self-assembled lipid-based NPs, namely nanodiscs and nanovesicles, composed of identical lipid composition. The morphology is characterized by small angle neutron scattering, dynamic light scattering, and transmission electron microscopy. Both NPs have similar bio-stability in serum and cellular cytotoxicity. However, cellular uptake of the nanodiscs at 37°C is consistently and significantly higher than that of the vesicles according to the uptake results of several human cancer cell lines, i.e., CCRF-CEM, KB, and OVCAR-8, indicating a strong morphological dependence of cellular internalization. Further studies on such morphological dependence using CCRF-CEM reveals that vesicles only use Clathrin- and caveolae-mediated endocytic pathways, while nanodiscs also take the additional routes of macropinocytosis and microtubule-mediated endocytosis.

2.1 Introduction

Nanoparticles (NPs) have been extensively investigated for biomedical applications as carriers for theranostics delivery[5, 75, 119] and molecular imaging.[9, 120] In addition to passive targeting delivery of nanoparticles to the desired locations via enhanced permeability and retention (EPR) effect, enhancing the cellular uptake is also an important parameter to achieve the high efficacy of the drug delivery.[5, 46-49] Studies suggest that the size and shape of a pharmaceutical carrier can affect its circulation in the blood, distribution in organs, intracellular transport, and the *in vivo* fate.[121] For example, trastuzumab-coated polystyrene microrods showed 15-fold enhancement of the uptake by SK-BR-3 cells compared to that of the spherical particles which were only five-fold higher than that of the uncoated particles.[122] In another study, the cellular uptake of cylindrical and spherical NPs produced by self-assembly of poly (acrylic acid) and polystyrene diblock copolymers was compared. The results revealed that the uptake of spherical NPs by Chinese Hamster Ovary cells was higher than that of the cylinder.[123] These studies suggest that the influence of the NPs shape on the enhancement of cellular uptake cannot be universal to a specific morphology; however, other parameters such as cell types, and materials used for NPs are also important.

Despite these studies, only a few materials have been examined to correlate the morphology of particles with the cellular interactions, and moreover, the length scale of interest was mostly in the size range of microns, instead of nanometers.[124-127] However, it is known that EPR effect works best for NPs with a size less than 100 nm. It has been reported that the diffusion of Au NPs across the tumor extracellular matrix is strongly sized dependent; particles in size range of ~ 20 nm or smaller showed superior penetration compared to larger Au NPs.[128] Also, an *in vivo* study on gold NPs of a size < 10 nm indicated better penetration in the breast cancer tumor spheroids

than the larger NPs did.[129] It has also been reported that, while larger polymeric micelles (~ 100 nm) were able to diffuse through highly permeable tumors, only NPs in 30 nm size were able to penetrate poorly permeable tumors.[130]

It should be noted that the cellular uptake of NPs depends on their chemical compositions in addition to their physical parameters (e.g., shape and size).[46, 48-53] Most of the studies on morphological dependence focused on metals or polymers. The correlation between cellular internalization and the nano-scaled morphology of biologically relevant materials (e.g., lipids, biosurfactants and proteins), though necessary, remains largely unexplored. The main challenge is the production of NPs with *uniform*, *distinct* nanoscopic structures but composed of *the same chemical composition*. Recently, low-polydispersity lipid-based nanodiscs, also known as bicelles, were found spontaneously forming in a mixture consisting of long- and short- chain lipids.[131] These bicellar nanodiscs can self-assemble robustly and are capable of entrapping hydrophobic molecules.[42, 43] A nanodisc-to-nanovesicle structural transition can also take place as the long-chain lipid melts from the low-temperature gel (order) to the high-temperature L_α (liquid disorder) phase. Both nanodiscs and nanovesicles are uniform in dimensions. At low lipid concentrations, the nanovesicles *irreversibly* form and would not revert to nanodiscs even when the long-chain lipid becomes gel phase as the temperature drops below its melting point.[43-45] These properties allow us to produce NPs of different morphologies, and low-polydispersity from the *identical chemical compositions*[43], thus enabling a non-bias investigation on the interaction between the NPs and the cells upon the variation of NP morphology while other physicochemical characteristics were kept invariant.

The global (average) structure and polydispersity of the NPs in this study were characterized using small angle neutron scattering (SANS) and dynamic light scattering (DLS), further confirmed by

the transmission electron microscopy (TEM) data. The SANS patterns of the bicellar nanodiscs and nanovesicles are distinct from each other and can be best fitted by the discoidal and core-shell oblate models, respectively. DLS can provide the polydispersity and the hydrodynamic radii, R_H of the NPs based on the assumption of Stokes-Einstein relationship for spheres.

In this report, we will present the dependence of cellular uptake and internalization mechanisms on NP morphology using fluorescence activated cell sorting (FACS) and fluorescence confocal optical microscopy (FCOM). Several significant findings are described as follow: First, two definite and uniform lipid-based NPs entrapping hydrophobic dyes of the identical chemical composition can be produced in the forms of nanodiscs and nanovesicles, and are found stable in serum. Second, the cellular uptake of nanodiscs is significantly higher than that of the similar-sized vesicles under the identical physiological conditions. Third, the nanodiscs utilize two additional cellular internalization mechanisms, i.e., macropinocytosis and microtubule-mediated transport in addition to the common clathrin- and caveolae- mediated pathways, which appeared to be the only routes taken by the nanovesicles. Finally, the enhanced endocytosis in the case of bicellar nanodiscs is observed consistently in three different cell lines (i.e., CCRF-CEM, KB, and OVCAR-8) of our study.

2.2 Materials

Dipalmitoyl phosphatidylcholine (di-16:0, DPPC), dipalmitoyl phosphatidylglycerol (DPPG), dihexanoyl phosphatidylcholine (di-6:0, DHPC), polyethylene glycol (PEG2000)-conjugated distearoyl phosphoethanolamine (DSPE-PEG2000), and 1-palmitoyl-2-{12-[(7-nitro-2-1,3-benzoxadiazol-4-yl) amino] dodecanoyl (NBD-PC) were purchased from Avanti Polar Lipids (Alabaster, AL, USA) and used without further purification. Nile Red (NR), phosphate buffered saline (PBS) powder and all pharmacological inhibitors were purchased from Sigma-Aldrich (St.

Louis, MO). Sepharose CL-6B was purchased from GE Healthcare (Pittsburgh, PA, USA). Cell Titer Blue kit was purchased from Promega (Madison, WI, USA). Dulbecco's Modified Eagle Medium (DMEM), phenol-free RPMI-1640 medium, Dulbecco's Phosphate-Buffered Saline (DPBS), fetal bovine serum (FBS), HEPES-buffered saline (HBS), and Hoechst 33342 were purchased from Life Technologies (Grand Island, NY, USA).

2.2.1 Cells

Human lymphoma CCRF-CEM cell line was cultured in phenol-free RPMI-1640 media supplemented with 10% FBS and 1% penicillin at 37˚C in 5%CO_2 and 95% humidified air.

Human cervix carcinoma KB cells were grown continuously as monolayers using DMEM media containing 10% FBS at 37 °C in a 5% CO2 and 95% air humidified atmosphere.

Human ovarian carcinoma OVCAR-8 were cultured as a monolayer in phenol-free RPMI-1640 media supplemented with 10% FBS and 1% penicillin at 37˚C in 5%CO_2 and 95% humidified air.

2.3 Methods

2.3.1 Preparation and Characterization of Nanoparticles

Dipalmitoyl phosphatidylcholine (di-16:0, DPPC), dipalmitoyl phosphatidylglycerol (DPPG), dihexanoyl phosphatidylcholine (di-6:0, DHPC), polyethylene glycol (PEG2000)-conjugated distearoyl phosphoethanolamine (DSPE-PEG2000), and 1-palmitoyl-2-{12-[(7-nitro-2-1, 3-benzoxadiazol-4-yl) amino] dodecanoyl (NBD-PC) or Nile Red (NR) were used for NPs preparation. Details on the characterization of lipid NPs are given in (Supplementary Materials). The molar composition of the mixture follows DPPC/DHPC/DPPG/DSPE-PEG2000/NR = 66.25/25/3.75/5/0.002. If NBD-PC is included, it has the same composition as NR. All components of the required weights were first homogenized in chloroform. After the removal of solvent in a vacuum oven, the dried samples were then re-dispersed in filtered D.I. water (or D_2O if the samples

were for SANS measurements) to make stock suspensions with a total lipid weight concentration, C_{lp} of 10 wt%. After successive vortex and temperature cycling between 25 and 70°C, the samples were completely homogenized. The 10 wt% stock dispersions were then progressively diluted at room temperature to C_{lp} = 1.0, 0.5 and 0.25 mg/ml with either water (or D_2O for SANS), 140 mM NaCl aqueous solution or phosphate buffered saline (PBS) solution, depending on the usages (i.e., DLS, SANS, stability or cellular uptake studies).

2.3.2 Nanoparticles Size Analysis and Characterization (Thanks to Ying Lue)

2.3.2.1 Dynamic Light Scattering

Size and population distribution of nanodiscs and vesicles were determined by DLS measurements using a Malvern instrument (NANO ZS, Malvern Instruments, CA, USA). For a typical sizing experiment 10 µl of NPs was diluted in 390 ml, HBS were placed into a Zeta-sizer cuvette. Each run consisted of 3 measurements of 12 to 20 acquisitions.

2.3.2.2 Small Angle Neutron Scattering

SANS data were collected using the EQ-SANS instrument at the Spallation Neutron Source at Oak Ridge National Laboratory. The sample-to-detector distance was set to 4.0 m. A 25 mm source aperture and a 10 mm sample aperture were used to collimate the incident beam. The instrument was operated in the 30 Hz "frame-skipping" mode with a minimum wavelength setting of 2.5 Å, providing a second wavelength band starting at 9.4 Å resulting in a combined q-range ($q = \frac{4\pi}{\lambda} sin\frac{\theta}{2}$, where θ is the scattering angle and λ is the neutron wavelength) covering 0.007 ~ 0.40 Å−1. The data fitting was performed in the q-range from 0.007 to 0.25 Å−1, since incoherent scattering dominates the higher q range. Data correction followed standard procedures implemented in MantidPlot (http://www.mantidproject.org/) to correct for sample transmission, detector sensitivity, and dark background before circularly averaging the 2D data around the beam center

to produce I(q) versus q. The data from the two wavelength bands were also merged into a single profile using MantidPlot.

2.3.2.3 Transmission Electron Microscopy

The negatively staining TEM micrograph was obtained by an FEI Tecnai T12 transmission electron microscope. The samples were prepared in the following steps. A drop of 5 µl solutions in a concentration of 0.01 mg/ml was first placed on a 400 mesh copper grid coated with Formvar/carbon film (Electron Microscopy Sciences, PA, USA). The excessive solution was then blotted with Whatman filter paper. Then, the sample was negatively stained with five µl of 10 mg/ml Uranyl acetate (SPI Supplies, PA, USA) and the excessive staining solution was again removed with the filter paper. Afterward, the grid was dried at room temperature. Electron micrographs were taken at an accelerating voltage of 80 kV.

2.3.2.4 Polydisperse radius disc (PRD) model

In regards to nanodiscs, the scattering pattern can be described by a polydisperse radius disc (PRD) model, where the thickness, t (= 2H) of the discs is assumed constant (only a function of temperature) and the radii, r of the discs follow the Schulz distribution (as shown in Scheme 2.1). As a result, the size averaged form factor, $P_{PRD}(q)$ of the PRD model is mathematically described by the following equations:

$$P_{PRD}(q) = \int_0^x \frac{1}{V_{PRD}} f(r)dr \int_0^{\pi/2} A^2{}_{PRD}(q,\alpha)\sin\alpha d\alpha \quad , \tag{1}$$

$$A_{PRD}(q) = 2V_{PRD}(r_{lip} - r_{D_2O}) j_0(qH\cos a)\frac{J_1(qr\sin a)}{(qr\sin a)},$$

Where □□is an angle between bilayer normal and scattering vector, q. V_{PRD} and $A_{PRD}(q)$ represent the volume of the individual disc and the scattering amplitude of the nanodisc, respectively. The

functions $J_1(x)$ and $Jo(x)$ are the Bessel function of the first kind and $\frac{sinx}{x}$, respectively. Eq. (1) includes the average over all possible orientations and various size of discs according to Schulz distribution, $f(r)$ as expressed below.

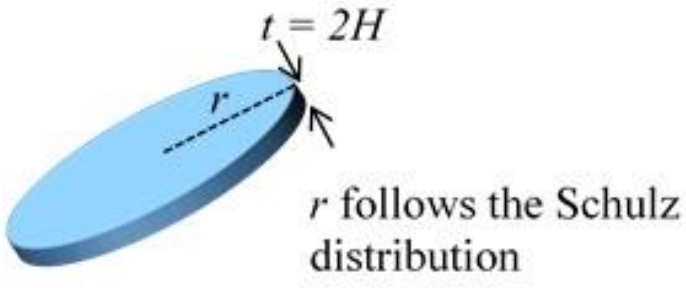

Scheme 2.1. A sketch of the disc with a thickness of t (=2H) and a radius of r.

$$f(r) = (z+1)^{z+1} r^{z} \frac{\exp[-(z+1)r]}{r\Gamma(z+1)}$$

$$V_{PRD} = \pi r^2 t(\frac{z+2}{z+1})$$

$$z = (1/p^2) - 1$$

$$t = 2H$$

Where p is the polydispersity of the size defined by $\sigma_R/\langle R \rangle$ with σ_R and $\langle R \rangle$ being the standard deviation and average of r.

2.3.2.5 Oblate Single-Shell (OSS) Model

The oblate single-shell (OSS) model (with two identical long-axes and one short-axis) was used to fit the SANS data as shown in Scheme 2.2. This model contains four independent parameters to describe the dimension of the particle, namely the major (r_{bi}) and minor (r_{ai}) axes of the core and the major (r_{bo}) and minor (r_{ao}) axes of the shell.

The form factor and scattering amplitude of OSS model, i.e., $P_{OSS}(q)$ and $A_{OSS}(q)$ can be expressed as follow

$$P_{OSS}(q) = \frac{1}{V_o}\int_0^1 \left|A_{OSS}(q, r_i, \beta)\right|^2 d\beta \quad \text{And}$$

$$A_{OSS}(q, r_i, b) = 3(r_{D_2O} - r_{lip})\left[\frac{V_i j_1(u_i)}{u_i} - \frac{V_o j_1(u_o)}{u_o}\right]$$

Where core and total volumes (V_i and V_o) can be mathematically derived as

$$V_i = (4\pi/3)r_{bi}^2 r_{ai} \text{ and, } V_o = (4\pi/3)r_{bi}^2 r_{ai}$$

$$u_i = q[r_{bi}^2(1-\beta^2) + r_{ai}^2\beta^2]^{1/2},\ u_o = q[r_{bo}^2(1-\beta^2) + r_{ao}^2\beta^2]^{1/2} \text{ and}$$

$$j_1(x) = (\sin x - x\cos x)/x^2,\ b = \cos a.$$

It should be noted that the OSS model assumes monodisperse particles and the peak smearing in the SANS patterns is mainly due to the different lengths and shell thicknesses along the long- and short- axes.

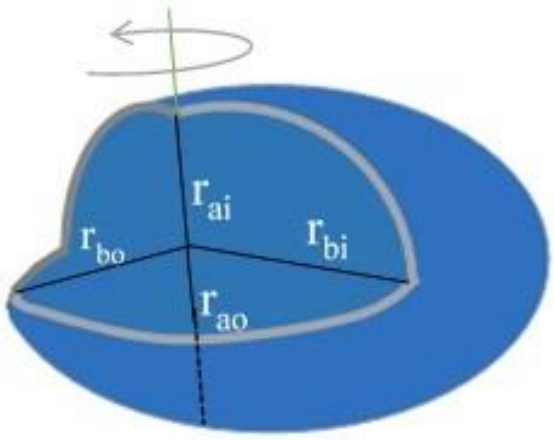

Scheme 2.2. A sketch of OSS model with the inner minor radius (r_{ai}) and major radius (r_{bj}), and an outer minor radius (r_{ao}) and an outer major radius (r_{bo}).

2.3.3 Nanoparticles Stability Assay (Thanks to Dr. Anu & her group)

To study the stability of the nanoparticles in the presence of serum, NPs of 1 mg/ml were either

labeled with NR or NBD-PC (a green dye with lipid tails). NPs (12 μmole Pi/ml) were incubated with either HEPES-buffered saline (HBS) or fetal bovine serum (FBS) at a volume ratio of 1:1 (NP solution: buffer) at 37°C for 2 hours. Samples were then fractionated using a size exclusion gel chromatography column (Sepharose CL-6B, 1x40 cm, 40 ml bed volume) pre-equilibrated with HBS. Eluted NPs (and/or any released dye) were collected as 1 ml fractions (total 40 fractions) to analyze fluorescence and the lipid content following the protocol described in previous articles.[132, 133] Fluorescence was measured using a fluorescent microplate reader (SpectraMax M2, Molecular Devices, Sunnyvale CA, USA). Filter settings (Ex/Em) of 450/530 nm and 530/605 nm were used for NBD-PC and NR, respectively. 100% fluorescence was obtained after addition of TX-100 (0.02%, final concentration). The recovery of lipids in the fractions was determined by measuring inorganic phosphorus (Pi).[132]

The time-dependent changes in fluorescence of NPs were measured at 37°C. The initial 10 mg/ml NPs (nanodiscs or vesicles) in either water or NaCl solution (140 mM) were further diluted with either FBS or HBS at 1:1 ratio (v/v). Diluted samples were placed in triplicate in a 96-well plate (0.2 ml per well). Fluorescence was measured at zero time, 2 hours and after addition of TX-100 (0.05% final concentration w/v) using the same filter setting as the previous experiment.

2.3.4 Cytotoxicity Assay

CCRF-CEM, KB, and OVCAR-8 cells were used for *in vitro* cytotoxicity analysis of the self-assembled lipid nanocarriers using an MTS assay. 10^4 cells/well were plated overnight in a 96 well plate. The NPs were diluted in the media to a final concentration ranging from 0.2 to 1.00 mg/ml in the final volume of 50 μl and incubated with cells in triplicate. The following controls were used: positive control = NPs + cells + MTS, blank = untreated cells + MTS, and negative control = medium + MTS. After incubation with NPs at 37°C for 48 hours, assays were performed by

adding the MTS reagent solution to culture wells and incubation continued for 4 hours. The absorbance (at 490 nm) was then recorded using a microplate reader. To calculate the percentage of cells density, the following formula was used: Cell density= optical density (OD) sample - OD blank, then the average of the triplicate sample ODs was calculated. The sample OD from untreated cells (blank) was set to 100%, then the percentage of cell density for treated cells was calculated by the following ratio: (OD untreated sample (100)/OD sample) *100.

2.3.5 Cellular Uptake Visualization and Quantification

FACS was performed on CCRF-CEM, KB, and OVCAR-8 cells after incubation with NPs to study cellular uptake and energy-dependent endocytosis. Cells were seeded in a 24 well tissue culture plate 24 hours before the tests. Cells were then incubated with NPs in lipid concentration of 1.00 mg/ml at 4 and 37°C for 2 hours. For adhering cells, e.g., KB and OVCAR-8 cells were first trypsinized and collected, while CCRF-CEM, a suspension cell, was collected directly. All cells were then washed and re-suspended using Dulbecco's Phosphate-Buffered Saline (DPBS). FACS experiment was conducted using a BD Biosciences FACSCalibur flow cytometer. All experiments were performed in triplicates. Emitted light results from NR-labeled nanoparticles was detected by the FL-2 detector. To calculate the background fluorescence of unlabeled cells, cells without any addition of nanoparticles were carried along as a negative control in every measurement. For whole-cell analysis, 10^4 cells were counted. Data analysis was performed with BD CellQuest Pro (BD Biosciences, Heidelberg, Germany).

The visualization of the NPs uptake by cells was conducted using a Nikon A1R confocal microscopy using a 60 x oil immersion lens. Image acquisition and analysis were performed using Nikon Elements Ar software. The procedure followed the same incubation conditions for the FACS quantification. Before imaging Hoechst 33342 was applied to stain the nuclei. The intensity of

the laser beam and the photodetector sensitivity were kept constant to compare the relative fluorescence intensities between experiments.

2.3.6 Mechanisms of Cellular Uptake

The relative level of nanoparticle uptake was assessed via FACS. CCRF-CEM cells were incubated with endocytosis inhibitors for 30 minutes according to the concentrations of the inhibitors listed in (Table 2.1).

NR-labeled NPs in the concentration of 1.00 mg/ml was then added, and the incubation continued for 1.5 hours. After that, cells were washed and resuspended in DPBS. Measurements on the cells treated by NPs in the absence of inhibitors were taken as the positive controls and compared with those of cells incubated with specific inhibitors and NPs. Concentrations of inhibitors were obtained based on 90% cell viability test of each inhibitor after 2 hours of incubation.

Inhibitors	Inhibited mechanism	Concentration
Chlorpromazine	Clathrin	140 μM
Filipin III	Caveolae	7.6 mM
Cytochalasin D	Macropinocytosis	10 μM
Amiloride	Macropinocytosis	800 μM
Wortmannin	Macropinocytosis	10 μM
Nocodazole	Microtubules	35 μM

Table 2.1.List of pharmaceutical inhibitors: The concentration of each pharmaceutical inhibitor used to determine the internalization mechanism of nanodiscs and nanovesicles.

2.4 Results and discussion

2.4.1 Nanoparticles characterization

The structures and polydispersity of the NPs were characterized by SANS, DLS, and TEM and are consistent with the previous report where nanodiscs self-assembled in a homogenized mixture of DPPC/DHPC/DPPG/DSPE-PEG2000 in PBS at room temperature.[45, 134] The nanodiscs were proven to be stable if kept at temperatures lower than the melting transition temperature of

DPPC (i.e., 41°C). They underwent a disk-to-vesicle transformation, which is irreversible in the sample at low lipid concentrations (≤ 1 mg/ml), i.e., the vesicular structure retained after being cooled down to the room temperature.[134] The hydrophobic core of the lipid bilayer can entrap hydrophobic or amphiphilic molecules, e.g., NR and NBD-PC in the bilayer. The DLS data (Figure 2.1 A) showed well-defined hydrodynamic diameters (D_H) of the two chemically identical samples (one not being heated and the other after being heated at 50°C for overnight) at 25°C. The D_H values obtained in unheated, and post-heated samples are 21 and 34 nm, respectively, representing nanodiscs and vesicles independent of NR or NBD-PC content. Since DLS did not elucidate detailed structural information, SANS measurements were also performed to investigate the detailed structures of the NPs. (Figure 2.1 B) Shows the SANS data of a 1.0 mg/ml DPPC/DHPC/DPPG/DSPE-PEG2000 unheated and the same post-heated samples, respectively. Distinct SANS patterns are observed for these two samples, indicative of different structures. The SANS curve of *unheated* sample shows a low-q asymptotic plateau (q being the scattering vector defined as $\frac{4\pi}{\lambda}\sin\frac{\theta}{2}$, where λ and θ are the wavelength of the neutron and the scattering angle, respectively) followed by a monotonic decay. A polydisperse discoidal model could best fit the data with an average diameter and bilayer thickness of 21.0 and 5.4 nm, respectively – consistent with the characteristic of DPPC bilayer structure. The fact that the negatively-stained TEM images reveal the plane and edge of discs further confirm the disk-like structure described by the SANS model (Figure 2.1C).

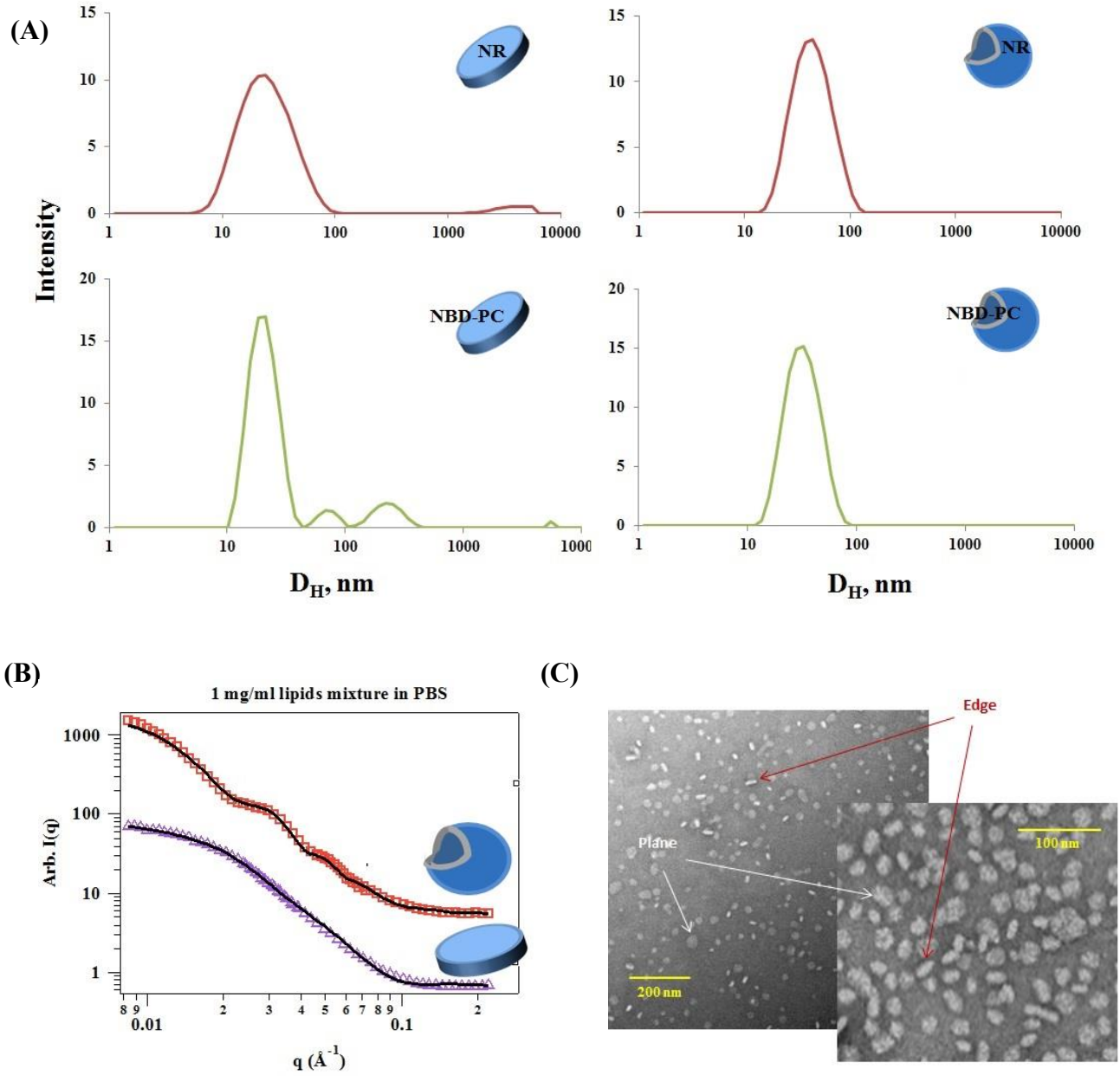

Figure 2-1.Structural characterization of the nanoparticles: (A) The distributions of hydrodynamic diameter, DH of NPs prepared in PBS by DLS. Three measurements at 25°C were taken on each sample, and the data were averaged and plotted as intensity-weighed distributions. (B) SANS data of the nanodiscs (purple triangles) at 37°C and the oblate vesicles after annealed at 50°C (red squares) with a lipid concentration of 1.0 mg/ml in PBS and their best fits (black curves) using the discoidal model and oblate vesicular models, respectively. (C) The negatively staining TEM micrographs of nanodiscs at different magnifications. The white and red arrows represent the plane and edge of the nanodiscs, respectively.

The SANS pattern of the same *post-heated* sample transforms into a curve with several weak

oscillations originated from the high contrast between the vesicular shell and interior/exterior solution as well as the low polydispersity of the vesicular radius. It has been previously established that the SANS pattern is a unique scattering feature of core-shell vesicular structure in literature.[43-45, 131, 135] The SANS data was best fit by an oblate vesicular model with the outer long- and short- axes of (34.2 ± 0.5) and (12.0 ± 0.3) nm, respectively. Neither aforementioned discoidal model nor other single-morphology, e.g., cylindrical, spherical and vesicular models provides reasonable fits with sensible physical parameters. TEM was not applied to examine the structure because vesicles do not survive at high vacuum and a cryogenic stage is not available at the facility. Based on the same transition and morphology which were observed and reported previously, the oblate vesicles are identified with high certainty.[45, 134] The interpretation of SANS results is also supported by the hydrodynamic diameters obtained from the DLS measurements (Figure 2.1 A).

It should be noted that both NPs (nanodiscs and vesicles) are made of biologically relevant components which have the identical compositions. Moreover, their sizes are similar (< 50 nm), and each has a low polydispersity. Therefore, this system enables us to study the shape-dependent of NPs on cellular internalization.

2.4.2 Stability of NPs in Serum

Before the *in vitro* cell study, the stability of the NPs must be examined to confirm that most the NPs will not alter their morphology, and the entrapped dye (NR or NBD-PC) does not dissociate from the NPs. It has been well known that PEG-conjugation (PEGylation) on the surface of NPs can effectively reduce the uptake by the reticuloendothelial system (RES) and the non-specific interactions between the NPs and the plasma proteins, thus increasing the circulation half-life of the NPs.[136, 137] Therefore, DSPE-PEG2000 was also incorporated with the lipid NPs to

suppress the lipid/plasma protein interactions in this study. Moreover, it has been reported that the bicelle-type nanodiscs tend to coalesce with each other after dilution.[45, 138, 139] The addition of DSPE-PEG2000 can effectively inhibit the disc coalescence due to the steric effect of PEG. To examine the stability of these lipid NPs and their interactions with serum, NP solutions containing FBS was investigated. The NR-containing NPs (either nanodiscs or vesicles) were incubated at 37°C with either FBS or HBS, and the release of the fluorophore was measured at a given period as shown in (Figures 2.2 A, and B). Two high-concentration NP solutions (100 mg/ml) were first prepared in either water or 140 mM NaCl saline, respectively, as stock solutions. Afterward, the stock solutions were diluted using either FBS or HBS solution to form a solution with lipid concentration of 1 mg/ml.

The retention of NR or NBD-PC from the nanodiscs was monitored based on fluorescence intensity initially (t = 0) and after 2 hours of incubation. Fluorescence measurements were also conducted on the samples with the addition of Triton-X100 (TX-100), a detergent commonly used to destabilize vesicles. The nearly invariant fluorescence in (Figure 2.2 A) indicated that the entrapped NR was most likely intact under all conditions. To further confirm the stability of nanodiscs in FBS and HBS, a time-resolved fluorescence experiment was conducted over 24 hours, and the results are shown in (Figure 2.3). The same type of experiment was also carried out on the nanodiscs and vesicles incorporated with a trace amount of NBD-PC, which is well integrated with PC lipids and thus can be considered as part of the bilayer. The fluorescence of both NBD-labeled nanodiscs and vesicles (Figure 2.2 A) also shows no noticeable differences in the presence or the absence of FBS as well as after the addition of TX-100. Thus, we can conclude that both nanodiscs and nanovesicles can entrap hydrophobic or amphiphilic molecules with high stability.

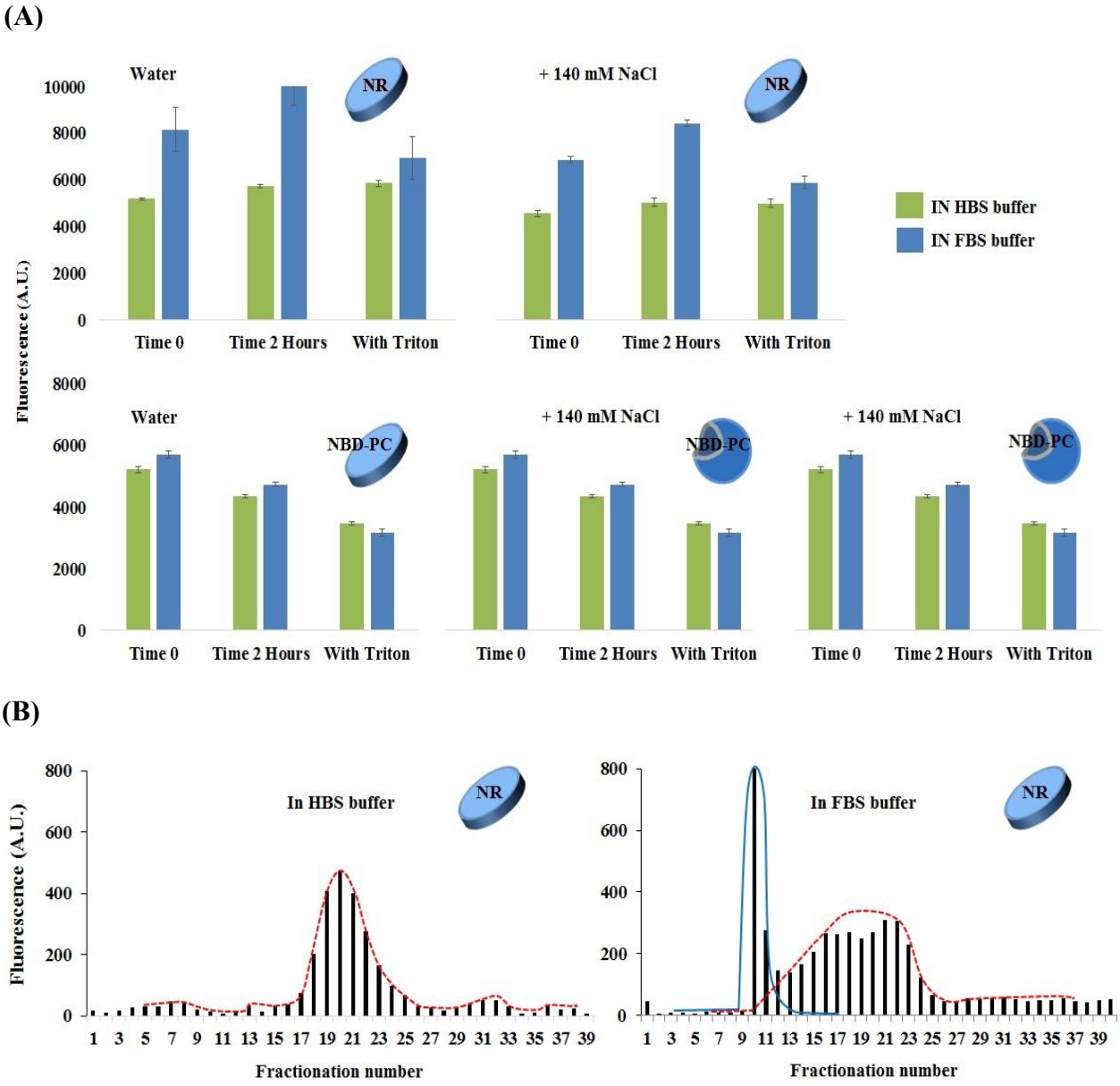

Figure 2-2. NPs stability in saline and serum: The fluorescence of NPs before and after being incubated in the presence (blue bars) and absence (green bars) of FBS at 37˚C for 2 hours and then treated with TX-100. The standard deviations of three measurements within a single experiment are used as the error bars. The results of (A) NR-containing nanodiscs and NBD-labeled nanodiscs and vesicles in the stock solutions which initially prepared in either water or 140 mM NaCl saline. (B) Fractionation and elution profiles of NP-containing nanodiscs after being incubated in the absence (left, HBS) and presence (right) of FBS for 2 hours at 37˚C. The nanodiscs in HBS were eluted from fractions 16 to 25 (dotted red line). FBS also yielded fluorescence signal and was eluted from fractions10 to 13 (solid blue line). The nanodiscs in FBS had a wider distribution and were eluted from fractions 12 to 25 (red dotted line).

Although neither NR nor NBD-PC fluorescence was significantly affected after incubation with FBS, the possible change in the morphology of NPs cannot be ruled out. In the case of lipid NPs, the morphology normally correlates with the size of the NPs. Therefore, we examined the structural variation of NPs in serum using a size exclusion column. Both serum-treated (2h in FBS) and non-serum (control, 2h in HBS) samples were fractionated by a Sepharose CL-6B size exclusion column,[132, 133] and the NR fluorescence of each fraction was determined. (Figure 2.2 B) Indicates that NR-containing nanodisc after being incubated in HBS saline (in the absence of FBS) were eluted from fractions 16 to 25 (guided by the dotted red curve). It should be noted that in the presence of FBS, a sharp fluorescence signal was observed in fractions 10 to 13, presumably contributed from the proteins in FBS (guided by the solid blue curve). The nanodiscs after incubation with FBS were eluted in a slightly wider spectrum (guided by the red dotted line from fractions 12 to 25). A parallel experiment was also carried out using NBD-PC labeled NPs (both nanodiscs and vesicles). The results in (Figure 2.4) show similar fractionation patterns as those of NR labeled NPs. Both fluorescence measurements and fractionation experiment demonstrate the high stability of both NPs in the presence of serum proteins.

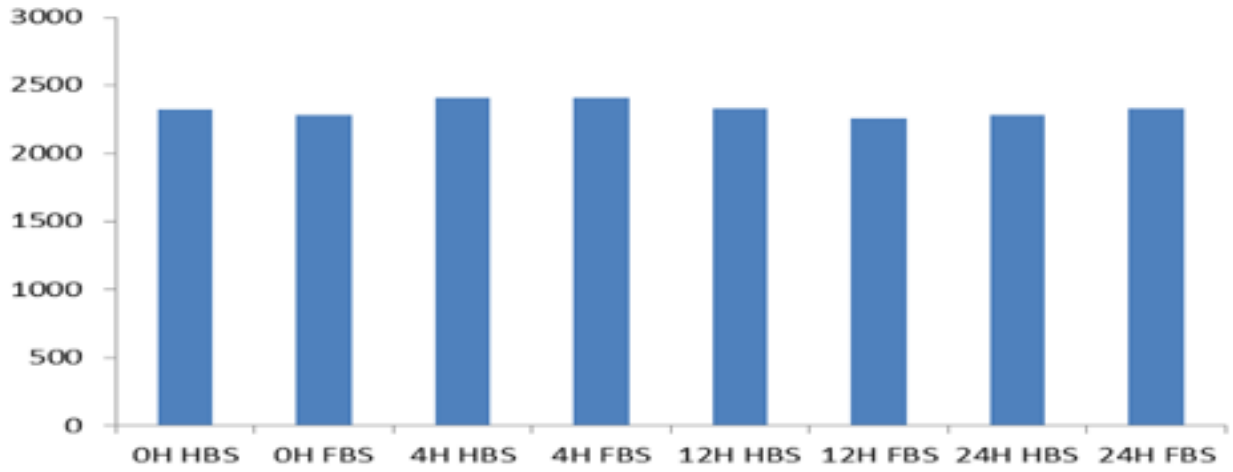

Figure 2-3. The fluorescence of NR encapsulated ND after being incubated in with FBS serum and with HBS (control) at 37˚C for 24 hours. Absorbance was measured at different time points.

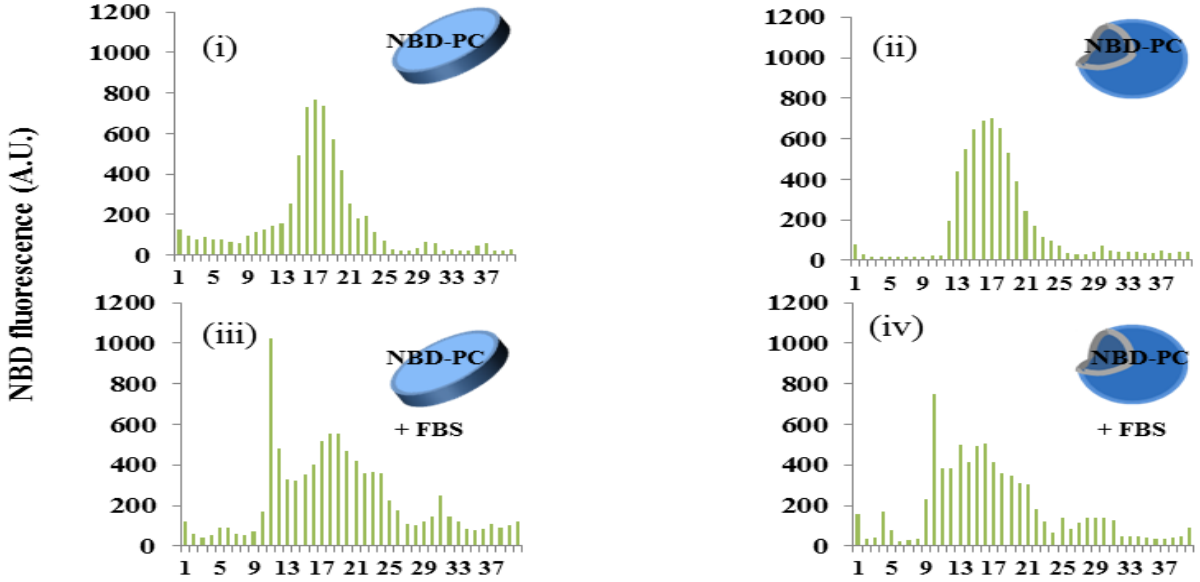

Figure 2-4. The NBD-PC containing NPs after being incubated in the absence [(i) and (ii)] and presence [(iii) and (iv)] of FBS for 2 hours at 37˚C. The nanodiscs are presented in (i) and (iii), while the vesicles are (ii) and (iv).

Also, known aliquots from various fractions were analyzed for inorganic phosphorus (Pi) as well as Nile Red or NBD fluorescence in triplicate, and the fluorescence associated per Nmol Pi was determined.[140]

To assess any non-specific contributions from the FBS, control samples (*without* nanoparticles) containing 1:1 ratio of FBS/HBS (v/v) were also fractionated on the column. The fractions corresponding to nanodiscs and vesicles elution were analyzed for fluorescence and Pi (F: Pi) ratios obtained typically from fractions 19-21 of the nanodiscs or vesicles. As seen in Table 2.2, there was non-specific fluorescence attributed to the serum proteins. However, tiny Pi above background levels was detected by the high ratios of F: Pi ratios. Our data also suggests that an increase in the ratios of F: Pi in FBS incubated nanoparticles is partly due the serum contributions. The further detailed analysis will be required to dissect out this effect.

Sample Tested	Relative Fluorescence Units/Nmol Pi (F: Pi)	
	HBS	FBS
NR ND (water)	17.17±6.21	35.97±6.17
NR ND (NaCl)	16.40±6.30	35.14±0.03
NBD ND (water)	22.69±6.30	40.68±3.45
NBD ND (NaCl)	24.33±5.27	44.25±1.04
NBD vesicles	24.66±4.30	35.60±2.50
FBS alone (NR)	N.D.	88.29±16.32
FBS alone (NBD)	N.D.	302±52.50

Table 2.2. Determination of Fluorescence: Phospholipid (F: Pi) ratios in nanoparticles fractionated by size-exclusion chromatography. Values presented are the average (±S.D.) of F: Pi ratios obtained column peak fractions (typically fraction 19-21) of the nanodiscs or vesicles.

2.4.3 Nile red profile in chloroform

It should be noted that the local high NR concentration in one NP is possibly greater than the onset concentration of the NR self-quenching. If this occurs together with the leakage of the entrapped NR into the aqueous phase, the fluorescence may increase at a lower NR concentration. To verify that our experimental condition does not correspond to such scenario, fluorescence measurements are also taken in NR/chloroform samples at different NR concentrations (covering the highest possible NR/lipid weight ratio ~ 1/1000) because NR does not fluoresce in aqueous solutions. (Figure 2.5) also shows a linear fluorescence response with the NR concentration, indicating that the NR in NP is below the onset of NR self-quenching concentration in the organic environment.

2.4.4 Cytotoxicity analysis

To examine the effects of the nanoparticles on cells viability, various concentrations of NPs were incubated with CCRF-CEM, KB, and OVCAR-8 cells up to 48 hours at 37˚C. Data presented in (Figure 2.6) indicates that the cell viability is not affected by the presence of either nanodiscs or vesicles. It further confirms that the presence of NR in the lipids constituting is not toxic to the

cells.

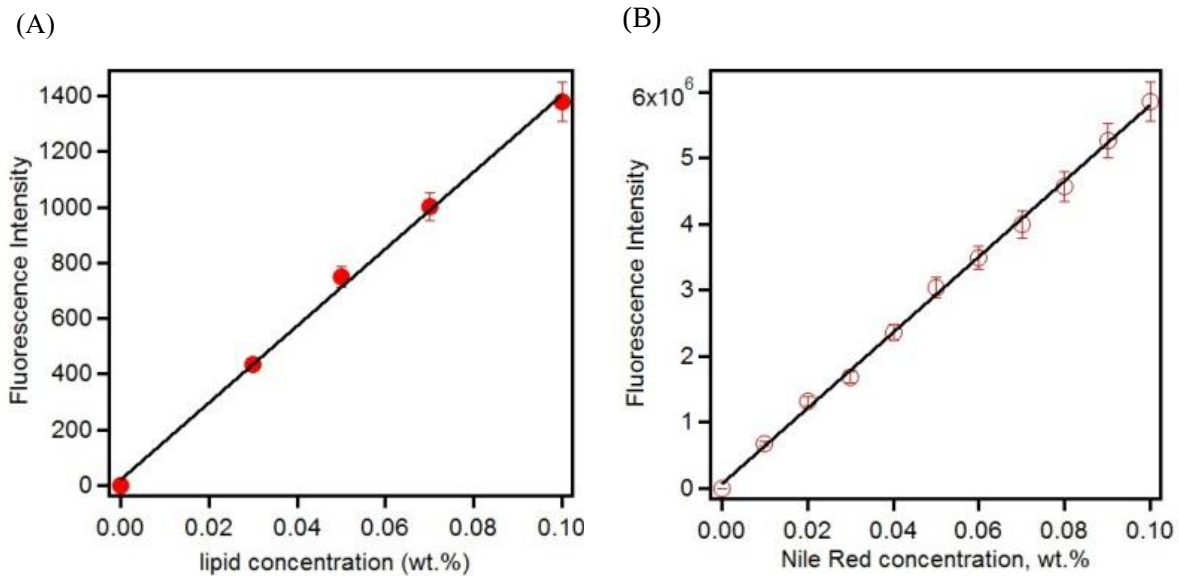

Figure 2-5. (A) The fluorescence of the NR-containing lipid mixtures (Nile Red–to-lipid weight ratio = 1/1000) as a function of lipid concentration and (B) The fluorescence of NR in chloroform as a function of NR concentration up to 1/1000 by weight. Both indicate linear relationship as well as passing through the origin indicative of negligible self-quenching.

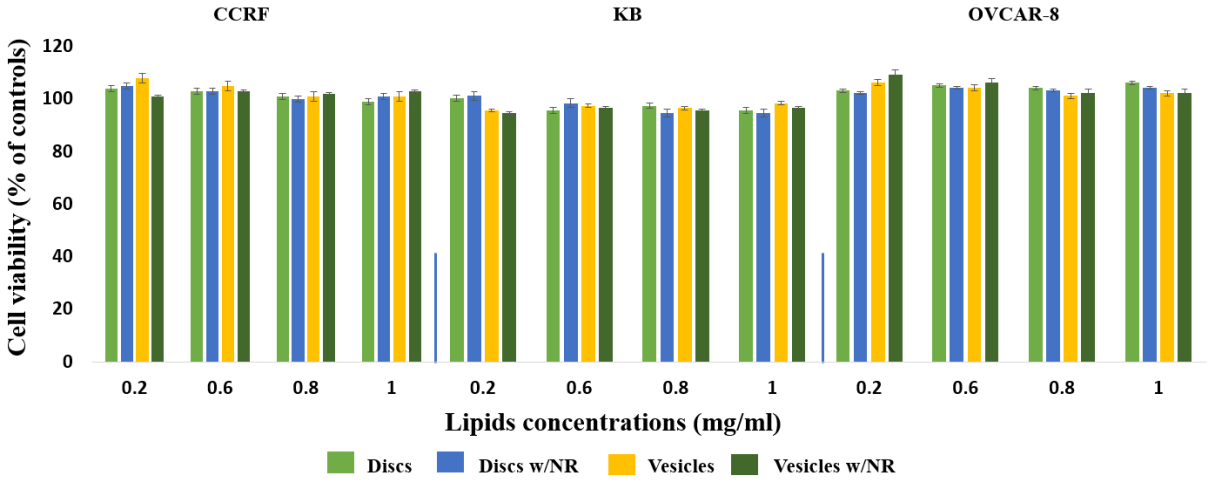

Figure 2-6. Cell viability assay: To study the effect of NPs (nanodiscs and vesicles) on the viability of cells, cells were incubated with various concentrations of nanodiscs or vesicles for 48 hours (in triplicate), and cell viability was determined. Values are expressed as a percentage of viable cells where the control samples (i.e., without the addition of nanoparticles) are considered 100% viable. The values are averages of 3 measurements (±S.D.). The results were reproducible from two independent experiments.

2.4.5 Cellular Uptake of NPs

It has been reported that the cellular internalization of the NPs significantly changes according to the cell line.[141] Therefore, three different cell lines, CCRF-CEM, KB, and OVCAR-8 were investigated after being incubated with a solution containing either nanodiscs or vesicles. The cellular uptake under various experimental conditions was revealed by FCOM and FACS. The fluorescence intensity from either FCOM or FACS can be directly correlated with the quantity of cellular uptake under the assumption of negligible self-quenching of the fluorophore. (Figure 2.5) Shows linear fluorescence response of the NR-containing lipid mixture as a function of lipid concentration up to 1.0 mg/ml, indicative of a negligible self-quenching effect of NR. The FACS results of CCRF-CEM cells after being incubated with NPs (i.e., vesicles and nanodiscs individually) at 37˚C for 2 hours are illustrated in (Figure 2.7), which indicates that the internalization of nanodiscs was significantly higher for all three cell lines. The peak represents the highest NP population of the specific fluorescence intensity, which is presumably proportional to the cellular uptake. The fluorescence peak intensities of vesicles in the cases of CCRF-CEM, KB, and OVCAR-8 were 50, 13 and 50, respectively. In comparison to those of the nanodiscs, 380, 200 and 600, implying that the internalization of nanodiscs is about 7 to 15 times of that of vesicles regardless of the cell lines. This observation suggests that nanodiscs are presumably a more efficient carrier to deliver molecules to cancer cells.

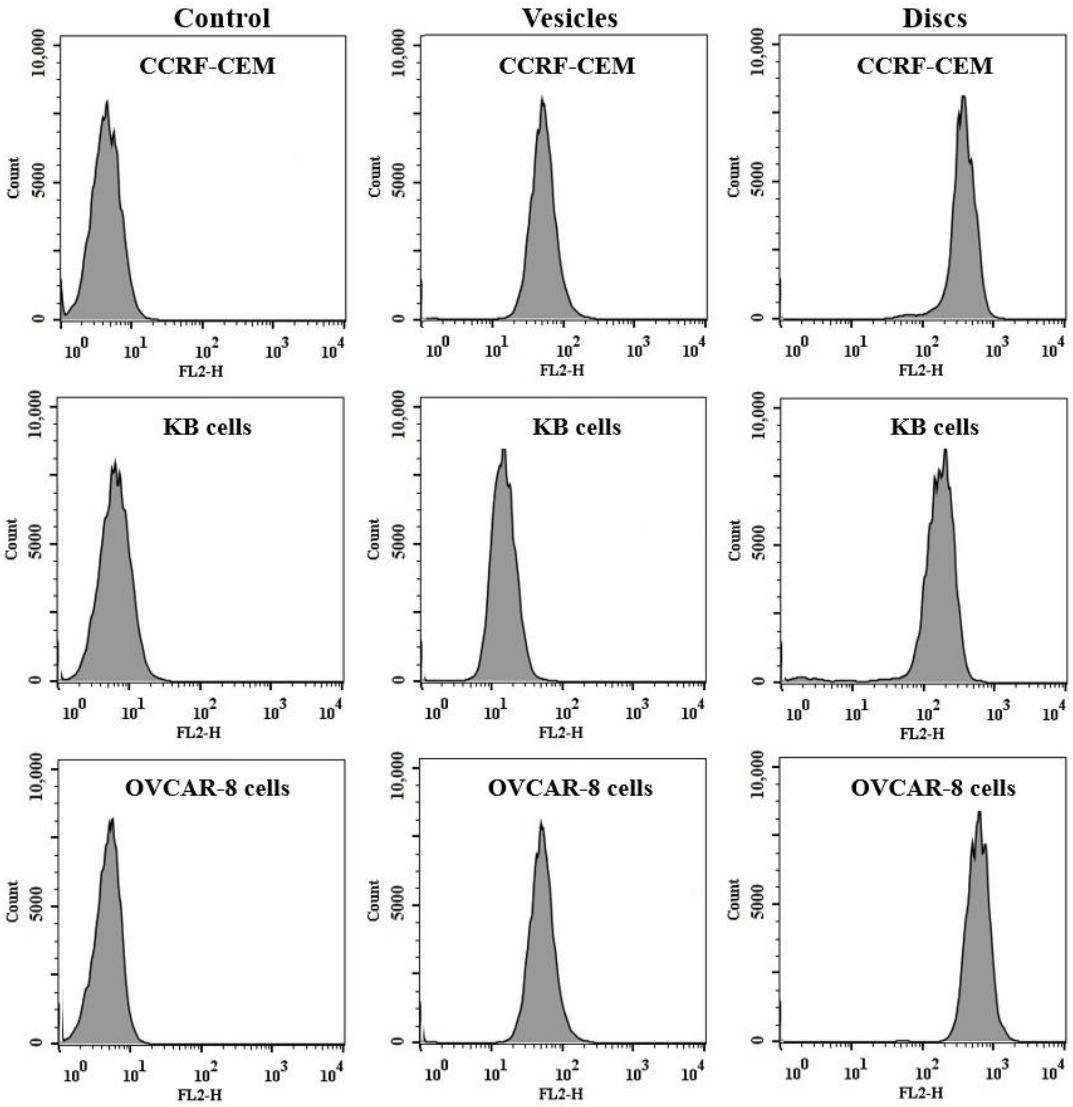

Figure 2-7. Flow cytometry results of cellular uptake: Representative flow cytometry histogram to quantitatively assess the uptake of nanoparticles after incubation for 2 hours at 37˚C: the first column of untreated cells (controls), the second column for cells treated with vesicles, and the third column for cells treated with nanodiscs. Nanoparticles in all cells show lower cellular uptake of vesicles as compared with the results of nanodiscs.

The preferred internalization of the nanodiscs was further supported by the FCOM images as shown in (Figure 2.8), where all cells exhibited the highest fluorescence in the case of nanodiscs as compared to the vesicles. The dataa acquired from FCOM were consistent with the results obtained from the FACS indicating that the cellular uptake of nanodiscs by all cells under study is

significantly higher than that of vesicles, confirming the strong dependence of internalization on morphology.

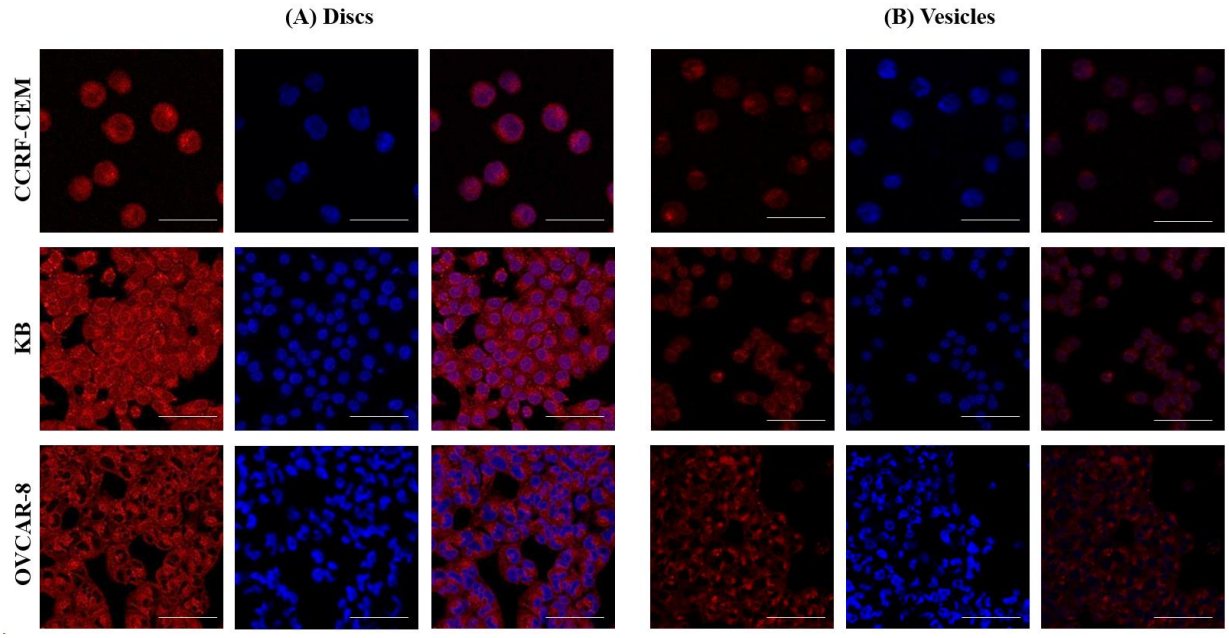

Figure 2-8. Fluorescence confocal micrographs: Confocal microscopy images of CCRF-CEM cells in the first row, the second row, represents KB cells, and the third row shows OVCAR-8 cells. All images were taken after incubation with the NR-contained (A) nanodiscs and (B) vesicles, respectively, at 37°C for 2 hours. The nuclei of the cells were dyed with Hoechst (blue). Three images were obtained in each case are illustrated: cells with NR (red), nucleus blue (Hoechst), and merged (both blue and red). Clear internalization of the NPs is observed. Moreover, the NR fluorescence intensity is found lower in the case of vesicles compared to nanodiscs. Scale bar is 50 μm.

To estimate the number of NPs being internalized in the cells, the ratio of NPs associated with the cells to those which remained in solutions were investigated through fluorescence. (Figure 2.9 A) Shows the fluorescence of the total amount of NP dispersion before their incubation with the CCRF-CEM cells and the fluorescence remained associated with the cell pellets obtained from the centrifuged cells after being incubated with NPs. The initial fluorescence values of the nanodisc dispersion are found to be similar to that of the vesicle dispersion, indicating that the morphology of NPs has no effect on the fluorescence intensity. In the case of NP concentration applied (i.e., 1.0 mg/ml), 19.2% of the original nanodiscs fluorescence was found associated with the CCRF-

CEM cells, while only 8.4% of the initial fluorescence associated with the cells in the case of vesicles under the identical experimental conditions. The result of the morphological dependence on lipid concentration is shown in (Figure 2.9 B), suggesting that the difference in uptake increases with increased NP concentrations (i.e., 1.0 mg/ml shows more uptake compared with 0.5 mg/ml and 0.25 mg/ml).

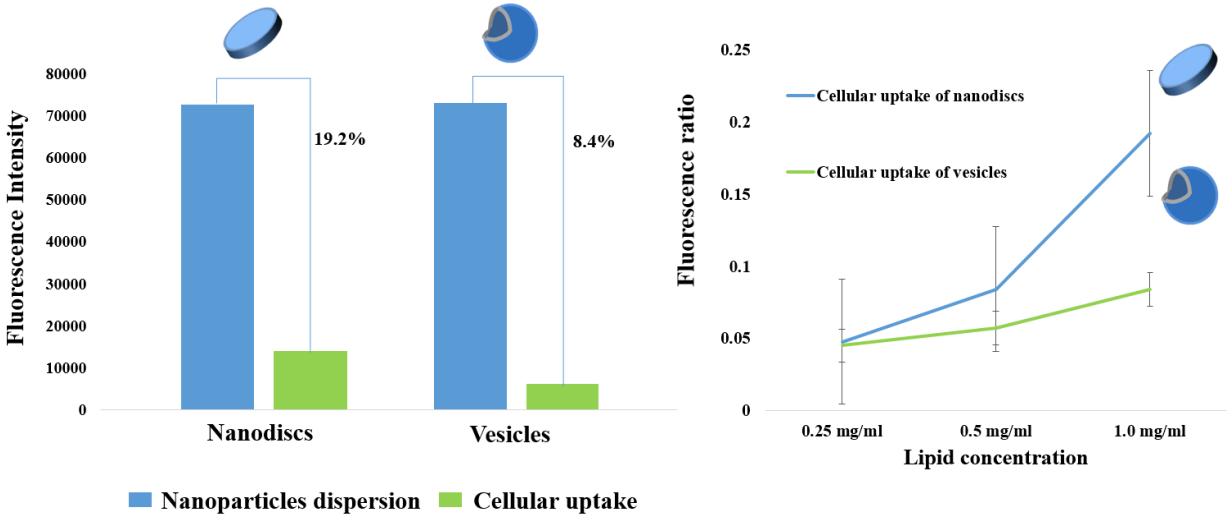

Figure 2-9. Quantification of the uptake: (A) The fluorescence of the 1.0 mg/ml nanodisc and vesicle dispersions (blue) as well as the fluorescence from the cell dispersions after the incubation with the nanoparticles for 2 hours (green). (B) The ratios of fluorescence readout from the re-dispersed cell suspension to that of NP dispersions as a function of lipid concentrations.

The results shown in (Figures 2.7,2.8, and 2.9) lead to the same conclusion that the cellular uptake of nanodiscs is higher than that of vesicles in all three cell lines presumably. A plausible speculation is that larger surface contact area is anticipated for discoidal morphology, providing a better opportunity for the NPs to interact with reasonably flat cell membranes.[46, 47, 142] While vesicles interact with the cell surface through the contact point (instead of the contact surface), thus significantly reducing the cellular uptake. Moreover, FCOM at different depths of the cell (Figure 2.10) indicates that a good portion of nanodiscs was indeed internalized in the cell.

(A) Nanodiscs

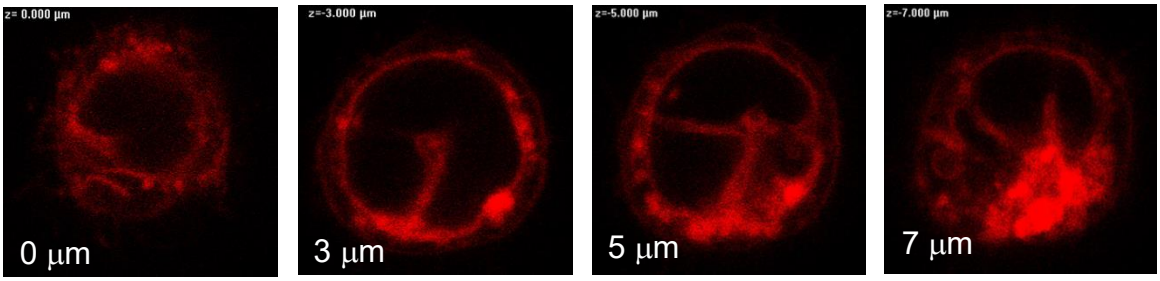

(B) Vesicles

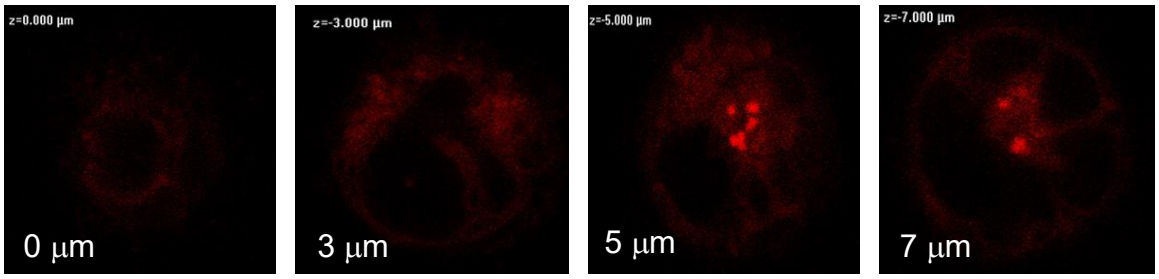

Figure 2-10. The FCOM of a CCRF-CEM cell being incubated with NR-containing (A) nanodiscs and (B) vesicles (NR-to-lipid weight ratio = 1/1000), respectively over a range of depths from 0 to 7 µm.

2.4.6 Intactness of Nanodiscs before the Uptake

It was speculated that NR might dissociate from the nanodiscs before the cellular uptake. Therefore, the intactness of the NR-containing nanodiscs is one of the research interests, providing the knowledge of the transfer mechanism of NR from nanodiscs to cells. To substantiate our observations and rule out the possible contributions of NR which was not entrapped by the nanodiscs, the cellular uptake studies of both NR and NBD-PC -labeled NPs were performed. Since NBD-PC can be well integrated into the DPPC lipid bilayer, by using different filters to allow individual color (red or/and green), we could identify the relative locations of NR and NBD-PC. The secure colocation of these two dyes indicates that the NR did not dissociate from the nanodiscs during the cellular uptake process (Figure 2.11).

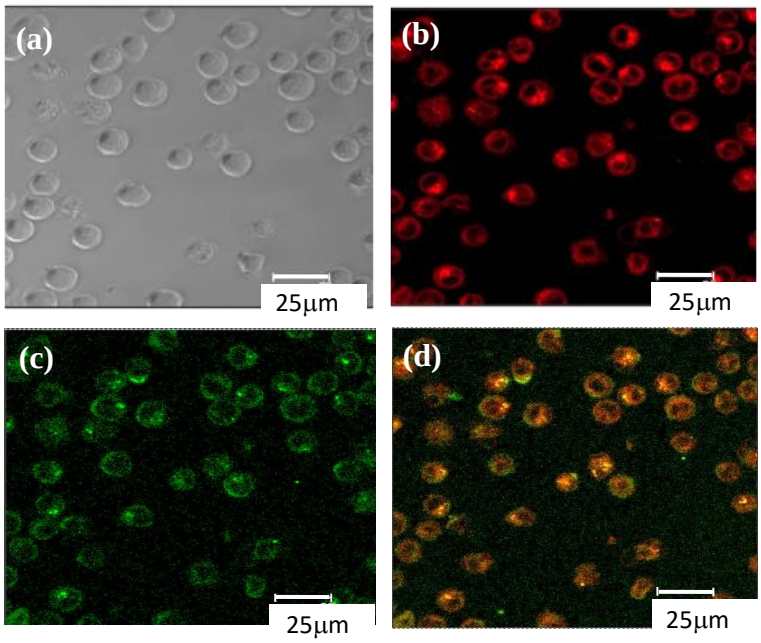

Figure 2-11. The fluorescence micrographs of CCRF-CEM cells after being incubated with both NR and NBD-PC containing nanodiscs under different configurations: (a) bright field, (b) red channel, (c) green channel and (d) both red and green channels. Strong colocation of NR and NBD-PC was observed.

2.4.7 Energy-Dependent Mechanisms of NPs Uptake

To advance our understanding of the NP uptake mechanism, several experiments were also conducted at 4°C. Presumably, the energy-dependent uptake would be obstructed due to the rigidity of the membrane resulting in inhibiting the passive internalization and effectively suppressing the endocytosis.[143] (Figures 2.12 A and B) Illustrate the fluorescence confocal microscopic micrographs and FACS results of CCRF-CEM cells after being incubated with 1.0 mg/ml vesicles or nanodiscs at 37 or 4°C for 2 hours. In the case of vesicles, greater cellular uptake was observed at 37°C than that at 4°C, suggesting strong energy dependent mechanisms of the vesicular uptake. Interestingly, the parallel experiment for nanodiscs only showed a slight decrease (< 10%) at 4°C in comparison to 37°C, suggesting that the cellular uptake of nanodiscs may follow a different mechanism from the energy-dependent endocytosis. Further investigation on possible mechanisms of the endocytosis of these two NPs was also taken to provide insights to the

differences in the cellular uptake as described in the following section.

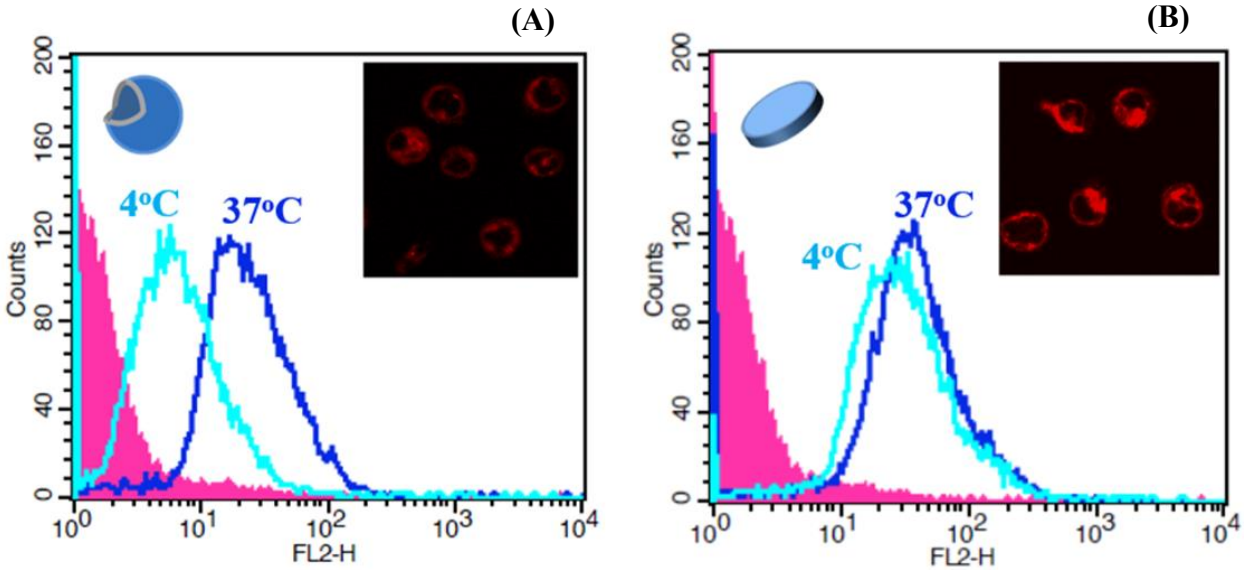

Figure 2-12. Energy-dependent uptake at 4˚C: The FACS and FCOM results of the energy-dependent cellular uptake after incubating CCRF-CEM cells with (A) vesicles and (B) nanodiscs at 37˚C (dark blue) and 4˚C (light blue) for 2 hours. The insets are the fluorescence confocal micrographs of CCRF-CEM at 4˚C.

2.4.8 Mechanisms of Uptake

Six pharmacological inhibitors (listed in Table 2.1 in the "Methods Section") were employed to investigate four cellular uptake mechanisms of both NPs. Specifically, chlorpromazine causes a reduction in clathrin adaptor complex protein from the cell surface and thus blocks the clathrin-mediated pathway.[144] Filipin III leads to the disruption of caveolar pits by inducing aggregation of cholesterol in the cell membrane.[144] Three reagents, Amiloride, wortmannin or cytochalasin D were individually applied to the cells to block the membrane ruffling and macropinocytosis.[144] Finally, nocodazole obstructs microtubule polymerization leading to vesicular transportation inhibition.[145]

Individual inhibitor concentrations were adjusted to achieve a minimum of 90% cell viability over 2 hours of incubation based on several previous protocols, and the results are presented in (Figure 2.13).

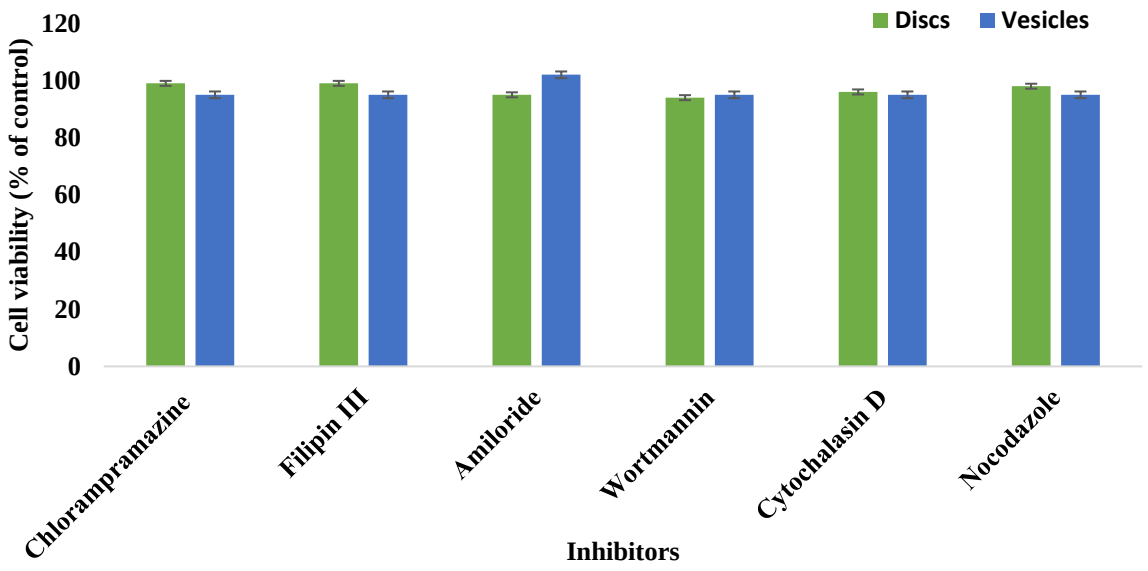

Figure 2-13. Viability assay to study the effect of inhibitors on cell viability after 2 hours of incubation. The data present a percentage of control sample which was not incubated with the inhibitors.

The FACS results of both NPs after incubation with CCRF-CEM cells are shown in (Figure 2.14). Evidently, both clathrin- and caveolae-mediated endocytosis were the major internalization pathways for both NPs. However, about 20% of nanodiscs were also internalized through macropinocytosis pathway and microtubule-mediated transportation, presumably attributed to the morphological variation. This observation is consistent with a recent report on the enhanced cellular uptake of disk-like hydrogel NPs in different cell types compared with those NPs of other shapes through the macropinocytotic pathway.[141] Another study also suggests that NPs of asymmetric shapes (i.e., worm-like micelles and cylinders) have a higher level of internalization through the macropinocytotic pathway than spheres.[142] Moreover, our result suggests a much lower cutoff size for the cellular uptake of vesicles than 200 nm as previously reported.[142] The results of pharmacological inhibitor provide the insight to the origin of the morphologically dependent mechanisms of cellular uptake. Multiple uptake mechanisms in addition to clathrin- and caveolae-mediated endocytosis are found for nanodiscs rather than vesicles. It also implies that

macropinocytosis and vesicular transportation may not be affected by low temperature considering (Figure 2.12). Therefore, the enhanced cellular uptake of nanodiscs is presumably due to the additional macropinocytosis and microtubule-mediated transport mechanisms.

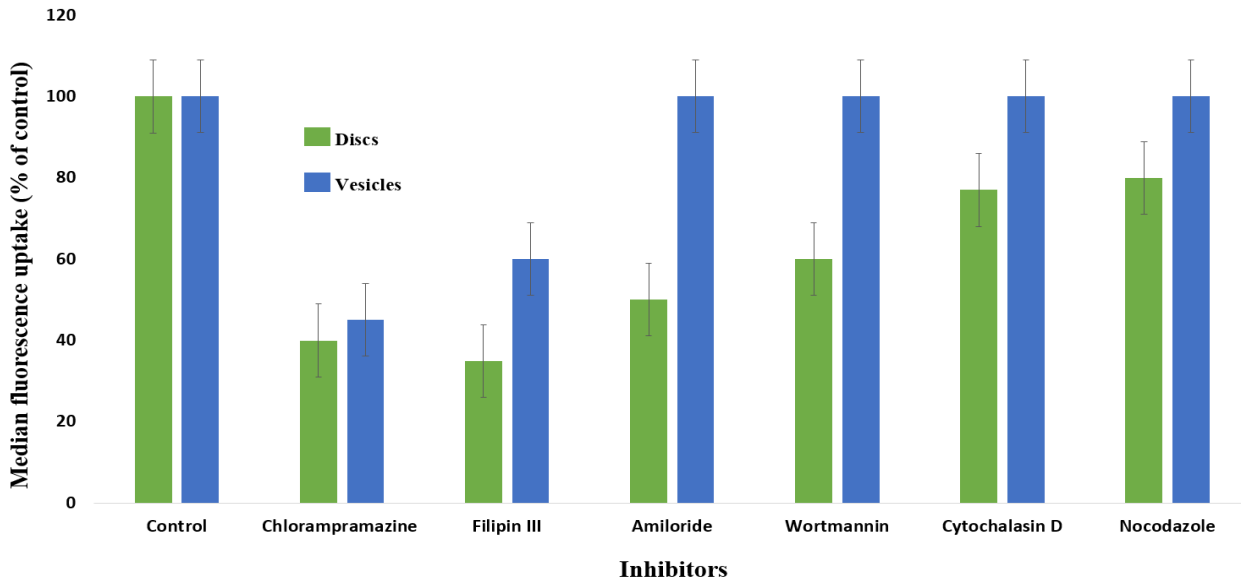

Figure 2-14. Mechanism of uptake: Median fluorescence as the CCRF-CEM cells incubated with the NPs (nanodiscs and vesicles) in the presence of various inhibitors. The uptakes of both NPs were suppressed in the presence of Chlorpromazine and Filipin III, while the uptake of vesicles was not affected by the other inhibitors unlike that of nanodiscs being suppressed in all cases.

2.5 Conclusion

This work first demonstrates uniform-sized nanodiscs and nanovesicles can be composed of the lipid mixture with *identical* chemical composition, enabling our study on the morphological dependence of the cellular internalization with no bias. It is evident that the morphology of nanoparticle plays a critical role in the cellular uptake of self-assembled lipid nanostructures. These NPs are structurally stable in the presence of serum and do not show cytotoxicity effect. In all cases (CCRF-CEM, KB, and OVCAR-8 cancer cell lines) nanodiscs illustrate significantly

higher cellular uptake than that of vesicles under the same conditions. Based on the study of endocytic mechanisms, the enhancement is presumably attributed to two main factors: (1) the larger surface contact area for the nanodiscs to interact with the cell membrane than that of the vesicles and (2) multiple pathways of cellular internalization (including macropinocytosis and microtubule-mediated transport) other than the typical clathrin- and caveolae-mediated endocytosis utilized by the vesicles. This study suggests a potential strategy regulating cellular internalization of nanoparticles by their morphological differences.

Chapter 3. Effect of Folate-Targeted Molecule on the Nanoparticles' Rate of Penetration into Cancer Cells

Abstract

Targeted therapies are developing as an ideal strategy for the treatment of cancer. Evaluating the impact of a high-affinity targeting ligand on the rate and extent of cancer cells penetration of different morphology of nanomedicine was performed. We have used fluorescence-activated cell sorting (FACS) and fluorescence confocal optical microscopy (FCOM) to quantitate the uptake of cancer cells of lipid-based self-assembles decorated with polyethylene glycols (PEG)-folate nanoparticles (NPs) prepared in two different shapes (discs and vesicles). We demonstrate that increasing of the cellular uptake of the discoidal folate NPs compared with the uptake of the vesicular and none conjugated NPs. Ligand Targeting eventually leads to increased cell accumulation, with endocytosis of the targeted nanocarriers contributing to enhanced delivery. Although, the results of the *in vivo* study on KB tumor-bearing mice by the Caliper IVIS system followed the same trend of the *in vitro* cell study were folate disc > folate vesicle > none folate disc > none folate vesicle, however, they were not as significant as the one conducted in the monolayer KB cells. Because the effects of nanocarrier shape and targeting ligand are interconnected and complex, we suggest that these parameters must be carefully optimized for each nanocarrier to ensure optimal drug delivery.

3.1 Introduction

Nanoparticles (NPs) have been widely used as biodiagnostic and pharmaceutical carriers to enhance the efficacy of different applications. To date, three generations of NPs have been engineered for biomedical applications. The first generation of nanomaterials was modified with non-stealth surface chemistries and used in experiments to assess cell uptake and toxicity.[146, 147] The main focus of these materials was to determine the effects of surface charge.[148, 149] Consequently, second-generation nanomaterials are characterized by two important design concepts: stealth and active targeting. For the first and second generations, although water solubility, biocompatibility and being stealth for the immune system of the body have been met, they still need to address issues such as dynamic properties, theranostic abilities, overreliance on passive targeting and finally limitations on shape, size and charge adjustments. The third generation shifted the paradigm of design to “intelligent” platforms that should improve targeted compound delivery, where based on the final approach, a broad range of carrier properties can be modified.[150]

In regards to cancer treatment or diagnosis, several important properties of NPs are desirable such as high biocompatibility, long in-vivo circulation half-life, high accumulation at cancer tissues and high loading drug/diagnostic capacity. Significant attention has drowned to a variety of nanocarriers, such as liposomes,[151] solid lipid NPs,[152] polymeric micelles,[153] dendrimers, and aptamers[154] indicating great potential for *in vivo* applications. That is due to their great drug carrying capacity, passive accumulation in malignant and inflamed tissues, long circulation times, and adaptability to multiple functions [153, 155].

Recently, it has been proven that both size and shape can also play a crucial role in cellular uptake. The gaps between endothelial cells of the leaky vasculature in the tumor site allow

nanostructures to enter a tumor through a mechanism known as the enhanced permeability and retention (EPR) effect [38, 56]. The efficiency of this process depends on the physicochemical characteristics of the nanoparticles, including both size and shape. It has been established that spherical particles of 20-100 nm in diameter proven to show the optimal range of size for enhancing the accumulation of NPs due to the EPR effect [10, 156]. However, different EPR effects have been reported to non-spherical nanostructures (i.e., nanorods) due to the variations of *in vivo* hydrodynamic behaviors such as circulation, transport in blood flow, and extravasation into the tumor [157, 158].

Further, NPs' shape directly influences uptake into cells. For particles larger than 100 nm, rods show the highest cellular uptake, followed by spheres, cylinders, and cubes in several types of research [159, 160]. In studies with sub-100-nm nanoparticles, spheres show a definite advantage over rods [146, 161] and increasing the aspect ratio of nanorods seems to decrease total cell uptake. However, among various shapes, there are very limited studies on discoidal shape. Therefore, here we focused on creating sub-100-nm NPs with discoidal shape versus the excellent shape based on these studies, which is 50 nm spherical carrier to study in this research.

Another important issue, which is commonly overlooked, is the scalability of the NPs. Recently low-polydispersity, spontaneously-forming lipid-based nanodiscs (~30 nm in diameter and 5 nm in thickness) composed of long- and short- chain lipids [131] are found capable of entrapping hydrophobic molecules and have a robust formation/assembly mechanism [42, 43]. The platform allows large-scale nanomanufacturing of the NPs. A nanodisc-to-nanovesicle structural transition also takes place as the long-chain lipid undergoes from low-temperature gel (order) to high-temperature L_α (liquid disorder) phase. Both nanodiscs and nanovesicles maintain uniform dimensions. At low lipid concentrations, the nanovesicles irreversibly form and would not revert

to nanodiscs even when the long-chain lipid become gel phase as lowering the temperature below the melting point [43-45]. These properties allow us to produce different low-polydispersity morphologies from using identical chemical compositions [43].

However, lack of specificity with passive targeting by nanoparticles is a major drawback with this approach. Therefore, it is of critical importance to develop a more accurate and active system that could target to the tumor, enhance intracellular uptake, and minimize the NPs distribution in healthy tissues. A reasonable approach to achieve these goals is to utilize specific interactions between receptors on the cancer cell surface and targeting conjugated to the nanocarriers [162]. Some ligands, such as folate and transferrin, can substantially increase site-specific targeting [163, 164]. In particular, folate has arisen as an ideal targeting ligand for selective delivery of attached imaging and therapeutic agents to the tumor site. The efficacy of folic acid in these applications has emerged primarily from its simplicity of conjugation to different NPs, the high affinity of binding to folate receptor (FR) (Kd ~ 10^{-9} M) [165], and the extensive distribution of its FR in a different portion of human cancers [166-168].

On the other hand, PEGylation of nanoparticle surfaces increases their blood half-life and create long-circulating “stealth” nanoparticles with improved accumulation in the target tissue, yet these properties also depend on a nanoparticle’s shape, size, and surface chemistry.

Furthermore, it has been shown that nanoparticles with a positive charge can perturb the cell membrane potential, causing Ca^{2+} influx into cells and the inhibition of cell proliferation.[169] While binding of negatively charged nanoparticles to a lipid bilayer causes local gelation, whereas binding of positively charged nanoparticles induces fluidity. On the other hand, blood half-life is highest for neutral and slightly negative nanoparticles.[169, 170] Positively charged nanoparticles are cleared most quickly from the blood and cause several complications such as hemolysis and

platelet aggregation.[159, 169] Therefore, since our platform is capable of being adjusted to have defined surface charge, we have done the synthesis in a way to keep the surface charge slightly negative for all the samples.

In this work, we are investigating the impact of folate addition as a targeting molecule on the enhancement of the cancer cellular uptake of both discoidal and vascular lipid-based self-assembly NPs. The size of both nanostructures was confirmed via dynamic light scattering (DLS). Fluorescence-activated cell sorting (FACS), and fluorescence confocal optical microscopy (FCOM) were used to quantify and visualize the cellular uptake of folate-conjugated NPs, respectively.

3.2 Materials and methods

3.2.1 Materials

Dipalmitoyl phosphatidylcholine (di-16:0, DPPC), dipalmitoyl phosphatidylglycerol (DPPG), dihexanoyl phosphatidylcholine (di-6:0, DHPC), polyethylene glycol (PEG2000)-conjugated distearoyl phosphoethanolamine (DSPE-PEG2000), and folate polyethylene glycol conjugated distearoyl phosphoethanolamine (DSPE-PEG2000 Folate) were purchased from Avanti Polar Lipids (Alabaster, AL, USA) and used without further purification. Nile Red (NR), phosphate buffered saline (PBS) powder were purchased from Sigma-Aldrich (St. Louis, MO). Sepharose CL-6B was purchased from GE Healthcare (Pittsburgh, PA, USA). Cell Titer Blue kit was purchased from Promega (Madison, WI, USA). Folate deficient RPMI Medium (FD-RPMI), Dulbecco's Phosphate-Buffered Saline (DPBS), and Hoechst 33342 were purchased from Life Technologies (Grand Island, NY, USA).

3.2.2 Cells

FR expressing human cervix carcinoma KB cells were continuously grown as monolayers using (FD-RPMI) containing 10% heat-inactivated fetal bovine serum at 37 °C in a 5% CO2 and 95% air humidified atmosphere.

3.2.3 Synthesis of Folate Conjugated Lipid NPs of Different Shapes

(DPPC), (DPPG), (DHPC), (DSPE-PEG2000), (DSPE-PEG2000 Folate), and (NR) were used for NPs preparation. The molar composition of the mixture follows DPPC/DHPC/DPPG/DSPE-PEG2000/DSPE-PEG2000 Folate/NR = 66.58/25.1/3.76/4.5/0.5/0.002. All components of the required weights were first homogenized in chloroform. After the removal of the solvent by a vacuum oven, the dried samples were then re-dispersed in filtered D.I. water to make stock suspensions with a total lipid weight concentration, Clp of 10 wt%. After successive vortex and temperature cycling between 25 and 70°C, the stock dispersions were then progressively diluted at room temperature to Clp = 1.0 mg/ml with phosphate buffered saline (PBS) solution. Vesicles were formed by increasing the temperature of 1.0 mg/ml discs' solution to 55°C for several hours.

3.2.4 Nanoparticles Characterization (Thanks to Armin Rad)

3.2.4.1 Small angle X-ray scattering

Nanostructures were dissolved at a concentration of 10 mg/ml in distilled water. Before SAXS measurements, the supernatants were put in an ultrasonic bath for 30 min and vortexed for 10 minutes. For each experiment, 70 µl of the solution was transferred to Brucker Company standard quartz capillary of 1.5 mm path length, and the background of each sample was measured separately before each experiment. Both scattering and transmittance of each sample were measured separately. Small angle X-ray scattering (SAXS) measurements were conducted at a Bruker NanoSTAR instrument. X-ray was generated by a Turbo (rotating anode) X-ray source

(TXS). A wavelength, λ of 1.542 Å was chosen by Cu-k_α using the Göble mirror. A pair of "scatters" pinholes with diameters of 500 and 350 μm, respectively, was used for collimation. The 2-D intensity data was collected by a MikroGap VÅNTEC-2000 detector with a sample-to-detector distance of 108 cm to cover a scattering vector, q range ($q \equiv \frac{4\pi}{\lambda} sin\frac{\theta}{2}$, where θ is the scattering angle) from 0.007 to 0.25 $Å^{-1}$.

The results will be shown as an absolute scaled intensity as a function of $q = 4л \sin(\theta/2)/\lambda$ where θ is the scattering angle and λ is the X-ray wavelength. Radial averaging and q-conversion of data were performed using the standard software at the beamline. Absolute scaling, i.e. expressing intensities as scattering cross-section per sample volume in units of cm^{-1}, was conducted using BSA as a standard.

3.2.4.2 Dynamic Light Scattering

Size and population distribution of folate and none folate nanodiscs and vesicles were determined by DLS with 633 nm laser beam. All studies were carried out at 15°C for folate conjugate nanodiscs and 25°C for nanovesicles. The samples were dissolved in ultrapure distilled filtered water to 0.1 wt%, aged for five days and vortexed before each measurement. The results were the average of 10 times measurements.

3.2.5 Viability and cytotoxicity assay

Cytotoxicity against KB cells of folate nanoparticles (discs and vesicles) was assessed by Microculture Tetrazolium Assay (MTT) assay and compared with none folate NPs (disc and vesicles). Briefly, KB cells were seeded in 96-well plates at a density around 5000 cells/well. Cells could adhere for 24 h before the assay. Cells were exposed to a series of doses (range from 0 mg/ml as a control to 1.6 mg/ml) of folate or none folate nanoparticles in (FD-RPMI) medium at 37 °C. After incubation with cells for 24 h, 25 μl of MTT indicator dye was added to each well and the

cells were incubated for another four h at 37 °C in the dark. The absorbance was measured at 570 nm using a microplate reader. The value was normalized to the control value (untreated cells) to obtain percentage cell viability.

3.2.6 Evaluation of the effect of folate targeting on the cellular uptake

KB cells were plated in a six-well plate at a density of 50 000 cells/well and allowed to adhere overnight. For analyses of NPs uptake, 20 μL of 1 mg/mL folate nanodiscs, nanovesicles, none folate nanodiscs (control), and none folate nanovesicles (control) were added to each well and incubation was carried out for two h at 37 °C. Following incubation, wells were washed thoroughly with DPBS to remove unbound ligand, after which cells were removed from the plate by trypsin, centrifuged to form a pellet, and resuspended in cold (4 °C) DPBS to block further FR trafficking. Fluorescently labeled NPs in all cell samples were quantitated on a Becton Dickinson FACS Caliber flow cytometer. Ten thousand cells were counted from each sample, and three samples from each treatment condition were evaluated. CellQuest software was used for data collection and analysis.

3.2.7 Confocal microscopy for uptake visualization (Thanks to Armin Rad)

The visualization of the folate NPs internalization to KB cells was done by a Nikon A1R confocal microscope using a 60 x oil immersion lens. Image acquisition was performed by Nikon Elements Ar software. The pre-imaging incubation procedure followed the same conditions for the FACS quantification except that cells were not removed from the well by trypsin. The intensity of the laser beam and the photodetector sensitivity were kept constant to compare the relative fluorescence intensities between experiments.

3.2.8 Mechanism of uptake

FA receptors in KB cells were blocked by adding folic acid to verify that the uptake

mechanism of folate conjugated NPs is following the folate receptor-mediated endocytosis. In brief, 1mM of folic acid was added to each well after plating 50 000cells/well in a six-well plate, and incubated for 30 minutes at 37 °C. Then both folate and none folate NPs (discs and vesicles) were added to each well and incubated for two h at 37 °C. Following incubation, wells were washed twice with DPBS and cells were removed from the plate by trypsin, centrifuged, and resuspended in cold (4 °C) DPBS to block further FR trafficking. The quantification was performed using FACS and confocal microscopy.

3.2.9 Intracellular localization study (Thanks to Dr. Lai and his group)

To follow intracellular trafficking of nanoparticles, 1×10^5 KB cells were seeded on 15 mm glass coverslips and incubated at 37°C for 24 h. Then folate or none folate NPs (discs and vesicles; lipid concentration: 0.1%) were added to cells and incubated for six h. After incubation cells were treated with Lysotracker Green DND-26 (the guideline was provided by Invitrogen) for 30 min, followed by washing three times with HBSS buffer and fixing with 4% paraformaldehyde at room temperature. The coverslips were mounted onto a glass slide. Then, the co-localization of nanoparticles within lysotracker-labeled cellular compartments was examined by confocal laser scanning microscopy (CLSM; Leica-SP5, Leica Microsystems Heidelberg GmbH, Germany). The colocalization ratio of nanoparticles within Lysotracker was quantified by Metamorph software.

3.2.10 Tumor penetration and accumulation of folate lipid NPs *in vivo* (Thanks to Dr. Lai and his group)

Non-invasive *in vivo* imaging system (IVIS) experiment was approved by the Institutional Animal Care and Use Committee of the National Chung-Hsing University. Female athymic nu/nu (nude) mice (ages 6-10 weeks, LASCO) were sterilely inoculated subcutaneously in the right flank with 1×10^7 KB cells. Two hundred microliter of folate or none folate NPs (discs and vesicles; lipid

concentration: 2%) were intravenously injected via tail vein when the tumors reached a volume around 500-1000 mm^3. Images were recorded by the Caliper IVIS system (excitation: 535 nm, emission: 600 nm) at different time points after injection. The fluorescence images were quantified by Living Image software.

3.3 Result and discussion

3.3.1 Nanoparticle Characterization

SAXS can provide an empty core-shell architecture of the designed NPs. This technique is very sensitive to the electron density distribution in the structure of nano-assemblies averaged in time. SAXS data of 1.0 wt.% of folate nanodisc, folate nanovesicle, nanodisc, and nanovesicle and were expressed by the scattering intensity as a function of scattering vector, q (defined as $4\pi\sin(\Theta/2)/\lambda$, Θ and λ being the scattering angle and wavelength, respectively) as shown in (Figure 3.1). Monotonic decays with different slopes were observed in the SAXS patterns. Both nanodisc curves show extra oscillation-like decay at $0.03\ Å^{-1} < q < 0.05\ Å^{-1}$. The main peaks for both were at around $0.12\ Å^{-1}$ which confirms the bicelle structures in them. The overall diameters from SAXS data are the thickness of the bicelle structure while DLS showed the hydrodynamic diameters of the nanodisc nanostructure.

Lipid bilayer can be considered as a lipophilic core (hydrocarbon chains) being sandwiched by two shells (hydrophilic phosphatidylcholine headgroups). Since phosphate group has the highest electron density in the system – greater than those of hydrocarbon tails and water, the electron density profile across the bilayer (i.e., water-headgroup shell-hydrocarbon core-headgroup shell-water) can be approximated by a “square well”. Thus, the SAXS pattern leads to a broad peak corresponding to the correlation length of headgroup-headgroup distance as shown in (Figure 3.1). Moreover, the slope at low q region could also infer possible morphology of the

lipid aggregates.

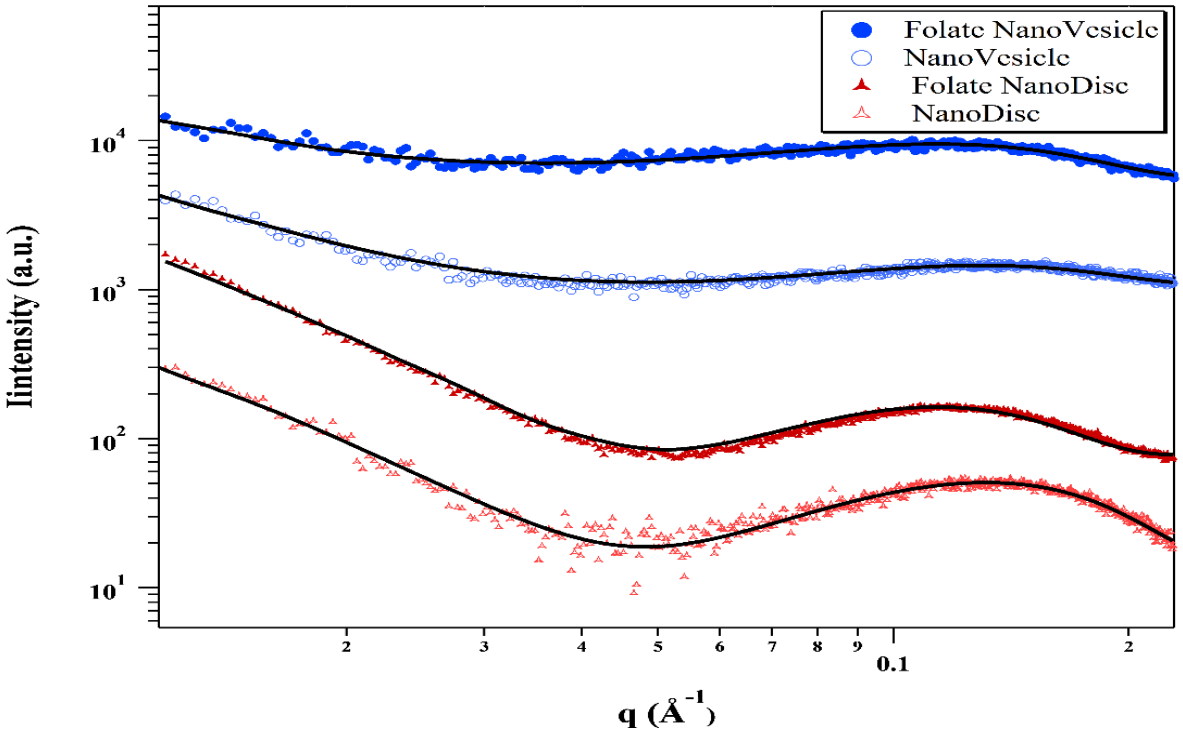

Figure 3-1. SAXS characterization of nanodiscs and nanovesicles.

Moreover, in both nanodisc samples, a transition of slope from q^{-2} to q^{-4} was found indicating that the lipid aggregates were presumably in the planar bilayered structure for both cases. As mentioned above, the high q peaks were observed in both nanodiscs which correspond to the distance between phosphate headgroups. For significant high electron density of headgroup over those of hydrocarbon core and water, the distances between phosphate headgroups can be estimated by the peak position of q_{peak}. That is:

Since

$$\lambda = d * \sin\left(\frac{\theta}{2}\right) \text{ for Bragg condition}$$

$$q_{peak} = 4 * \pi * \sin(\frac{\theta}{2})/\lambda$$

So

$$d = 2 * \pi/q_{peak}$$

At 55°C where vesicles will form, SAXS were also conducted to investigate how folic acid molecules would affect the transformation from nanodisc to vesicles. The slope of the curve for both nanovesicle samples were q^{-2} which could prove that the particles were vesicles composed of the bilayer.

Furthermore, one of the most significant advantages of SAXS is its capability of differentiating the locations of atoms regarding their distinct electron densities, which is reflected by different scattering intensity at various *q* ranges.

To further explain the SAXS pattern, we employ a core-shell discoidal (CSD) model for nanodisc samples, and one-core-three-shell spherical (CSS) model for nanovesicle samples (supporting information) as reported in a recent literature.[8] Each model is described by up to nine independent parameters– the shells thicknesses (which may consist of radial and facial thicknesses, t_{rim} *and* $t_{s,norm}$), the core thickness (t_{core}) and radius (R_{core}), the electron densities of solvent (which here is equal to electron density of water, ρ_w), shell (may consist of rim's, ρ_{rim}, and faces', $\rho_{s,norm}$) and core core (ρ_{core}), as well as polydispersity of the core radius ($p = \frac{\sigma_R}{\langle R_{core} \rangle}$, σ_R and $<R_{core}>$ being the standard deviation and average of R_{core}, respectively).

Using these models and the same values of electron densities as reported in the literature,[150, 171] we can best fit the SAXS data with excellent agreement (Table 3.1). The results of fittings validate the applicability of the models as well as provides us the variations in size and electron density of the nanocarrier after the addition of the folic acid to verify the probable changes regarding the shape, diameter and so on.

	ρ_{rim}, $\times 10^{-6}$ Å^{-2}	t_{rim}, Å	ρ_{core}, $\times 10^{-6}$ Å^{-2}	t_{core}, Å	R_{core}, Å
Nanodisc	9.8	23.5	8.5	26.6	101
Folate Nanodisc	9.8	23.9	8.7	28.9	115
Nanovesicle	-	-	8.4	44.6	232
Folate Nanovesicle	-	-	8.5	47.1	239

Table 3.1. The best-fitting parameters obtained from the SAXS data of the nanocarriers with invariant $t_{s,norm}$ (= 14.9 Å), ρ_w (= 9.40 x 10-6 Å-2) and $\rho_{s,norm}$ (= 1.06 x 10-5 Å-2).

These observations were confirmed by DLS results as shown in (Figure 3.2) which presented the monodispersed lipid nanostructures has two different size ranges, based on the applied temperatures. The samples which have been under heating process, nanovesicle and Folate-nanovesicle, the hydrodynamic radius is ~20 nm. Furthermore, the folic acid conjugated to the surface increased the size slightly which might be due to the laser scattering around the added molecules. On the other hand, the radius sizes of the nanodisc samples are below 10 nm which is in consistency with the SAXS results.

Most importantly, both DLS and SAXS data clearly indicated the absence of nanoparticle aggregation in a solution. The low-*q* SAXS scattering intensity of nanodisc samples increased in comparison with that of nanovesicles as shown in (Figure 3.1) and the contrast was significantly enhanced.

From DLS results it was clear that the size of lipid structures was changed after transformation to vesicles. However, DLS could only provide the average size information for nanodisc samples based on spherical assumption.

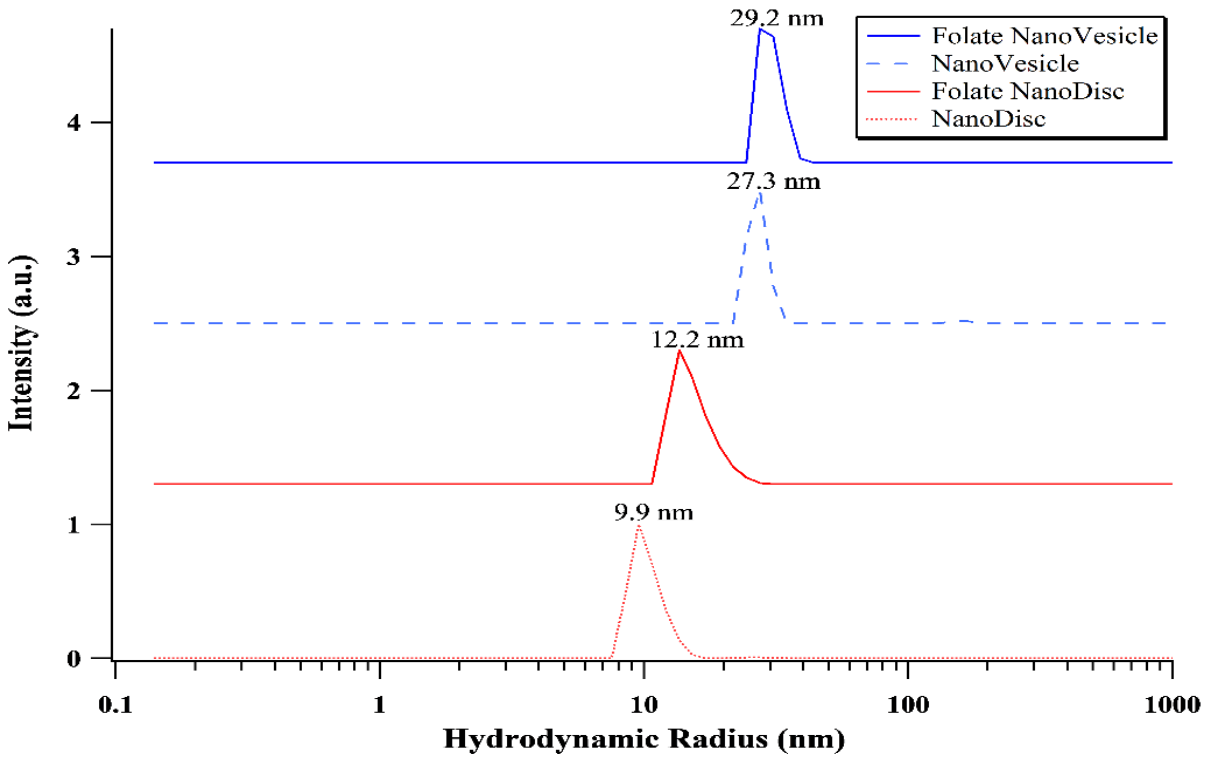

Figure 3-2. Size distribution of folate nanodiscs and nanovesicles. The hydrodynamic radius, R_H of folate conjugated NPs was 10 nm for nanodiscs and 21 nm for nanovesicles.

These results are promising for the application of the nanostructures since it has been shown that our liposomes have diameters between 46.4 to 47.8 nm, which is within 30 to 50 nm range which is the "sweet spot" for nanocarriers.[159, 169] In this size range, not only the nanostructures meet the EPR criteria, but also the ligand density is optimal.[169]

Although in the range of 50-100 nm, EPR effect can be observed, but above 50 nm, nanoparticles bind such many receptors that uptake is limited by the redistribution of receptors on the cell membrane via diffusion to compensate for local depletion. Nanoparticles greater than 50 nm bind

with high affinity to a significant number of receptors and may limit the binding of additional nanoparticles. Mathematical modeling of this phenomenon has demonstrated that optimal endocytosis occurs when there is no ligand shortage on the nanoparticle and no localized receptor shortage on the cell surface.[169, 172] On the other hand, the nanoparticles smaller than 20 nm penetrate deep into the tumor tissue but are not retained beyond 24 h. It also has been shown that even adding a targeting moiety on the surface of these nanoparticles does not appear to increase accumulation inside the tumor or change biodistribution. They are quickly eliminated from the body because they can be excreted by the kidneys.[172, 173]

3.3.2 Viability and cytotoxicity assay

(Figure 3.3) summarizes the outcomes of MTT assay where the cell proliferation counts were obtained after 24 hours of incubation with KB cells. The results were compared to the control cells which were incubated in the buffer in the absence of NPs. No toxicity effect on KB cells up to 1.6 mg/mL (the lipid concentration) was observed in all cases of NPs. The results indicate that all the components making up the NPs are biocompatible.

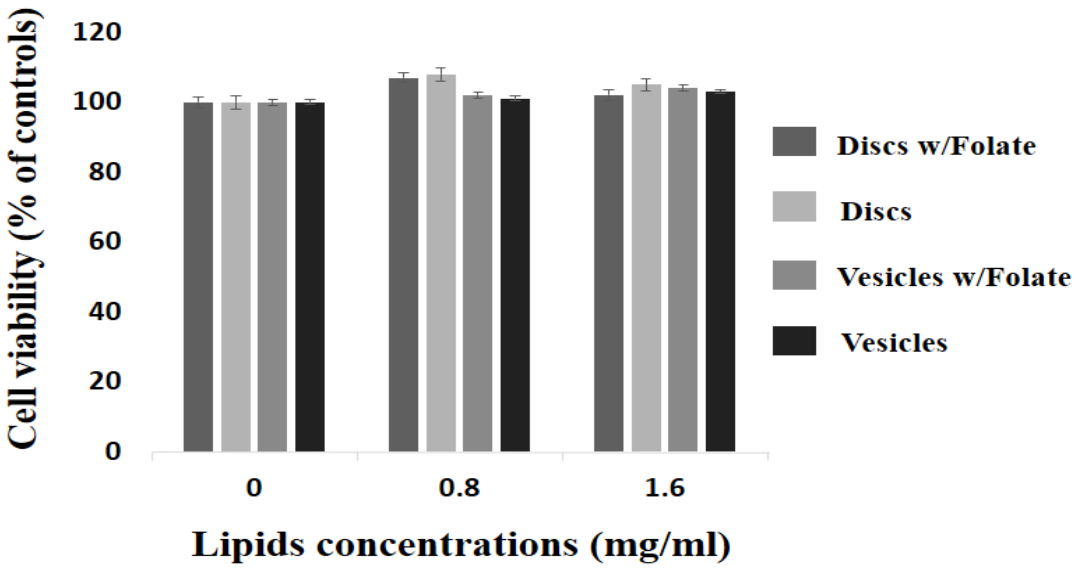

Figure 3-3. The summarized result of MTT viability test on KB cells after being exposed to a solution containing different concentrations of folate or non-folate NPs for 24 hours.

3.3.3 The effect of folate targeting on the cellular uptake

FACS was used to evaluate the cellular uptake of NPs by KB cells. (Figure 3.4) shows the FACS results of four different NPs (bicellar discs, folate discs, vesicles, and folate-vesicles) under the same condition, lipid concentration, and Nile red-to-lipid molar ratio. Each experiment was repeated at least three times. The cellular uptake level of NPs shows a clear dependence of targeting folate FACS data of the cellular uptake of folate and non-folate NPs by the KB cells after 2 hours of incubation at 37˚C.

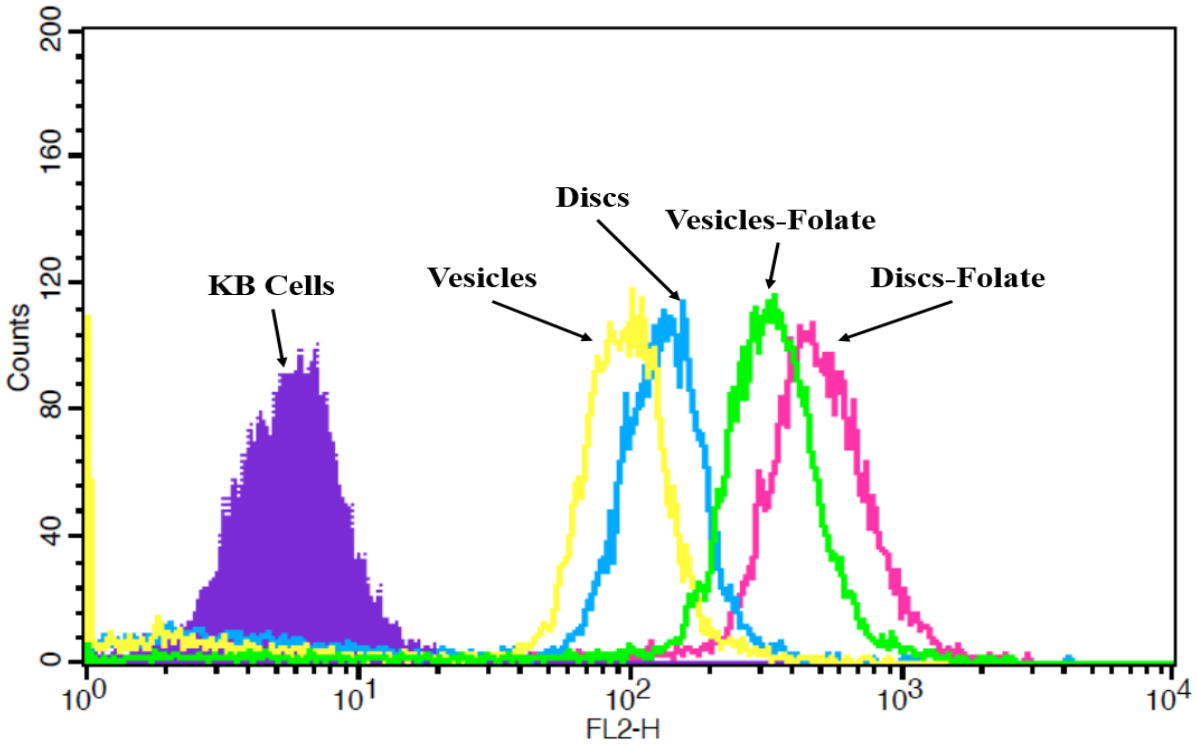

Figure 3-4. FACS data of the cellular uptake of folate and non-folate NPs by the KB cells after 2 hours of incubation at 37˚C. The result shows that the uptake level follows: folate-discs > folate-vesicles > discs > vesicles.

The result shows that the uptake level follows: folate-discs > folate-vesicles > discs > vesicles. and particulate morphology: folate-discs > folate vesicles > discs > vesicles. The uptake of folate discs was higher than that of folate vesicles by ~ 2-3 folds, consistent with our previous report on

the morphological dependent of the cellular uptake of lipid-based self-assembled non-folate NPs (i.e., nanodiscs and nanovesicles). The addition of DSPE-PEG2000 folate on the surface of the NPs further enhanced the KB cellular uptake by ~7 folds. It has been reported that the uptake of monoclonal antibody-coated polystyrene nanoparticles in an experiment on the breast cancer cell line was found the highest in the case of rod-like NPs with a size of 367nm in length and 126 nm in width. Followed by discs in the size of 236nm in diameter and 88 nm in thickness and the lowest for 200 nm spheres.[122] Our FACS results seem to suggest a similar trend even in a much smaller length scale (< 50 nm), further confirming the roles of nano-scaled morphology and targeting molecules in the enhancement of cellular internalization. It is also noteworthy that the targeting effect, in this case, overwhelms the morphological effect since the folate-vesicles show higher efficacy in cellular uptake than non-folate discs do.

Fluorescence confocal microscopy was also conducted under the same sample condition to confirm the FACS results. The optical configuration was identical for all cases. (Figure 3.6 A-D) Show the confocal micrographs of KB cells after being incubated with folate discs, discs, folate vesicles, and vesicles, respectively, for 2 hours and rinsed twice in DPBS. The outcome is consistent with the FACS above result indicating the same sequence in the cellular uptake: folate-discs > folate vesicles > discs > vesicles.

3.3.4 Mechanism of Enhanced Endocytosis by Folate Targeting

To confirm that the enhanced cellular uptake of folate-conjugated NPs originates from the over-expressed folate receptor-mediated endocytosis, we performed a similar FACS experiment under the same condition above except for free folate (at a concentration of 1.0 mM) being added in the cell growth medium.[174]

(Figure 3.5) Shows the FACS results of the cellular uptake of folate lipid NPs by the KB cells. Compared with the outcome obtained from the medium in the absence of free folate, the cellular uptakes were significantly reduced by an order of magnitude, supporting the proposed folate receptor-mediated endocytosis. The higher level of cellular uptake of folate nanodiscs than that of folate vesicles remains valid even in the presence of free folate consistent with our previous report revealing that nanodiscs effectively utilize two more endocytosis (namely, macropinocytosis and microtubule-mediated endocytosis) than the vesicles do, independent of the pathway through folate receptor.[175]

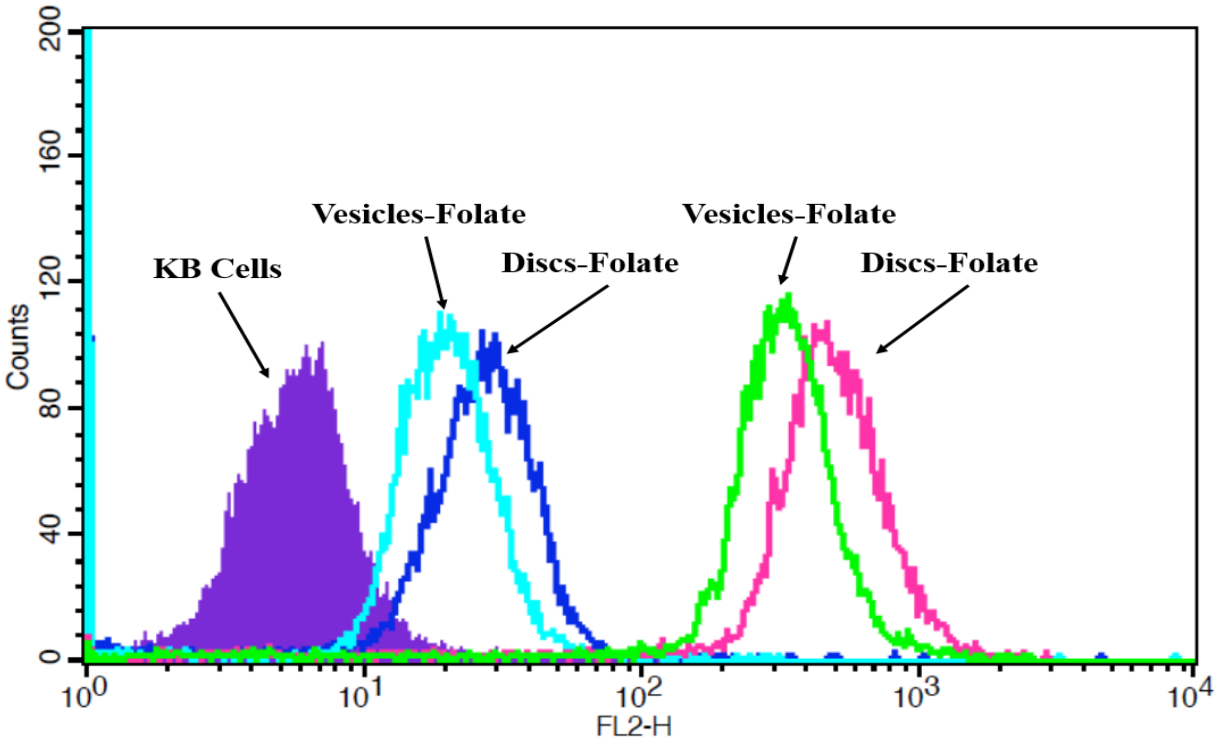

Figure 3-5. FACS analysis of folate mediated endocytosis. The uptake of folate NPs was reduced after the addition of free folate (dark blue) line show the reduction in case of folate discs compared to the (pink) line, and (light blue) represent the reduction in case of folate vesicles compared to the (green) line.

The confocal fluorescence microscopic micrographs (Figure 3.6) where A is compared with E and B is compared with F. The results are consistent with the FACS outcome that the presence of excess free folic acid in the culture media reduces the uptake of folate NPs.

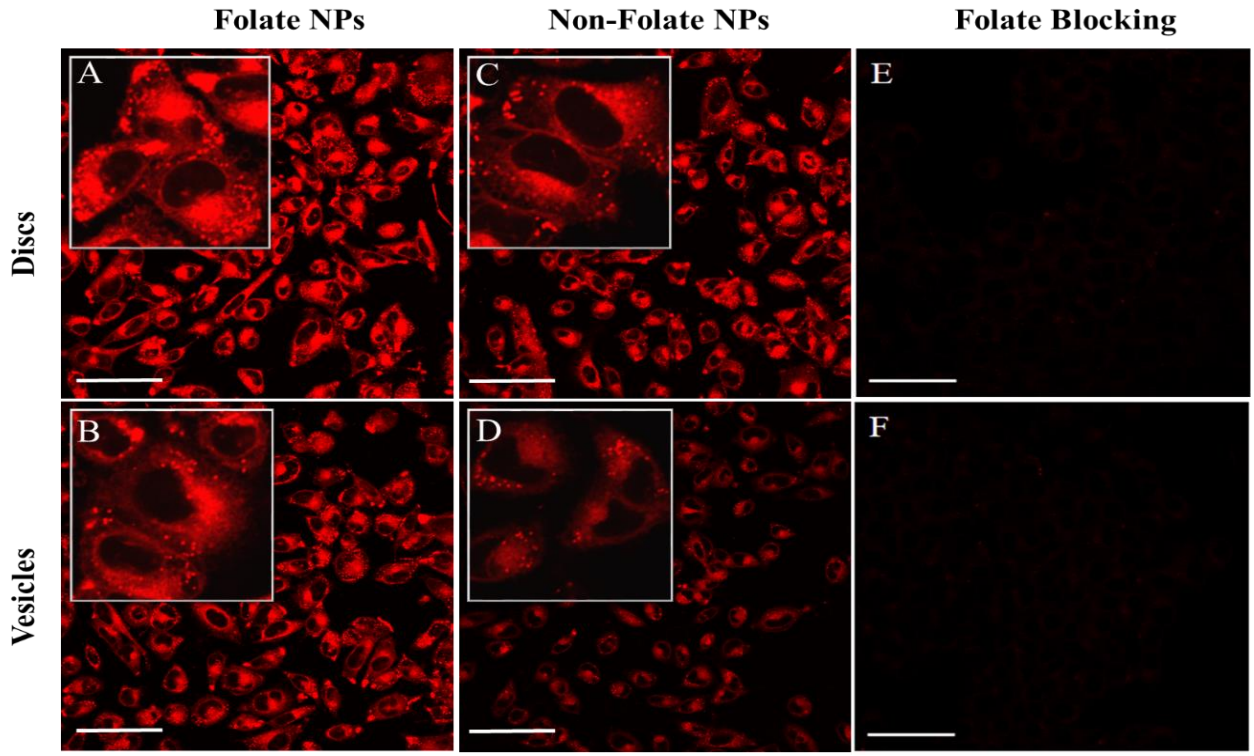

Figure 3-6. Confocal micrographs represent the uptake of folate NPs. (A) folate discs, (B) for folate vesicles, (C) none folate discs, (D) none folate vesicles, (E) and (F) folate discs and folate vesicles after the addition of free folate into culture media. Scale bar is 50 μm.

3.3.5 Intracellular localization study

The intracellular trafficking of NPs was investigated by labeling with Lysotracker Green DND-26 (green). (Figure 3.7) Showed that a lot of none folate NPs (nanodiscs and vesicles) were colocalized in lysosomes (nanodiscs: 98.69%; vesicles: 92.42%). It was indicated that none-folate NPs entered lysosomes and trapped there at six hr. A study by Mansoori and co-workers demonstrated that folate conjugated NPs attached to the folate receptors, followed by uptake through a caveolin endocytotic pathway. The drug was released when the pH value of endosome

approaches five.[176] Another study by Cuong et al. showed that the uptake of the folate-decorated star-shaped PEG–PCL micelle in MCF-7 was via caveolae/lipid raft-mediated endocytosis and then folate receptor-mediated endocytosis.[177] In our research, we also observed that the strong fluorescence of folate NPs was almost expressed in the cytoplasm. The observation of fluorescence in cytoplasm indicated that the folate NPs were internalized by the cells through endocytosis and folate NPs were distributed in the cytoplasm after escaping from the endosome and/or the lysosome (nanodiscs: 7.91%; vesicles: 29.81%).

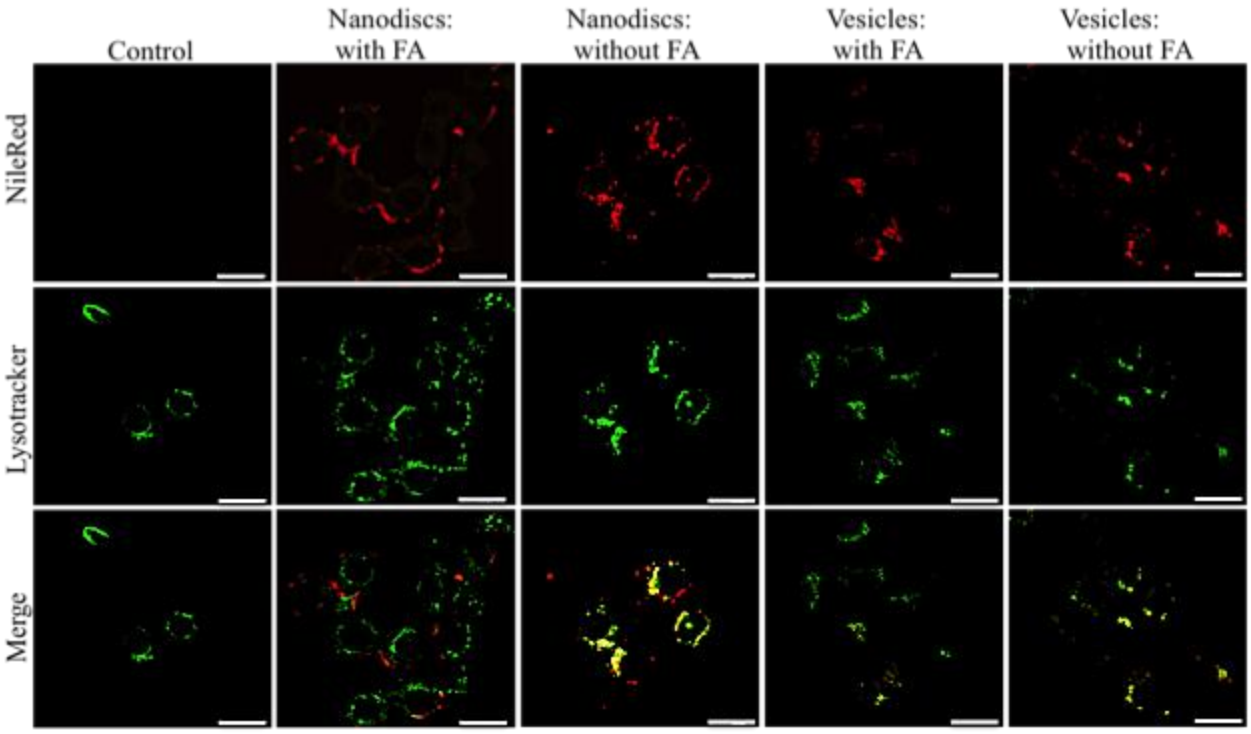

Figure 3-7. Fluorescent images were utilized to assess the colocalization of nanodiscs-Nile red with or without FA and vesicles-Nile red with or without FA (Red) with lysosomes using Lysotracker (green). The colocalization ratio of nanoparticles within Lysotracker was quantified by Metamorph software. Scale bar: 10 μm.

3.3.6 Tumor penetration and accumulation of folate lipid NPs *in vivo*

The tumor targeting efficiency of the folate and none folate NPs were evaluated *in vivo* using KB tumor-bearing mice by the Caliper IVIS system. Folate disc NPs exhibited a higher tumor uptake in comparison with folate vesicle NPs at different time points. The same situation also observed in none folate disc NPs and none folate vesicle NPs. The penetration rate and accumulation volume of NPs were folate disc > folate vesicle > none folate disc > none folate vesicle (Figure 3.8., Table 3.2 and Table 3.3).

Since the molarity percentage of the charged lipids, DSPE-PEG2000 and DHPC, is fixed within the different samples, surface charge cannot be a major parameter to cause these various biological responses. Nonetheless, it is worth to mention that since neutral and slightly negatively charged nanoparticles have longer circulation lifetimes and less accumulation in the liver, spleen, kidneys and lungs, we have chosen the lipids above to provide a marginally negative charge.[159, 178]

Additionally, it is well-known that cylindrical and discoidal shapes exhibit unique flow characteristics that substantially alter circulating lifetimes, pharmacokinetics, biodistribution, cell membrane interactions and macrophage uptake, which in turn affect biodistribution among the different organs.[159, 178]

These results confirm that the nanodisc samples are even more efficient than the spherical NPs which were within the optimum range of size and surface charge. Keeping the size of all the samples within 30-50 nm range improved their EPR effect as well as having maximum surface ligand density for the interaction with the cells.[169, 170] Within the previous size range, the excellent shape was introduced to be a spherical shape in previous studies. Spherical nanoparticles showed significant better cellular uptake in comparison with other shapes with higher aspect ratios,

such as rods.[146, 161] Interestingly, recent mathematical modeling combined with *in vitro* and ex-vivo experimentation demonstrated that discoidal geometries possessed the most favorable margination dynamics in the body.[173] However, to the best of our knowledge, discoidal shape was not studied in a fair comparison with another shape in an optimization study like this. Hence, current results can clearly show this shape, at least for this charge and carrier chemistry, is significantly more successful than spherical carriers and potentially can be a promising alternative shape for the next generation nanocarriers.

Likewise, NPs' geometries affect hemorheological dynamics, cellular uptake and *in vivo* fate. It has been shown that discoidal nanoparticles display unique movement dynamics that favor the interaction with vessel wall more than spherical particles.[159, 179] Therefore, the observed differences between biological responses to our various samples can be originated from several causes.

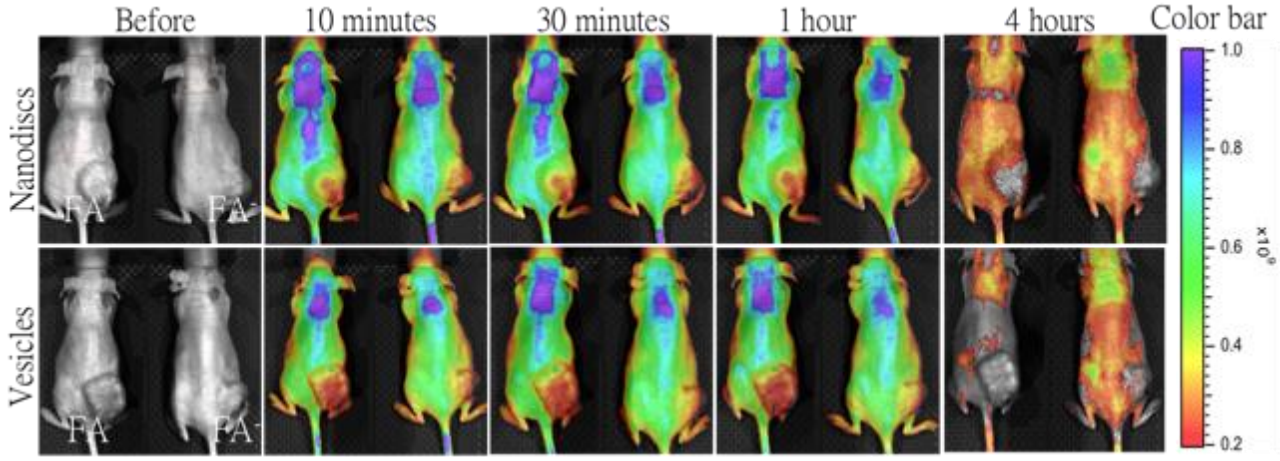

Figure 3-8. *In vivo* fluorescence images of mice bearing KB tumor. The mice were intravenously administered with folate or none folate NPs (discs and vesicles) at 2% lipid, and the fluorescence signal was monitored at different time points post-probe administration.

Nanodiscs:	0min	10min	30min	1hr	4hr
FA	5.3041E+10	3.3243E+11	3.1265E+11	2.4921E+11	9.9726E+10
FA-	1.3151E+10	6.418E+10	6.1226E+10	4.9961E+10	2.6124E+10
Vesicle:					
FA	3.9885E+10	2.1973E+11	2.0676E+11	1.4999E+11	5.7415E+10
FA-	2.5601E+10	1.0201E+11	9.1472E+10	6.6584E+10	3.9853E+10

Table 3.2. Region of interesting in tumor was quantified by Living Image software

Nanodiscs:	0min	10min	30min	1hr	4hr
FA	1	6.27	5.89	4.70	1.88
FA^-	1	4.88	4.66	3.80	1.99
Vesicle:					
FA	1	5.51	5.18	3.76	1.44
FA^-	1	3.98	3.57	2.60	1.56

Table 3.3. Fold increasing of (ROI) in the tumor.

3.4 Conclusion

Both *in vitro* and *in vivo* results indicate the impacts of morphology and ligand-targeted nanoparticle accumulation in cancer cells. The toxicity of the folate and none folate NPs are minimal to KB cells. Overall speaking, folate targeting provides an important mechanism for high cellular internalization for KB cancer cells. Moreover, our experimental outcome also indicates that the NPs with vesicular shape is less efficient in cellular uptake compared with those of discoidal shape. However, the shape effect is *not* as significant as the folate targeting in the cell study compared to the animal study. The penetration rate and accumulation volume of NPs were folate disc > folate vesicle > none folate disc > none folate vesicle.

These findings, besides other research regarding low-polydisperse well-defined nanocarriers [159, 169, 178] can alter the EPR paradigm, which has been limited to define the effect of particle size in cancer diagnostics and therapeutics, in favor for the more general targeting approaches. Accordingly, development of platforms and nanocarriers fabrication processes which can create non-spherical shapes may hopefully provide a path to a revolutionary feasible design solutions.

Chapter 4. Tumor on Chip: A Potential Strategy to Examine the Impact of the Design of Lipid Nanoparticles on their Transportation into 3D Ovarian Tumor.

Abstract

A key factor in cancer treatment and drug therapy is the development of carriers that can proficiently reach targeted cells. Results obtained from nanomedicine studies are mostly based on 2D cultures which cannot be interpreted to *in vivo*. In this work, we developed a 3D culture microfluidic chamber made of a polydimethylsiloxane (PDMS) for studying nanoparticle penetration and transport in ovarian cancer cell–gel cultures. A mixture of cells embedded in a 4-arm Poly (ethylene glycol) acrylate (4-arm PEG Acrylate) hydrogel is loaded in the chamber. The microfluidic device offers straightforward and rapid fabrication, direct *in vitro* cell imaging, and an easily configurable and controllable microenvironment for different cell culture. To assess the application of the device, we studied the transportation of two distinct shapes of fluorescently labeled lipid self-assembly nanoparticles, in addition to studying the effect of targeting molecules in increasing the penetration of nanoparticles to the 3D cancer cells embedded in the microchannel under constant flow conditions. Penetration of nanoparticles was enhanced by targeting to folic acid receptors and revealed particle shape restrictions to efficient delivery. This device was designed for delivery studies. However, it can be easily modified to be useful for any other biomedical applications.

4.1 Introduction

Nanotechnology has emerged as an important tool to be applied in cancer-targeting therapeutic and diagnostic. Nanoparticles (NPs) made of a variety of materials in different sizes and shapes are the point of interest in many types of research. However, delivery of these nanoparticles remains unpredictable because of poor control over the accumulation of carrier systems in tumor tissues *in vivo*.[4] To overcome this problem, a better understanding of how nanoparticles (on their size, morphology, and surface modification) enter to the target tumor and distribute at the cellular level is required.

So far, *in vivo* animal models have been useful for assessing general pharmacokinetics.[80-82] Also, they have been used to study the effect of different criteria in particles manufacturing such as size, shape, surface modifications and the material in use. However, it has been difficult to evaluate the tumor tissue without interruption of lymphatic and blood clearance.[180] Also, it is hard to visualize target tissues at the cellular level during animal studies because of the low resolution of whole-animal imaging techniques.[83] As a result, our knowledge of the interaction between the nano-carriers and the cell is gained from in vitro cell monolayer experiments.[18] Information gained from these studies is mostly limited to characterization of the binding affinity, uptake, cellular responses and toxicity of the nanoparticles.[46, 54, 74, 75] However, the absence of a three-diminution (3D) tissue structure make these findings inaccurate to predict the *in vivo* results.

A massive number of evidence suggests that the 3D models replicate more accurately the actual microenvironment of the tumor compared to the two-dimensional (2D) monolayer cell cultures; therefore, the behavior of cells cultured in 3D will reflect more closely the *in vivo* responses.[76-79] Thus, different approaches of in vitro 3D culture models for cancer research

have been invented. These methods include but not limited to the multicellular spheroids grown in suspension,[86, 114, 181] cells embedded within either naturally derived extracellular matrices (ECM) [182-185] or collagen gels.[113, 186]

A recent approach which offers a highly customizable micro-scale platform to assess complex cellular structures has been the focus of researchers. Microfluidic devices are an excellent tool to investigate tumor tissue in a relatively natural microenvironment. Microfluidic devices can be adapted for different biomedical applications such as cells culture, mimicking the cellular microenvironments, and ex vivo tissue evaluation.[11, 93, 187-190] All of these can be done using microliter amounts of reagents under controllable flow conditions.[118, 191, 192]

Based on several *in vivo* and *ex vivo* studies, it is well recognized that NP size, shape, and surface chemistry can affect tumor accumulation.[18, 46] Several 3D in vitro studies have been done to evaluate chemotherapeutic drug diffusion;[109-112] however, the role of drug carriers design in tumor accumulation is not well addressed. These studies announced the potential role of microfluidics as an approach for the rapid and cost-effective pre-screening of nano-carriers while also providing sufficient data to model the transport process before full animal studies.[118]

As previously mentioned, only a few studies have been done using microfluidic devices to evaluate the relationship between nanoparticles physiochemical properties and their penetration into the tumor. The focus of these research was on the effect of the nanoparticle size on their abilities to overcome the physical factors and barriers that influence their distribution in the tumor. [115, 116] The results of these studies suggest that the usage of the microfluidic systems assist the evaluation of different NPs in different tumor systems before animal studies.

Here, we present the design, fabrication, and evaluation of hydrogel cell culture microfluidic device that can be used to study nanoparticle penetration and delivery to cancer cells in a 3D matrix

under interstitial fluid flow. The device met all essential design criteria for this application, including the viable cell culture in a 3D matrix, the imposition of fluid flow through the 3D cell culture, and the live cell imaging during perfusion. Moreover, we could proof the feasibility of using this device to investigate the effect of shape (discoidal and vesicular) with the addition of folic acid (FA) targeting on the penetration of nanoparticle through the hydrogel to 3D ovarian cancer cells.

4.2 Materials & Methods

4.2.1 Materials

Microfluidic devices were gently provided by Prof. Pinar Zorlutuna's group, 4-arm PEG Acrylate, Mw 20000, was purchased from JenKem Technology, Allen, TX, USA. The photoinitiator, 1-[4-(2-hydroxyethoxy)-phenyl]-2-hydroxy-2-methyl-1-propane-1-one (Irgacure 2959) was purchased from Ciba, Tarrytown, NY, USA. RPMI-1640 media and phenol-free RPMI-1640 media were purchased from Life Technologies, Grand Island, NY, USA.

4.2.2 Cell culture

OVCAR-8 a human ovarian cancer cells (gently provided by Prof. Xiuling Lu, Department of Pharmaceutical Sciences, University of Connecticut) were cultured in a monolayer in RPMI-1640 media supplemented with 10% FBS and 1% penicillin at 37˚C in 5%CO_2 and 95% humidified air. Cells grown to pre-confluency were passaged no more than ten times using 0.25% trypsin and 0.04% EDTA. Before encapsulation in hydrogels, cells were added to the pre-polymer solution and mixed gently.

4.2.3 Fabrication of Microfluidic Devices

The design and fabrication of the device were performed by our cooperator Dr. Pinar Zorlutuna's group. Devices were fabricated using elastomer polydimethylsiloxane (PDMS) as

follow: (a) Rapid Prototyping which included the designing of three microfluidic channels (outer channels widths = 1100 µm, the middle channel is 2200 µm) in a Computer-aided design (CAD) program: The design transparencies as seen in (Figure 4.1 A) were printed by a commercial printer from the CAD files with the design clear and the background ink. Transparencies were used as masks in photolithography on negative photoresist (SU-8) spin-coated onto silicon wafers to create masters. (b) Molding: a 10:1 mixture of PDMS prepolymer and curing agent (Sylgard 184) were stirred thoroughly and then degassed under vacuum. The prepolymer mixture was then poured onto the master and cured for one h at 65 °C. After curing, the PDMS replica was peeled from the master. (c) Sealing. A PDMS replica and a cover slip will be rinsed in ethanol. The cured mold was irreversibly bonded to the coverslip by oxygen plasma treatment and tubing of 1/16 inches. Inner diameter was used to connect to syringes pump for cell loading and media injection. (Figure 4.1 B) represents the fabrication process.

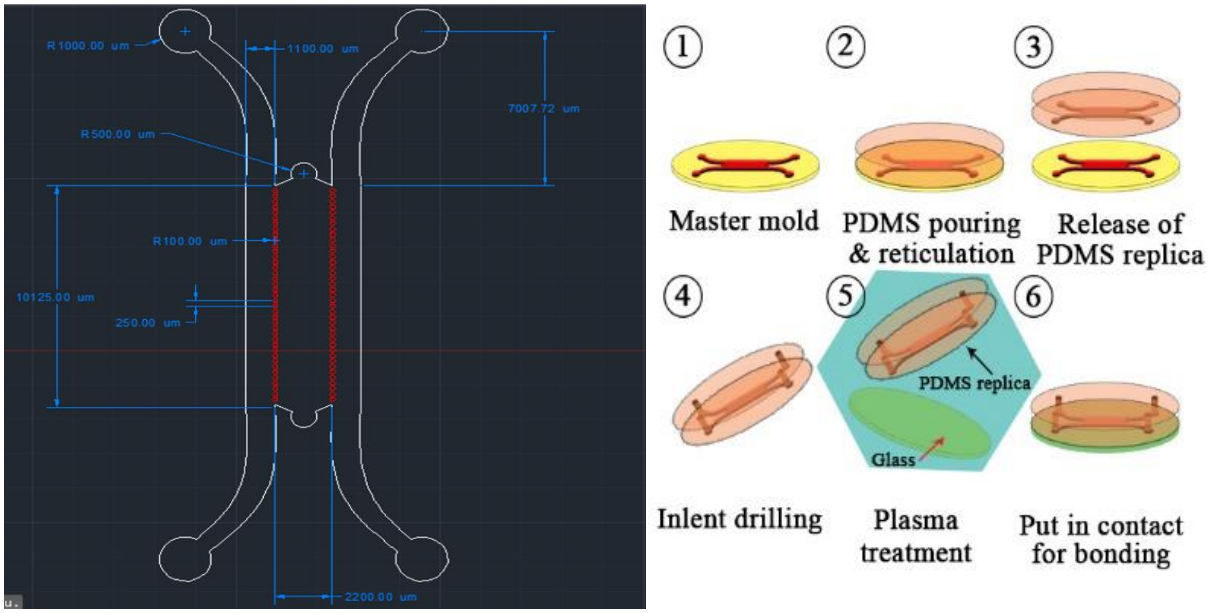

Figure 4-1. The design and fabrication of the microfluidic device. (A) The CAD design of the microchannel. (B) The fabrication process using photolithography.

4.2.4 Hydrogel Preparation and Cell Encapsulation Process

20 mg of 4-arm PEG Acrylate 20K (PEG 20K) was mixed with 100 µl of phenol-free RPMI-1640 media. Also, a 1% photoinitiator (PI) (Irgacure 2959) was prepared by mixing 10 mg PI with 100 µl ethanol and 900 µl PBS. Encapsulation was done using an equal volume of OVCAR-8 cells suspension and pre-polymer solution to give a final concentration of 10 % PEG20K, 0.1 % photoinitiator (wt/v, Igracure 2959), and 50 million cells/mL in phenol-free RPMI-1640. Cells and prepolymer were mixed, and the microfluidic chambers were filled with the mixture then cross-linked via UV irradiation for 30 seconds at 6.9 mW/cm^2. After encapsulation, hydrogels were washed several times with media to remove the uncrossed gel and PI. Then the cells within the microfluidic device were incubated under 5 % CO_2 at 37°C. Media was supplemented using a syringe pump under a constant flow rate. The cell aggregations and tumor formation within the hydrogel were evaluated and measured using Zeiss Axiovert 40 CFL inverted microscope.

4.2.5 Cell Viability within Hydrogel

Two methods were used to assess long-term cell viability in the cross-linked hydrogel and the microchannel. In the first study, OVCAR-8 cancer cells at a density of 10 million cells/mL were encapsulated in 10% PEG20K hydrogels patterned in single-layer disks with dimensions of 160 µm thickness and 2 mm diameter. These disks were cultured in media at 37˚C over a period of 14 days. Cell viability was quantitatively evaluated using MTS assays. The absorbance density measurements obtained from these assays on 1, 4, 7, and 14 days were converted to relative cell viability (%) by normalizing to 0 days. In the second study, the viability of encapsulated OVCAR-8 cells in the microfluidic device was tested at three time points (day 4, 7 and 14) by staining them using the live/dead assay. 2x PBS was pumped into the channels to wash out the growing media from encapsulated cells. Then the live/dead staining solution was pumped for 5 min at 37ºC. To remove unbound reagents, cells were washed again with PBS. Nikon A1R fluorescence confocal

microscope was used to observe encapsulated cells. This assay identifies esterase activity in live cells via green fluorescence emission from calcein AM and nuclear permeability in dead cells via red fluorescence emission from propidium iodide.

4.2.6 Effect of NPs Morphology and Targeting on Tumor Accumulation

Fluorescently labeled lipid nanoparticles namely (discs, vesicles, discs w/FA, and vesicles w/FA) were diluted individually in phenol-free RPMI-1640 media to a final concentration of 1 mg/mL. Then they were pumped through the chambers by the syringe pump under a constant flow condition for 12 hours, and images were taken using a confocal microscope. A comparison of the fluorescent intensity was performed to observe the effect of NPs shape or targeting on the accumulation in the tumor.

4.2.7 Confocal Microscope Conditions for the Microfluidic Device

The microfluidic device was mounted on a microscope stage inside a 37˚C incubator. Media containing NPs was pumped at a flow rate of 12.96 μL/min which is relevant to blood flow in tissue capillaries, [193, 194] and was controlled using a syringe pump. NPs accumulation images were taken using a 40X emersion objectives on a Nikon A1R confocal microscope. Images were taken in the center layer of the 3D tumor every 10 min for 12 hours.

4.2.8 Calculating the Rate of NP Accumulation

Fluorescence distribution was analyzed in ImageJ by drawing a contour around the cell aggregates freehand and measure the mean fluorescence at the various time point. Results were collected after 1 hour and after 12 hours. Accumulation of NPs in the tumor tissue was obtained by taking the mean fluorescence in selected images and normalizing to fluorescence of the surrounding media. The final accumulation data was obtained after subtracting the background.

4.3 Results and discussion

4.3.1 Characteristic of the Microfluidic device

The device consisted of the main chamber area, two media reservoirs as shown in (Figure 4.2). The main chamber area, which measures about 10125 µm (length) × 2200 µm (width) × 160 µm (height) was used for tissue culture. As highlighted in (Figure 4.2), the photo-cross-linked gel encapsulating cells was located between the two red lines. The PDMS posts in 100 µm radius guide and retain the viscous cell–gel solution during loading, thus giving the cell–gel a definable geometry after photocrosslinking, and serve as lateral but porous supports for the cellular gel. The device was also designed for direct *in vitro* cell observation in 3D structure under controllable flow. Thus, the chamber has to be optically transparent under low or high magnification. Using the device for i*n vitro* observations with the media compartments at the sides improved the optical imaging to monitor the transportation of the NPs.

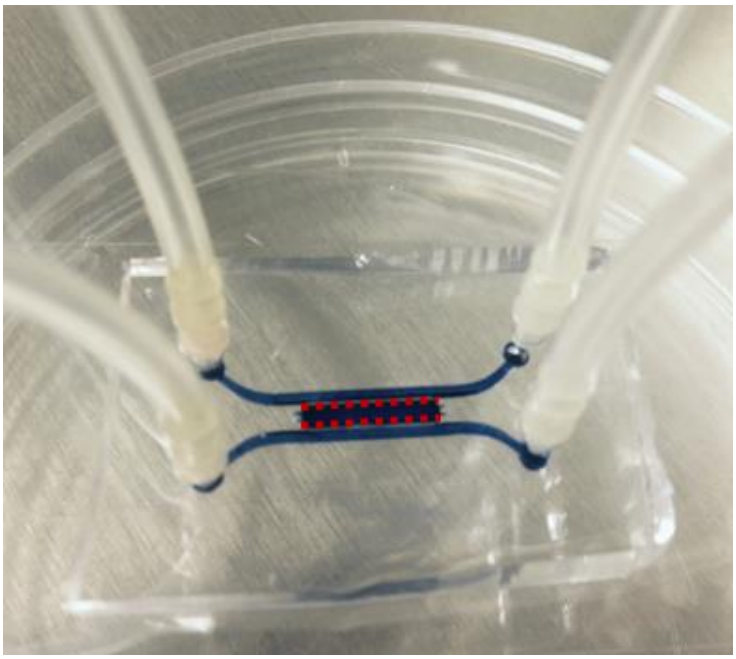

Figure 4-2. A picture of the microfluidic device show the microchannel in blue. The central channel for cell encapsulation is between the two red lines. Two inlet tubes and two outlet tubes for media supplement and waste removal, respectively.

4.3.2 Evaluation of cell aggregation in the hydrogel

To evaluate the growth of OVCAR-8 cells in PEG 20K hydrogel inside the microfluidic devices, several micro images were taken via Zeiss Axiovert 40 CFL inverted microscope at several time points starting at the day of encapsulation up to 14 days. Images were analyzed in ImageJ to measure the size of aggregates and tumor formation by measuring the diameter of each aggregate. The result in (Figure 4.3) indicates that OVCAR-8 cells start to form small aggregates after 48 hours of encapsulation and continue to grow to reach 270 µm in the largest diameter of the aggregate at day 7. Since the attempt to mimic the ECM of ovarian cancer is very critical, we chose to use PEG 20K as the matrix for cell encapsulation. This type of hydrogel was used in several studies for tissue engineering and stem cells proliferation,[195, 196] where the results suggested that the microenvironment created by PEG 20K modulate the fate of cell differentiation and aggregation.[197] Therefore, we were expecting to observe the same phenomena, where OVCAR-8 cancer cells proliferate and aggregate in a similar microenvironment.

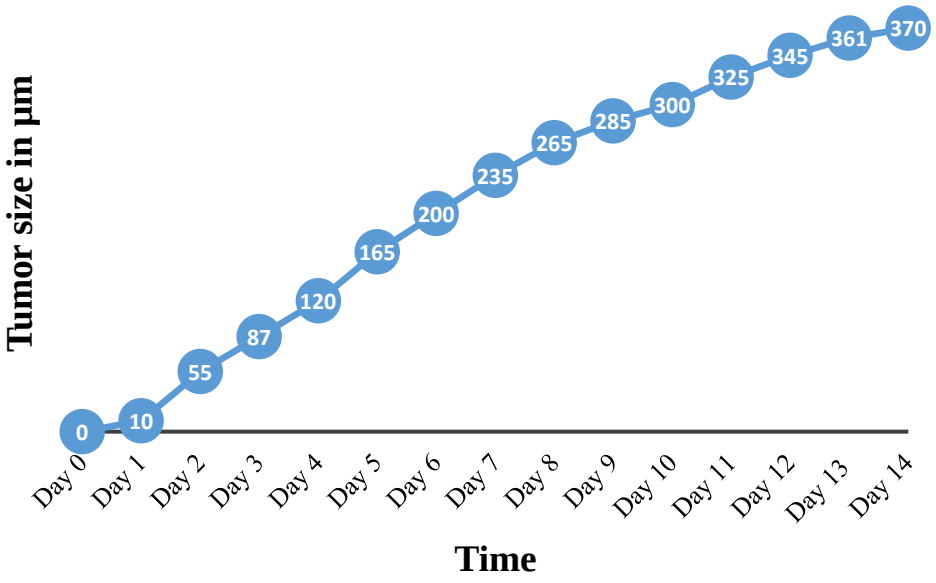

Figure 4-3 Size measurements of OVCAR-8 cell aggregates in PEG 20K microfluidic over time.

4.3.3 Cell viability

Studying the long-term survival of OVCAR-8 ovarian cancer cells encapsulated in the 3D hydrogel matrix required the use of two different approaches to examine cell viability. The MTS assay results in (Figure 4.4) indicated that the cell numbers were increased after 24 hours, which was maintained for seven days. However, a decrease in cell numbers by 36% was observed by the end of 14 days. Qualitative LIVE/DEAD, cell viability stain, was also performed. Representative images (Figure 4.5) showed an increase in the dead cells over later time points, which supported the results of the quantitative MTS assay.

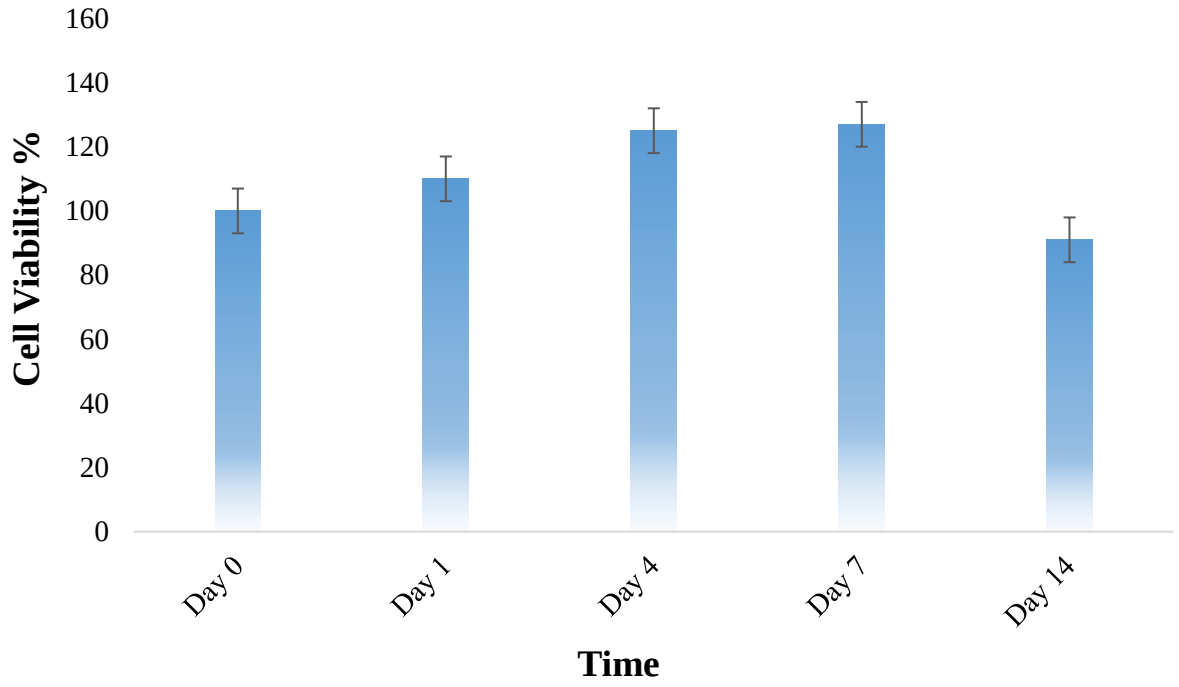

Figure 4-4. OVCAR-8 cell viability over 14 days in PEG 20K hydrogels. The absorbance at (490 nm) values quantified by MTS assays were normalized to 0 day. All values are mean ± standard deviation of n = 3.

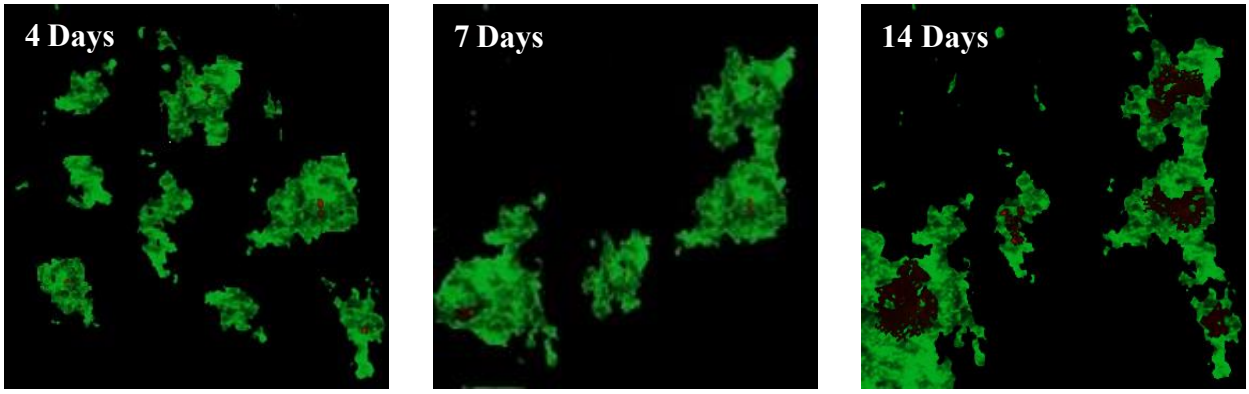

Figure 4-5 Live and dead cells were indicated by calcein-AM (green) and propidium iodide (red), respectively.

4.3.4 Nanoparticle penetration based on morphology and targeting effects

The main application of our tumor on a chip in this study is to address several concerns about the transportation and accumulation of NPs in the tumor tissue. Since it has been difficult to address the delivery of NPs using either animal models or cell culture experiment, this approach should be very useful for real-time imaging and better understanding. In the first set of experiments, we examined the effect of NP shape on their accumulation in the tumor tissue. Fluorescently labeled lipid-based nanodiscs and nanovesicles were administered individually to the OVCAR-8 3D tumor in the microfluidic chip for 12 hours at a flow rate of 12.96 µL/min. The penetration of NPs was quantified based on the fluorescence intensity of the NPs in the tumor using ImageJ, and the results are also presented in (Figure 4.6 A). Also, the accumulation of either nanodiscs or nanovesicles into the tumor tissue after 1 of continues flow were captured with confocal microscopy as shown in (Figure 4.6 B). The nanodiscs started to be visible inside the tumor within the first 10 min and continued to increase relatively with time. In contrast, the nanovesicles showed significantly less accumulation within the tumor tissue, and they started to appear in very low visibility after 60 min. It has been hypothesized that the accumulation of

filomicelles NPs in the tumor tissue is controlled by EPR effect, and due to the morphology of these NPs, they can move around obstacles into tumors through small leaky vasculatures.[198] If we based our results on that, then the highest accumulation of nanodiscs compared to nanovesicles is due to their morphology which allows them to penetrate through the ECM faster than that of the vesicular NPs.

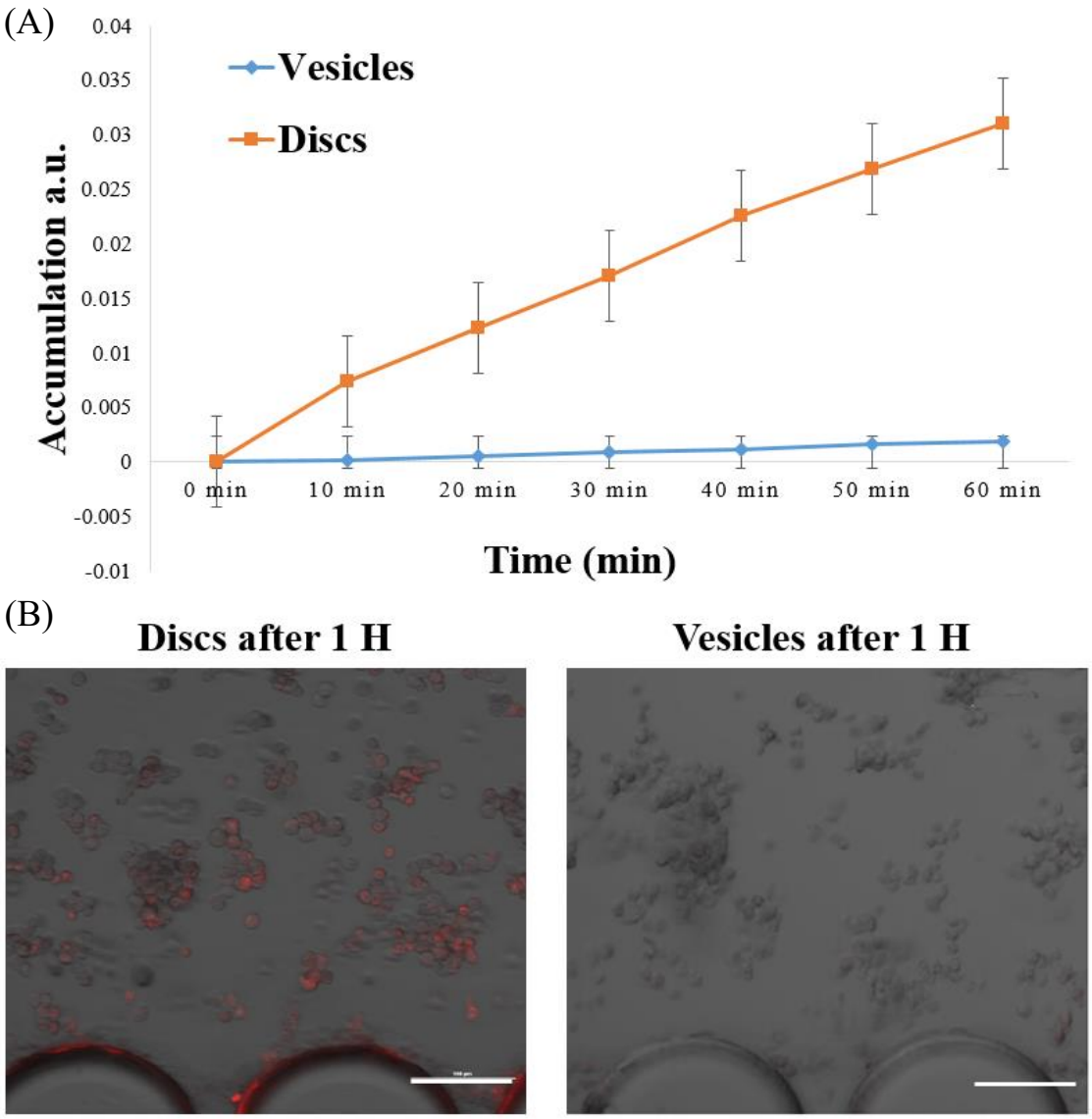

Figure 4-6 Effect of NPs shape on tumor accumulation. (A) The quantification of fluorescently labeled discs and vesicles penetration into the tumor tissue during the first hour, (B) micrographs were taken at the end of 1 hour. Scale bar is 100 µm.

Next, we used the tumor on a chip to verify the effect of PEG-folate to target folic acid receptors on the tumor cells. A comparison of the penetration of disc w/FA and vesicles w/FA was conducted on OVCAR-8 tumor aggregates in the microchannel. Diluted NPs were pumped to the microchannel at 12.96 μL/min, and pictures were taken every 10 min for 12 hours. Results indicated that the average fluorescence of targeted NPs accumulation in the tumor by the end of the first hour was significantly increased with respect to time (Figure 4.7).

The results were also compared with none targeted discs and vesicles. By the end of the experiment, the accumulation of discs' w/FA was improved by about 39% compared with none targeted discs. Moreover, the accumulation of vesicles w/FA increased by 42% compared to the results of vesicles because of the effect of the active targeting. However, the accumulation of the discoidal NPs still dominant either with or without targeting. Discs w/FA proved to have the maximum tumor accumulation of 79% more than that of vesicles w/FA as seen in (Figure 4.8). Therefore, we demonstrated from these findings that folate active-targeting NPs could increase accumulation compared with diffusion alone. Also, in all settings we verified the importance of NPs shape in the enhancement of penetration and delivery to tumor tissue. This must be useful before conducting any *in vivo* tests.

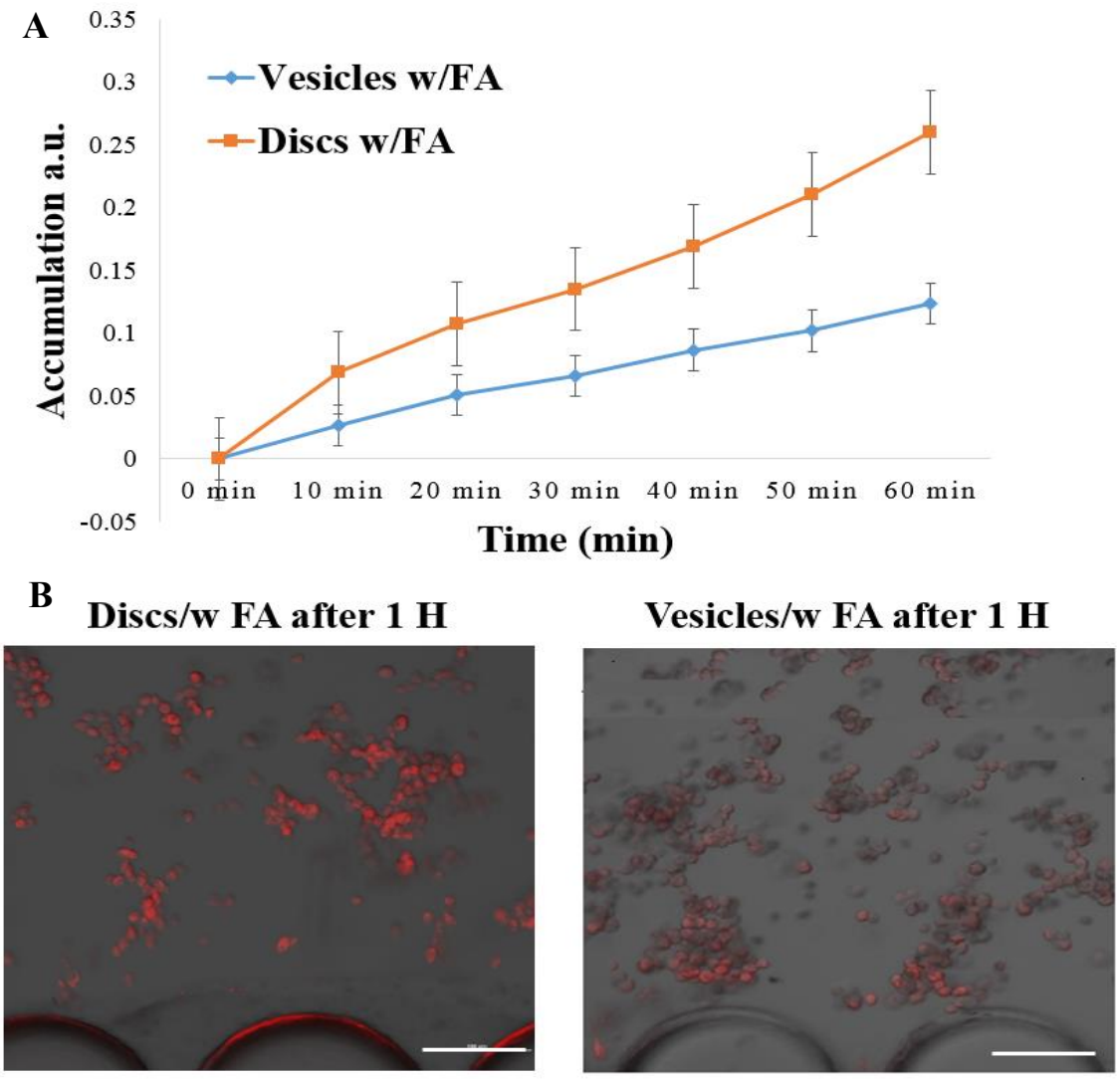

Figure 4-7 Effect of NPs targeting on tumor accumulation. (A) The quantification of fluorescently labeled discs and vesicles penetration into the tumor tissue during the first hour, (B) micrographs were taken at the end of 1 hour. Scale bar is 100 µm.

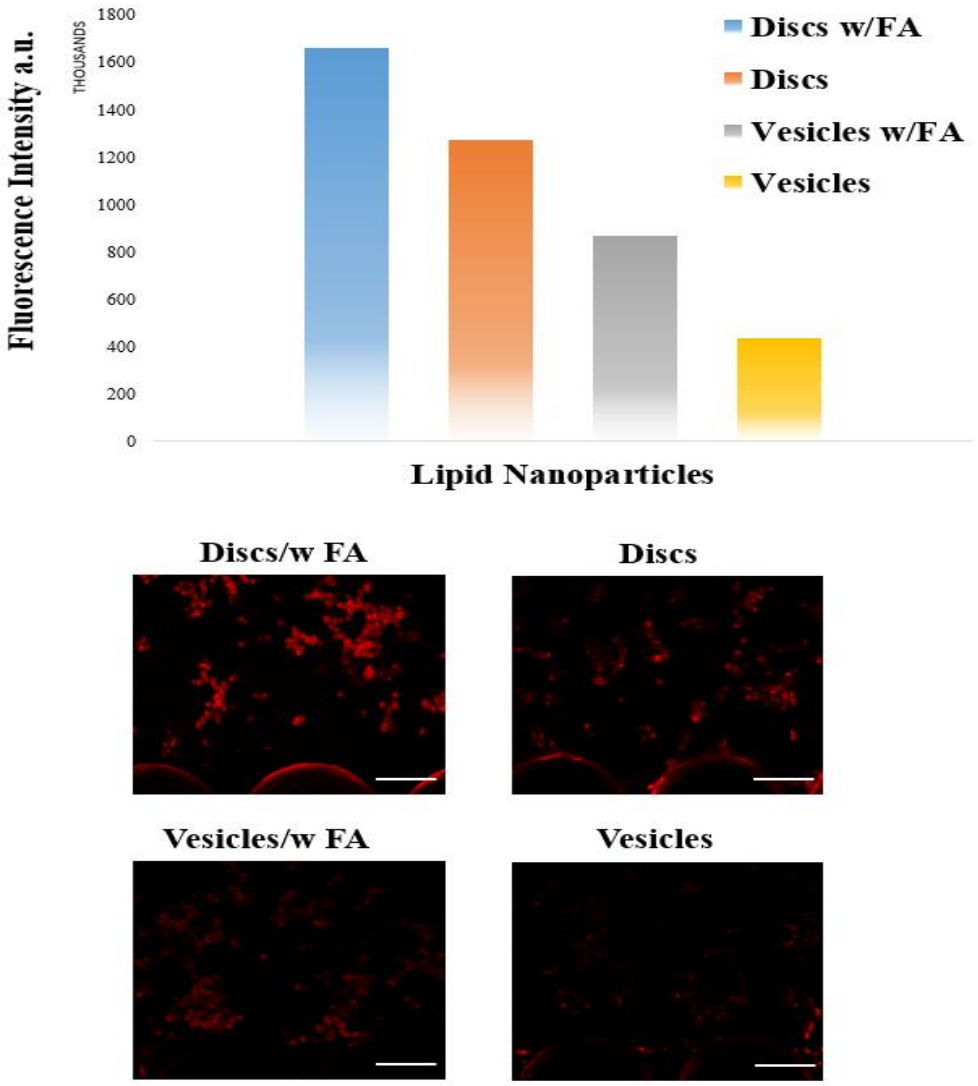

Figure 4-8 Comparison of active and passive accumulation in tumor tissue after 12 hours. Scale bar is 100 μm.

4.4 Conclusion

Our design of the microfluidic device shows very promising potential over previous *in vitro* studies where tumor spheroids used to stay in a static solution for several hours to be disrupted before or after incubation with nanocarriers.[110, 128, 190] Here the tumor intact by the surrounding hydrogel which mimics the microstructure of the ECM of most solid tumors.[199, 200] also, the design reveal the real-time imaging of tumor using confocal microscopy which provided a way into understanding the interactions between NP and tissue under controllable flow conditions at very early stage. Our experimental set-up permits more accurate assessment of the impact of NP's physicochemical properties (i.e. shape and targeting) on its transportation through the ECM and eventually into the tumor. The information we collected from our study of monitoring the early interaction between NP and tissue using microfluidic for 3D tumor aggregates may successfully predict the behavior of NPs in the long-term *in vivo* studies.

Chapter 5. Summary and Future Directions

5.1 Summary

Since nanotechnology gained a huge attention in the world of cancer treatment and diagnostic, it is essential to uncover some of the fundamental design criteria to improve the efficiency of nanoparticle delivery and uptake. In this work, we have accomplished several significant findings toward a better understanding of the nano-bio interactions. First, our work verified the importance of the morphology of NPs in the enhancement of delivery and cellular retention. As of today, most of the cancer drug carriers that are commercially used were in the spherical shape. However, here we could synthesize very stable discoidal lipid-based nanostructures and substantiated their advantageous to interact with different types of cancer cells over the vesicular NPs which were made from the same lipid mixture. Also, we demonstrated that several cancer cells (i.e. CCRF-CEM, KB and Ovcar-8 cell lines) respond differently to the morphology of the nanoparticle, and thus, they had different mechanisms of uptake based on each shape. These observations are crucial to providing a direct benefit for enhanced delivery of nanocarriers to cancer cells.

This work also covered the importance of targeting molecules in enhancing delivery and uptake by cancer cells. Targeting with folic acid has been used because of its very high binding affinity, and the exceeding distribution of its receptors on the surface of many cancer cells. Our results exposed the impact of targeting in the improvement of cellular uptake of both discoidal and vesicular lipid-based nanoparticles. In addition, it confirmed our previous findings that shape is matter and discoidal folate lipid NPs have more potential in cancer treatment and diagnostic. We also proved that folate NPs were mainly internalized into cancer cells via folate receptor-mediated

endocytosis. Also, we demonstrated that folate NPs were localized in cytoplasm indicating that they followed endocytosis pathway to internalize into the cells. Then they were distributed in the cytoplasm after escaping from the endosome and the lysosome. During the animal study, we observed a higher tumor uptake of folate disc NPs in comparison with folate vesicle NPs at different time points. Similar observation was made in the case of none folate disc NPs and none folate vesicle NPs. These results are strong evidence of the role of both morphology and targeting in the enhancement of the penetration of NPs in the tumor.

Moreover, this makes our findings especially significant because it provides a detailed quantitative analysis of the interplay between shape and cellular uptake, which offers principles for drug carrier design. The significant of the discoidal shape of the self-assembled lipid nanoparticle over the vesicular one offers potential application of this nanostructure in cancer diagnostic and therapeutic.

To extend our understanding of the relationship between the design of the nanoparticles and their interaction with the tumor and the surrounding tissue structure, we developed the concept of tumor on the chip to serve as a backbone for future *in vivo* tests. The design, fabrication, and evaluation of hydrogel cell culture microfluidic device that can be used to monitor nanoparticle penetration and delivery to 3D cancer cells was accomplished in this study, too. The device met all essential design criteria for this application, including the viable cell culture in a 3D matrix, the imposition of fluid flow through the 3D cell culture, and the live cell imaging during perfusion. Moreover, we could proof the feasibility of using this device to investigate the effect of shape (discoidal and vesicular) with the addition of folic acid (FA) targeting on the penetration of nanoparticle through the hydrogel to 3D ovarian cancer cells. That may lead to identifying the dosage of anticancer drugs for *in vitro* experiments, saving time and reducing costs.

The above contributions will advance the field of nanoparticles manufacturing for drug delivery and will improve the efficacy of cancer treatment. It should be noticed that the simplicity of the fabrication process of our nanocarriers, as well as the uniformity and the stability of the obtained structure, can be used for the next generation of drug carriers. Overall, this study of several *in vitro* tumor models has highlighted the unique potential and flexibility of the shape and targeting specific nanoparticles in versatile implications in the field of tumor therapeutics and diagnostics.

5.2 Future studies

As of future work, the encapsulation of hydrophobic anticancer drugs in the bilayers of the discoidal lipid nanoparticles is our next step. Thus, we could verify the effectiveness of the discoidal lipid nanoparticles in drug delivery. Also, we may incorporate imaging agents such as quantum dots with the drug to serve both as a diagnostic and therapeutic carrier. Furthermore, the microchannel device we fabricated here can be used as a platform to investigate the compatibility of the nanocarriers. Several types of cells can be encapsulated in the microfluidic device including cancer, normal and stem cells to investigate in real time the trafficking and fate of the nanoparticles with each cell type. Further analysis of the transportation of the nanoparticle inside the blood vessels and all the way to the target tissue will be performed. Conducting mathematical analysis could be useful to improve the design of the microchannel device. Moreover, confirming these results must be performed *in vivo* before applications in drug delivery can be considered further.

5.3 References

1. Singh, R., P. Kumari, and S. Kumar, *11 - Nanotechnology for enhanced bioactivity of bioactive phytomolecules A2 - Grumezescu, Alexandru Mihai*, in *Nutrient Delivery*. 2017, Academic Press. p. 413-456.
2. Brys, A.K., et al., *Nanotechnology-based strategies for combating toxicity and resistance in melanoma therapy.* Biotechnology Advances, 2016. **34**(5): p. 565-577.
3. Research, I.I.f.P.E., *Proceedings of the International Conference on Production Engineering*. On the basic concept of nano-technology. 1974: Japan Society of Precision Engineering.
4. Davis, M.E., Z. Chen, and D.M. Shin, *Nanoparticle therapeutics: an emerging treatment modality for cancer.* Nat Rev Drug Discov, 2008. **7**(9): p. 771-782.
5. Zhang, L., et al., *Nanoparticles in medicine: therapeutic applications and developments.* Clin. Pharmacol. Ther., 2008. **83**(5): p. 761-9.
6. Kreuter, J., *Nanoparticles—a historical perspective.* International Journal of Pharmaceutics, 2007. **331**(1): p. 1-10.
7. Miele, E., et al., *Albumin-bound formulation of paclitaxel (Abraxane(®) ABI-007) in the treatment of breast cancer.* International Journal of Nanomedicine, 2009. **4**: p. 99-105.
8. Alibolandi, M., et al., *In vitro and in vivo evaluation of therapy targeting epithelial-cell adhesion-molecule aptamers for non-small cell lung cancer.* J Control Release, 2015.
9. de la Rica, R., D. Aili, and M.M. Stevens, *Enzyme-responsive nanoparticles for drug release and diagnostics.* Adv. Drug Deliv. Rev., 2012. **64**(11): p. 967-78.
10. Kong, G., R.D. Braun, and M.W. Dewhirst, *Hyperthermia enables tumor-specific nanoparticle delivery: effect of particle size.* Cancer Res, 2000. **60**(16): p. 4440-5.
11. Lam, A.K., et al., *Quantitative imaging of electron transfer flavoprotein autofluorescence reveals the dynamics of lipid partitioning in living pancreatic islets.* Integr Biol (Camb), 2012. **4**(8): p. 838-46.
12. Torchilin, V.P., *Recent advances with liposomes as pharmaceutical carriers.* Nat Rev Drug Discov, 2005. **4**(2): p. 145-60.
13. Puri, A., et al., *Lipid-based nanoparticles as pharmaceutical drug carriers: from concepts to clinic.* Crit Rev Ther Drug Carrier Syst, 2009. **26**(6): p. 523-80.
14. Rai, M., A. Yadav, and A. Gade, *Silver nanoparticles as a new generation of antimicrobials.* Biotechnology Advances, 2009. **27**(1): p. 76-83.
15. Mason, T.G., et al., *Nanoemulsions: formation, structure, and physical properties.* Journal of Physics: Condensed Matter, 2006. **18**(41): p. R635.
16. Daniel, M.-C. and D. Astruc, *Gold Nanoparticles: Assembly, Supramolecular Chemistry, Quantum-Size-Related Properties, and Applications toward Biology, Catalysis, and Nanotechnology.* Chemical Reviews, 2004. **104**(1): p. 293-346.
17. Nel, A.E., et al., *Understanding biophysicochemical interactions at the nano-bio interface.* Nat Mater, 2009. **8**(7): p. 543-57.
18. Albanese, A., P.S. Tang, and W.C. Chan, *The effect of nanoparticle size, shape, and surface chemistry on biological systems.* Annu Rev Biomed Eng, 2012. **14**: p. 1-16.
19. Endres, T., et al., *Optimising the self-assembly of siRNA loaded PEG-PCL-lPEI nano-carriers employing different preparation techniques.* J Control Release, 2012. **160**(3): p. 583-91.
20. Duncan, R., *The dawning era of polymer therapeutics.* Nat Rev Drug Discov, 2003. **2**(5): p. 347-60.
21. Kumari, A., S.K. Yadav, and S.C. Yadav, *Biodegradable polymeric nanoparticles based drug delivery systems.* Colloids and Surfaces B: Biointerfaces, 2010. **75**(1): p. 1-18.
22. Liechty, W.B., et al., *Polymers for Drug Delivery Systems.* Annual review of chemical and biomolecular engineering, 2010. **1**: p. 149-173.
23. Pelegri-O'Day, E.M., E.-W. Lin, and H.D. Maynard, *Therapeutic Protein–Polymer Conjugates: Advancing Beyond PEGylation.* Journal of the American Chemical Society, 2014. **136**(41): p. 14323-14332.

24. Nauka, P.C., J. Lee, and H.D. Maynard, *Enhancing the conjugation yield of brush polymer-protein conjugates by increasing the linker length at the polymer end-group.* Polymer Chemistry, 2016. **7**(13): p. 2352-2357.
25. Kedar, U., et al., *Advances in polymeric micelles for drug delivery and tumor targeting.* Nanomedicine: Nanotechnology, Biology and Medicine, 2010. **6**(6): p. 714-729.
26. Croy, S.R. and G.S. Kwon, *Polymeric micelles for drug delivery.* Curr Pharm Des, 2006. **12**(36): p. 4669-84.
27. Rink, J.S., et al., *Update on Current and Potential Nanoparticle Cancer Therapies.* Current opinion in oncology, 2013. **25**(6): p. 646-651.
28. Wilczewska, A.Z., et al., *Nanoparticles as drug delivery systems.* Pharmacol Rep, 2012. **64**(5): p. 1020-37.
29. Mudshinge, S.R., et al., *Nanoparticles: Emerging carriers for drug delivery.* Saudi Pharmaceutical Journal, 2011. **19**(3): p. 129-141.
30. Gabizon, A.A., *Pegylated liposomal doxorubicin: metamorphosis of an old drug into a new form of chemotherapy.* Cancer Invest, 2001. **19**(4): p. 424-36.
31. Green, A.E. and P.G. Rose, *Pegylated liposomal doxorubicin in ovarian cancer.* International Journal of Nanomedicine, 2006. **1**(3): p. 229-239.
32. Duggan, S.T. and G.M. Keating, *Pegylated Liposomal Doxorubicin.* Drugs, 2011. **71**(18): p. 2531-2558.
33. Zhang, L., et al., *Nanoparticles in Medicine: Therapeutic Applications and Developments.* Clinical Pharmacology & Therapeutics, 2008. **83**(5): p. 761-769.
34. Allen, T.M. and P.R. Cullis, *Liposomal drug delivery systems: From concept to clinical applications.* Advanced Drug Delivery Reviews, 2013. **65**(1): p. 36-48.
35. Koning, G.A. and G. Storm, *Targeted drug delivery systems for the intracellular delivery of macromolecular drugs.* Drug Discov Today, 2003. **8**(11): p. 482-3.
36. Metselaar, J.M. and G. Storm, *Liposomes in the treatment of inflammatory disorders.* Expert Opin Drug Deliv, 2005. **2**(3): p. 465-76.
37. Hua, S. and S.Y. Wu, *The use of lipid-based nanocarriers for targeted pain therapies.* Front Pharmacol, 2013. **4**: p. 143.
38. Kroon, J., et al., *Liposomal delivery of dexamethasone attenuates prostate cancer bone metastatic tumor growth In Vivo.* The Prostate, 2015. **75**(8): p. 815-824.
39. Ulrich, A.S., *Biophysical aspects of using liposomes as delivery vehicles.* Biosci Rep, 2002. **22**(2): p. 129-50.
40. Gabizon, A., et al., *Liposomes as in vivo carriers of adriamycin: reduced cardiac uptake and preserved antitumor activity in mice.* Cancer Res, 1982. **42**(11): p. 4734-9.
41. Nieh, M.-P., et al., *SANS Study on the Effect of Lanthanide Ions and Charged Lipids on the Morphology of Phospholipid Mixtures.* Biophysical Journal, 2002. **82**(5): p. 2487-2498.
42. Iqbal, U., et al., *Small unilamellar vesicles: a platform technology for molecular imaging of brain tumors.* Nanotechnology, 2011. **22**(19): p. 195102.
43. Nieh, M.P., N. Kucerka, and J. Katsaras, *Spontaneously formed unilamellar vesicles.* Methods Enzymol., 2009. **465**: p. 3-20.
44. Nieh, M.P., et al., *Spontaneously formed unilamellar vesicles with path-dependent size distribution.* Langmuir, 2005. **21**(15): p. 6656-61.
45. Nieh, M.P., et al., *Formation of kinetically trapped nanoscopic unilamellar vesicles from metastable nanodiscs.* Langmuir, 2011. **27**(23): p. 14308-16.
46. Chithrani, B.D., A.A. Ghazani, and W.C. Chan, *Determining the size and shape dependence of gold nanoparticle uptake into mammalian cells.* Nano Lett., 2006. **6**(4): p. 662-8.
47. Cho, E.C., et al., *The effects of size, shape, and surface functional group of gold nanostructures on their adsorption and internalization by cells.* Small, 2010. **6**(4): p. 517-22.
48. Desai, M.P., et al., *The mechanism of uptake of biodegradable microparticles in Caco-2 cells is size dependent.* Pharm. Res., 1997. **14**(11): p. 1568-73.

49. Li, X., *Size and shape effects on receptor-mediated endocytosis of nanoparticles.* J. Appl. Phys. , 2012. **111**(2): p. -.
50. Al Kobiasi, M., et al., *Control of size dispersity of chitosan biopolymer microparticles and nanoparticles to influence vaccine trafficking and cell uptake.* J. Biomed. Mater. Res., Part A, 2012. **100**(7): p. 1859-67.
51. Arnida, A. Malugin, and H. Ghandehari, *Cellular uptake and toxicity of gold nanoparticles in prostate cancer cells: a comparative study of rods and spheres.* J. Appl. Toxicol. , 2010. **30**(3): p. 212-7.
52. Florez, L., et al., *How shape influences uptake: interactions of anisotropic polymer nanoparticles and human mesenchymal stem cells.* Small, 2012. **8**(14): p. 2222-30.
53. Stefanick, J.F., et al., *A systematic analysis of peptide linker length and liposomal polyethylene glycol coating on cellular uptake of peptide-targeted liposomes.* ACS Nano, 2013. **7**(4): p. 2935-47.
54. Agarwal, R., et al., *Mammalian cells preferentially internalize hydrogel nanodiscs over nanorods and use shape-specific uptake mechanisms.* Proceedings of the National Academy of Sciences, 2013.
55. Safari, J. and Z. Zarnegar, *Advanced drug delivery systems: Nanotechnology of health design A review.* Journal of Saudi Chemical Society, 2014. **18**(2): p. 85-99.
56. Alexis, F., et al., *Factors affecting the clearance and biodistribution of polymeric nanoparticles.* Mol Pharm, 2008. **5**(4): p. 505-15.
57. Perez-Herrero, E. and A. Fernandez-Medarde, *Advanced targeted therapies in cancer: Drug nanocarriers, the future of chemotherapy.* Eur J Pharm Biopharm, 2015. **93**: p. 52-79.
58. Patra, C.R., et al., *Targeted delivery of gemcitabine to pancreatic adenocarcinoma using cetuximab as a targeting agent.* Cancer Res, 2008. **68**(6): p. 1970-8.
59. Yu, B., et al., *Receptor-targeted nanocarriers for therapeutic delivery to cancer.* Mol Membr Biol, 2010. **27**(7): p. 286-98.
60. Koning, G.A. and G.C. Krijger, *Targeted multifunctional lipid-based nanocarriers for image-guided drug delivery.* Anticancer Agents Med Chem, 2007. **7**(4): p. 425-40.
61. Alexis, F., et al., *HER-2-targeted nanoparticle-affibody bioconjugates for cancer therapy.* ChemMedChem, 2008. **3**(12): p. 1839-43.
62. Low, P.S. and A.C. Antony, *Folate receptor-targeted drugs for cancer and inflammatory diseases.* Adv Drug Deliv Rev, 2004. **56**(8): p. 1055-8.
63. Antony, A.C., *Folate receptors.* Annu Rev Nutr, 1996. **16**: p. 501-21.
64. Kelemen, L.E., *The role of folate receptor alpha in cancer development, progression and treatment: cause, consequence or innocent bystander?* Int J Cancer, 2006. **119**(2): p. 243-50.
65. Zwicke, G.L., G.A. Mansoori, and C.J. Jeffery, *Utilizing the folate receptor for active targeting of cancer nanotherapeutics.* Nano Reviews, 2012. **3**: p. 10.3402/nano.v3i0.18496.
66. Vlashi, E., et al., *Effect of Folate-Targeted Nanoparticle Size on Their Rates of Penetration into Solid Tumors.* ACS Nano, 2013. **7**(10): p. 8573-8582.
67. Nogueira, E., et al., *Folate-targeted nanoparticles for rheumatoid arthritis therapy.* Nanomedicine: Nanotechnology, Biology and Medicine. **12**(4): p. 1113-1126.
68. Werner, M.E., et al., *Folate-targeted nanoparticle delivery of chemo- and radiotherapeutics for the treatment of ovarian cancer peritoneal metastasis.* Biomaterials, 2011. **32**(33): p. 8548-8554.
69. Nukolova, N.V., et al., *Folate-decorated nanogels for targeted therapy of ovarian cancer.* Biomaterials, 2011. **32**(23): p. 5417-5426.
70. Yoo, H.S. and T.G. Park, *Folate-receptor-targeted delivery of doxorubicin nano-aggregates stabilized by doxorubicin-PEG-folate conjugate.* J Control Release, 2004. **100**(2): p. 247-56.
71. Kim, Y.K., et al., *Therapeutic efficiency of folated poly(ethylene glycol)-chitosan-graft-polyethylenimine-Pdcd4 complexes in H-ras12V mice with liver cancer.* Int J Nanomedicine, 2013. **8**: p. 1489-98.
72. Rathinaraj, P., et al., *Targeted images of KB cells using folate-conjugated gold nanoparticles.* Nanoscale Research Letters, 2015. **10**: p. 5.
73. Zhang, L., et al., *Folate-modified lipid-polymer hybrid nanoparticles for targeted paclitaxel delivery.* Int J Nanomedicine, 2015. **10**: p. 2101-14.

74. Jiang, W., et al., *Nanoparticle-mediated cellular response is size-dependent.* Nat Nanotechnol, 2008. **3**(3): p. 145-50.
75. Verma, A. and F. Stellacci, *Effect of surface properties on nanoparticle-cell interactions.* Small, 2010. **6**(1): p. 12-21.
76. Abbott, A., *Cell culture: biology's new dimension.* Nature, 2003. **424**(6951): p. 870-2.
77. Debnath, J. and J.S. Brugge, *Modelling glandular epithelial cancers in three-dimensional cultures.* Nat Rev Cancer, 2005. **5**(9): p. 675-88.
78. Schmeichel, K.L. and M.J. Bissell, *Modeling tissue-specific signaling and organ function in three dimensions.* J Cell Sci, 2003. **116**(Pt 12): p. 2377-88.
79. Weigelt, B. and M.J. Bissell, *Unraveling the microenvironmental influences on the normal mammary gland and breast cancer.* Semin Cancer Biol, 2008. **18**(5): p. 311-21.
80. Wang, Y., et al., *Evaluating the pharmacokinetics and in vivo cancer targeting capability of Au nanocages by positron emission tomography imaging.* ACS Nano, 2012. **6**(7): p. 5880-8.
81. Xie, H., et al., *Effect of intratumoral administration on biodistribution of 64Cu-labeled nanoshells.* Int J Nanomedicine, 2012. **7**: p. 2227-38.
82. Xie, H., et al., *In vivo PET imaging and biodistribution of radiolabeled gold nanoshells in rats with tumor xenografts.* Int J Pharm, 2010. **395**(1-2): p. 324-30.
83. Toy, R., et al., *Multimodal in vivo imaging exposes the voyage of nanoparticles in tumor microcirculation.* ACS Nano, 2013. **7**(4): p. 3118-29.
84. Holtfreter, J., *A study of the mechanics of gastrulation. Part I.* Journal of Experimental Zoology, 1943. **94**(3): p. 261-318.
85. Moscona, A. and H. Moscona, *The dissociation and aggregation of cells from organ rudiments of the early chick embryo.* Journal of Anatomy, 1952. **86**(Pt 3): p. 287-301.
86. Hirschhaeuser, F., et al., *Multicellular tumor spheroids: an underestimated tool is catching up again.* J Biotechnol, 2010. **148**(1): p. 3-15.
87. Kelm, J.M. and M. Fussenegger, *Microscale tissue engineering using gravity-enforced cell assembly.* Trends Biotechnol, 2004. **22**(4): p. 195-202.
88. Zhang, W., et al., *Optimization of the formation of embedded multicellular spheroids of MCF-7 cells: How to reliably produce a biomimetic 3D model.* Anal Biochem, 2016. **515**: p. 47-54.
89. Mehta, G., et al., *Opportunities and challenges for use of tumor spheroids as models to test drug delivery and efficacy.* Journal of Controlled Release, 2012. **164**(2): p. 192-204.
90. Ma, H.L., et al., *Multicellular tumor spheroids as an in vivo-like tumor model for three-dimensional imaging of chemotherapeutic and nano material cellular penetration.* Mol Imaging, 2012. **11**(6): p. 487-98.
91. Whitesides, G.M., *The origins and the future of microfluidics.* Nature, 2006. **442**(7101): p. 368-73.
92. Pushkarsky, I., et al., *Research highlights: microfluidics and magnets.* Lab on a Chip, 2014. **14**(16): p. 2882-2886.
93. Wu, L.Y., D. Di Carlo, and L.P. Lee, *Microfluidic self-assembly of tumor spheroids for anticancer drug discovery.* Biomed Microdevices, 2008. **10**(2): p. 197-202.
94. Napolitano, A.P., et al., *Dynamics of the self-assembly of complex cellular aggregates on micromolded nonadhesive hydrogels.* Tissue Eng, 2007. **13**(8): p. 2087-94.
95. Dean, D.M., et al., *Rods, tori, and honeycombs: the directed self-assembly of microtissues with prescribed microscale geometries.* Faseb j, 2007. **21**(14): p. 4005-12.
96. Karp, J.M., et al., *Controlling size, shape and homogeneity of embryoid bodies using poly(ethylene glycol) microwells.* Lab Chip, 2007. **7**(6): p. 786-94.
97. Khademhosseini, A., et al., *Micromolding of photocrosslinkable hyaluronic acid for cell encapsulation and entrapment.* J Biomed Mater Res A, 2006. **79**(3): p. 522-32.
98. An, D., K. Kim, and J. Kim, *Microfluidic System Based High Throughput Drug Screening System for Curcumin/TRAIL Combinational Chemotherapy in Human Prostate Cancer PC3 Cells.* Biomolecules & Therapeutics, 2014. **22**(4): p. 355-362.
99. Kim, J., et al., *A programmable microfluidic cell array for combinatorial drug screening.* Lab Chip,

2012. **12**(10): p. 1813-22.
100. Liu, D., et al., *Parallel microfluidic networks for studying cellular response to chemical modulation.* J Biotechnol, 2007. **131**(3): p. 286-92.
101. Nie, F.-Q., et al., *On-chip cell migration assay using microfluidic channels.* Biomaterials, 2007. **28**(27): p. 4017-4022.
102. Tokuyama, T., et al., *Microbioassay System for Antiallergic Drug Screening Using Suspension Cells Retaining in a Poly(dimethylsiloxane) Microfluidic Device.* Analytical Chemistry, 2005. **77**(10): p. 3309-3314.
103. Kang, A., et al., *Concave microwell array-mediated three-dimensional tumor model for screening anticancer drug-loaded nanoparticles.* Nanomedicine: Nanotechnology, Biology and Medicine, 2015. **11**(5): p. 1153-1161.
104. Mohr, J.C., J.J. de Pablo, and S.P. Palecek, *3-D microwell culture of human embryonic stem cells.* Biomaterials, 2006. **27**(36): p. 6032-42.
105. Huh, D., et al., *Microfabrication of human organs-on-chips.* Nat. Protocols, 2013. **8**(11): p. 2135-2157.
106. Bersini, S., et al., *A microfluidic 3D in vitro model for specificity of breast cancer metastasis to bone.* Biomaterials, 2014. **35**(8): p. 2454-61.
107. Aref, A.R., et al., *Screening therapeutic EMT blocking agents in a three-dimensional microenvironment.* Integr Biol (Camb), 2013. **5**(2): p. 381-9.
108. Holohan, C., et al., *Cancer drug resistance: an evolving paradigm.* Nat Rev Cancer, 2013. **13**(10): p. 714-726.
109. Horning, J.L., et al., *3-D tumor model for in vitro evaluation of anticancer drugs.* Mol Pharm, 2008. **5**(5): p. 849-62.
110. Mitra, M., et al., *A novel in vitro three-dimensional retinoblastoma model for evaluating chemotherapeutic drugs.* Mol Vis, 2012. **18**: p. 1361-78.
111. Shin, C.S., et al., *Development of an in vitro 3D tumor model to study therapeutic efficiency of an anticancer drug.* Mol Pharm, 2013. **10**(6): p. 2167-75.
112. Toley, B.J., et al., *Microfluidic technique to measure intratumoral transport and calculate drug efficacy shows that binding is essential for doxorubicin and release hampers Doxil.* Integr Biol (Camb), 2013. **5**(9): p. 1184-96.
113. Szot, C.S., et al., *3D in vitro bioengineered tumors based on collagen I hydrogels.* Biomaterials, 2011. **32**(31): p. 7905-12.
114. Sutherland, R.M., *Cell and environment interactions in tumor microregions: the multicell spheroid model.* Science, 1988. **240**(4849): p. 177-84.
115. Albanese, A., et al., *Tumour-on-a-chip provides an optical window into nanoparticle tissue transport.* Nat Commun, 2013. **4**: p. 2718.
116. Ng, C.P. and S.H. Pun, *A perfusable 3D cell-matrix tissue culture chamber for in situ evaluation of nanoparticle vehicle penetration and transport.* Biotechnol Bioeng, 2008. **99**(6): p. 1490-501.
117. Toy, R., et al., *Effect of Particle Size, Density and Shape on Margination of Nanoparticles in Microcirculation.* Nanotechnology, 2011. **22**(11): p. 115101-115101.
118. Valencia, P.M., et al., *Microfluidic technologies for accelerating the clinical translation of nanoparticles.* Nat Nanotechnol, 2012. **7**(10): p. 623-9.
119. Tan, S.J., et al., *Engineering Nanocarriers for siRNA Delivery.* Small, 2011. **7**(7): p. 841-56.
120. Liu, G., et al., *FUNCTIONAL NANOPARTICLES FOR MOLECULAR IMAGING GUIDED GENE DELIVERY.* Nano Today, 2010. **5**(6): p. 524-539.
121. Truong, N.P., et al., *The importance of nanoparticle shape in cancer drug delivery.* Expert Opin Drug Deliv, 2015. **12**(1): p. 129-42.
122. Barua, S., et al., *Particle shape enhances specificity of antibody-displaying nanoparticles.* Proceedings of the National Academy of Sciences, 2013. **110**(9): p. 3270-3275.
123. Zhang, K., et al., *Shape effects of nanoparticles conjugated with cell-penetrating peptides (HIV Tat PTD) on CHO cell uptake.* Bioconjug Chem, 2008. **19**(9): p. 1880-7.

124. Alemdaroglu, F.E., et al., *Cellular Uptake of DNA Block Copolymer Micelles with Different Shapes.* Macromol. Rapid Commun., 2008. **29**(4): p. 326-329.
125. Ferris, D.P., et al., *Synthesis of biomolecule-modified mesoporous silica nanoparticles for targeted hydrophobic drug delivery to cancer cells.* Small, 2011. **7**(13): p. 1816-26.
126. Shang, L., K. Nienhaus, and G.U. Nienhaus, *Engineered nanoparticles interacting with cells: size matters.* J Nanobiotechnology, 2014. **12**: p. 5.
127. Shanmugam, T. and R. Banerjee, *Nanostructured self assembled lipid materials for drug delivery and tissue engineering.* Ther. Delivery, 2011. **2**(11): p. 1485-516.
128. Goodman, T.T., P.L. Olive, and S.H. Pun, *Increased nanoparticle penetration in collagenase-treated multicellular spheroids.* Int. J. Nanomed., 2007. **2**(2): p. 265-274.
129. Huang, K., et al., *Size-dependent localization and penetration of ultrasmall gold nanoparticles in cancer cells, multicellular spheroids, and tumors in vivo.* ACS Nano, 2012. **6**(5): p. 4483-93.
130. Cabral, H., et al., *Accumulation of sub-100 nm polymeric micelles in poorly permeable tumours depends on size.* Nat. Nanotechnol., 2011. **6**(12): p. 815-23.
131. Nieh, M.-P., et al., *SANS Study on the Effect of Lanthanide Ions and Charged Lipids on the Morphology of Phospholipid Mixtures.* Biophys. J., 2002. **82**(5): p. 2487-2498.
132. Ames, B.N. and D.T. Dubin, *The role of polyamines in the neutralization of bacteriophage deoxyribonucleic acid.* J. Biol. Chem., 1960. **235**: p. 769-75.
133. Smith, B., et al., *Hyperthermia-triggered intracellular delivery of anticancer agent to HER2(+) cells by HER2-specific affibody (ZHER2-GS-Cys)-conjugated thermosensitive liposomes (HER2(+) affisomes).* J. Controlled Release, 2011. **153**(2): p. 187-94.
134. Liu, Y., et al., *The effects of temperature, salinity, concentration and PEGylated lipid on the spontaneous nanostructures of bicellar mixtures.* Biochim. Biophys. Acta, 2014. **1838**(7): p. 1871-80.
135. Nieh, M.P., et al., *Spontaneously Formed Monodisperse Biomimetic Unilamellar Vesicles: The Effect of Charge, Dilution, and Time.* Biophys. J., 2004. **86**(4): p. 2615-2629.
136. Deng, Z.J., et al., *Plasma protein binding of positively and negatively charged polymer-coated gold nanoparticles elicits different biological responses.* Nanotoxicology, 2013. **7**(3): p. 314-22.
137. Immordino, M.L., F. Dosio, and L. Cattel, *Stealth liposomes: review of the basic science, rationale, and clinical applications, existing and potential.* Int. J. Nanomed., 2006. **1**(3): p. 297-315.
138. Aggarwal, P., et al., *Nanoparticle interaction with plasma proteins as it relates to particle biodistribution, biocompatibility and therapeutic efficacy.* Adv. Drug Delivery Rev., 2009. **61**(6): p. 428-37.
139. Hu, A., et al., *Lipid-based nanodiscs as models for studying mesoscale coalescence--a transport limited case.* Soft Matter, 2014. **10**(28): p. 5055-60.
140. Puri, A., et al., *HER2-specific affibody-conjugated thermosensitive liposomes (Affisomes) for improved delivery of anticancer agents.* J Liposome Res, 2008. **18**(4): p. 293-307.
141. Agarwal, R., et al., *Mammalian cells preferentially internalize hydrogel nanodiscs over nanorods and use shape-specific uptake mechanisms.* PNAS, 2013. **110**(43): p. 17247-52.
142. Herd, H., et al., *Nanoparticle geometry and surface orientation influence mode of cellular uptake.* ACS Nano, 2013. **7**(3): p. 1961-73.
143. Vranic, S., et al., *Deciphering the mechanisms of cellular uptake of engineered nanoparticles by accurate evaluation of internalization using imaging flow cytometry.* Part. Fibre Toxicol., 2013. **10**: p. 2.
144. Ivanov, A.I., *Pharmacological inhibition of endocytic pathways: is it specific enough to be useful?* Methods Mol. Biol. (N. Y.), 2008. **440**: p. 15-33.
145. dos Santos, T., et al., *Effects of transport inhibitors on the cellular uptake of carboxylated polystyrene nanoparticles in different cell lines.* PLoS One, 2011. **6**(9): p. e24438.
146. Chithrani, B.D., A.A. Ghazani, and W.C. Chan, *Determining the size and shape dependence of gold nanoparticle uptake into mammalian cells.* Nano letters, 2006. **6**(4): p. 662-668.
147. Kirchner, C., et al., *Cytotoxicity of colloidal CdSe and CdSe/ZnS nanoparticles.* Nano letters, 2005.

5(2): p. 331-338.
148. Hauck, T.S., A.A. Ghazani, and W.C. Chan, *Assessing the effect of surface chemistry on gold nanorod uptake, toxicity, and gene expression in mammalian cells.* Small, 2008. **4**(1): p. 153-159.
149. Cho, E.C., et al., *Understanding the role of surface charges in cellular adsorption versus internalization by selectively removing gold nanoparticles on the cell surface with a I2/KI etchant.* Nano letters, 2009. **9**(3): p. 1080-1084.
150. Albanese, A., P.S. Tang, and W.C. Chan, *The effect of nanoparticle size, shape, and surface chemistry on biological systems.* Annual review of biomedical engineering, 2012. **14**: p. 1-16.
151. Torchilin, V.P., *Recent advances with liposomes as pharmaceutical carriers.* Nature reviews Drug discovery, 2005. **4**(2): p. 145-160.
152. MuÈller, R.H., K. MaÈder, and S. Gohla, *Solid lipid nanoparticles (SLN) for controlled drug delivery–a review of the state of the art.* European journal of pharmaceutics and biopharmaceutics, 2000. **50**(1): p. 161-177.
153. Dreher, M.R., et al., *Tumor vascular permeability, accumulation, and penetration of macromolecular drug carriers.* Journal of the National Cancer Institute, 2006. **98**(5): p. 335-344.
154. Patri, A.K., I.J. Majoros, and J.R. Baker, *Dendritic polymer macromolecular carriers for drug delivery.* Current opinion in chemical biology, 2002. **6**(4): p. 466-471.
155. Liu, M., et al., *The preparation and characterization of micelles from poly (γ-glutamic acid)-graft-poly (L-lactide) and the cellular uptake thereof.* Journal of Materials Science: Materials in Medicine, 2015. **26**(5): p. 1-9.
156. Ernsting, M.J., et al., *Factors controlling the pharmacokinetics, biodistribution and intratumoral penetration of nanoparticles.* J Control Release, 2013. **172**(3): p. 782-94.
157. Tan, J., et al., *The influence of size, shape and vessel geometry on nanoparticle distribution.* Microfluid Nanofluidics, 2013. **14**(1-2): p. 77-87.
158. Venkataraman, S., et al., *The effects of polymeric nanostructure shape on drug delivery.* Advanced Drug Delivery Reviews, 2011. **63**(14–15): p. 1228-1246.
159. Blanco, E., H. Shen, and M. Ferrari, *Principles of nanoparticle design for overcoming biological barriers to drug delivery.* Nature biotechnology, 2015. **33**(9): p. 941-951.
160. Gratton, S.E., et al., *The effect of particle design on cellular internalization pathways.* Proceedings of the National Academy of Sciences, 2008. **105**(33): p. 11613-11618.
161. Qiu, Y., et al., *Surface chemistry and aspect ratio mediated cellular uptake of Au nanorods.* Biomaterials, 2010. **31**(30): p. 7606-7619.
162. Allen, T.M., *Ligand-targeted therapeutics in anticancer therapy.* Nature Reviews Cancer, 2002. **2**(10): p. 750-763.
163. Zhang, Z., et al., *Conjugating folic acid to gold nanoparticles through glutathione for targeting and detecting cancer cells.* Bioorganic & Medicinal Chemistry, 2010. **18**(15): p. 5528-5534.
164. Zheng, Y., et al., *Transferrin-conjugated lipid-coated PLGA nanoparticles for targeted delivery of aromatase inhibitor 7α-APTADD to breast cancer cells.* International Journal of Pharmaceutics, 2010. **390**(2): p. 234-241.
165. Vlashi, E., et al., *Effect of folate-targeted nanoparticle size on their rates of penetration into solid tumors.* ACS Nano, 2013. **7**(10): p. 8573-82.
166. Weitman, S.D., et al., *Distribution of the folate receptor GP38 in normal and malignant cell lines and tissues.* Cancer Res, 1992. **52**(12): p. 3396-401.
167. Ross, J.F., P.K. Chaudhuri, and M. Ratnam, *Differential regulation of folate receptor isoforms in normal and malignant tissues in vivo and in established cell lines. Physiologic and clinical implications.* Cancer, 1994. **73**(9): p. 2432-43.
168. Parker, N., et al., *Folate receptor expression in carcinomas and normal tissues determined by a quantitative radioligand binding assay.* Anal Biochem, 2005. **338**(2): p. 284-93.
169. Xiao, K., et al., *The effect of surface charge on in vivo biodistribution of PEG-oligocholic acid based micellar nanoparticles.* Biomaterials, 2011. **32**(13): p. 3435-3446.
170. Arvizo, R.R., et al., *Effect of nanoparticle surface charge at the plasma membrane and beyond.* Nano

letters, 2010. **10**(7): p. 2543-2548.
171. Liu, Y., et al., *The effects of temperature, salinity, concentration and PEGylated lipid on the spontaneous nanostructures of bicellar mixtures.* Biochimica et Biophysica Acta (BBA)-Biomembranes, 2014. **1838**(7): p. 1871-1880.
172. Yuan, H., et al., *Variable nanoparticle-cell adhesion strength regulates cellular uptake.* Physical review letters, 2010. **105**(13): p. 138101.
173. Lee, H., et al., *The effects of particle size and molecular targeting on the intratumoral and subcellular distribution of polymeric nanoparticles.* Molecular pharmaceutics, 2010. **7**(4): p. 1195-1208.
174. Gabizon, A., et al., *Tumor cell targeting of liposome-entrapped drugs with phospholipid-anchored folic acid-PEG conjugates.* Adv Drug Deliv Rev, 2004. **56**(8): p. 1177-92.
175. Aresh, W., et al., *The Morphology of Self-Assembled Lipid-Based Nanoparticles Affects Their Uptake by Cancer Cells.* Journal of Biomedical Nanotechnology, 2016. **12**(10): p. 1852-1863.
176. Mansoori, G.A., K.S. Brandenburg, and A. Shakeri-Zadeh, *A Comparative Study of Two Folate-Conjugated Gold Nanoparticles for Cancer Nanotechnology Applications.* Cancers, 2010. **2**(4): p. 1911.
177. Cuong, N.-V., Y.-L. Li, and M.-F. Hsieh, *Targeted delivery of doxorubicin to human breast cancers by folate-decorated star-shaped PEG-PCL micelle.* Journal of Materials Chemistry, 2012. **22**(3): p. 1006-1020.
178. Decuzzi, P., et al., *Intravascular delivery of particulate systems: does geometry really matter?* Pharmaceutical research, 2009. **26**(1): p. 235-243.
179. Gentile, F., et al., *The effect of shape on the margination dynamics of non-neutrally buoyant particles in two-dimensional shear flows.* Journal of biomechanics, 2008. **41**(10): p. 2312-2318.
180. Thurber, G.M., M.M. Schmidt, and K.D. Wittrup, *Factors determining antibody distribution in tumors.* Trends Pharmacol Sci, 2008. **29**(2): p. 57-61.
181. Kunz-Schughart, L.A., M. Kreutz, and R. Knuechel, *Multicellular spheroids: a three-dimensional in vitro culture system to study tumour biology.* Int J Exp Pathol, 1998. **79**(1): p. 1-23.
182. Kleinman, H.K. and G.R. Martin, *Matrigel: basement membrane matrix with biological activity.* Semin Cancer Biol, 2005. **15**(5): p. 378-86.
183. Lee, G.Y., et al., *Three-dimensional culture models of normal and malignant breast epithelial cells.* Nat Methods, 2007. **4**(4): p. 359-65.
184. Loessner, D., et al., *Bioengineered 3D platform to explore cell-ECM interactions and drug resistance of epithelial ovarian cancer cells.* Biomaterials, 2010. **31**(32): p. 8494-506.
185. Vahidnezhad, H., et al., *Modeling breast acini in tissue culture for detection of malignant phenotype reversion to non-malignant phenotype.* Iran Biomed J, 2009. **13**(4): p. 191-8.
186. Sameni, M., et al., *Imaging and quantifying the dynamics of tumor-associated proteolysis.* Clin Exp Metastasis, 2009. **26**(4): p. 299-309.
187. Sun, M.Y., et al., *Autofluorescence imaging of living pancreatic islets reveals fibroblast growth factor-21 (FGF21)-induced metabolism.* Biophys J, 2012. **103**(11): p. 2379-88.
188. Toh, Y.C., et al., *A microfluidic 3D hepatocyte chip for drug toxicity testing.* Lab Chip, 2009. **9**(14): p. 2026-35.
189. Toh, Y.C., et al., *A configurable three-dimensional microenvironment in a microfluidic channel for primary hepatocyte culture.* Assay Drug Dev Technol, 2005. **3**(2): p. 169-76.
190. Walsh, C.L., et al., *A multipurpose microfluidic device designed to mimic microenvironment gradients and develop targeted cancer therapeutics.* Lab Chip, 2009. **9**(4): p. 545-54.
191. Capretto, L., et al., *Microfluidic and lab-on-a-chip preparation routes for organic nanoparticles and vesicular systems for nanomedicine applications.* Adv Drug Deliv Rev, 2013. **65**(11-12): p. 1496-532.
192. Medina-Sanchez, M., S. Miserere, and A. Merkoci, *Nanomaterials and lab-on-a-chip technologies.* Lab Chip, 2012. **12**(11): p. 1932-43.
193. Vaupel, P., F. Kallinowski, and P. Okunieff, *Blood flow, oxygen and nutrient supply, and metabolic microenvironment of human tumors: a review.* Cancer Res, 1989. **49**(23): p. 6449-65.

194. Myer, K., *PHYSICAL AND FLOW PROPERTIES OF BLOOD*, in *Standard Handbook of Biomedical Engineering & Design*. 2003, McGraw Hill Professional, Access Engineering.
195. Hwang, N., et al., *Regulation of osteogenic and chondrogenic differentiation of mesenchymal stem cells in PEG-ECM hydrogels.* Cell and Tissue Research, 2011. **344**(3): p. 499-509.
196. Lin, C.-C. and K.S. Anseth, *Cell–cell communication mimicry with poly(ethylene glycol) hydrogels for enhancing β-cell function.* Proceedings of the National Academy of Sciences, 2011. **108**(16): p. 6380-6385.
197. Schukur, L., et al., *Directed Differentiation of Size-Controlled Embryoid Bodies Towards Endothelial and Cardiac Lineages in RGD-Modified Poly(Ethylene Glycol) Hydrogels.* Advanced healthcare materials, 2013. **2**(1): p. 195-205.
198. Christian, D.A., et al., *Flexible filaments for in vivo imaging and delivery: persistent circulation of filomicelles opens the dosage window for sustained tumor shrinkage.* Mol Pharm, 2009. **6**(5): p. 1343-52.
199. Jung, J.P., et al., *ECM-incorporated hydrogels cross-linked via native chemical ligation to engineer stem cell microenvironments.* Biomacromolecules, 2013. **14**(9): p. 3102-11.
200. Nadiarnykh, O., et al., *Alterations of the extracellular matrix in ovarian cancer studied by Second Harmonic Generation imaging microscopy.* BMC Cancer, 2010. **10**: p. 94.